# LASER PROCESSING FOR THIN AND HIGHLY EFFICIENT SILICON SOLAR CELLS

by

Jostein Thorstensen

Thesis submitted in partial fulfillment
for the degree of Philosophiae Doctor


Department of Physics
Faculty of Mathematics and Natural Sciences
University of Oslo

March, 2013

*Series of dissertations submitted to the*
*Faculty of Mathematics and Natural Sciences, University of Oslo*
*No. 1367*

ISSN 1501-7710



Cover: Inger Sandved Anfinsen.
Printed in Norway: AIT Oslo AS.

Produced in co-operation with Akademika Publishing.
The thesis is produced by Akademika publishing merely in connection with the thesis defence. Kindly direct all inquiries regarding the thesis to the copyright holder or the unit which grants the doctorate.

# ACKNOWLEDGEMENT

Although it may seem so from an outside perspective, a Ph. D. thesis is definitely not a solo race. (At least mine haven't been one.) I can't even take full credit for the decision to apply for a Ph. D. position at IFE, as this decision was strongly influenced by sensible and good advice from my friend and colleague Trygve Mongstad. Without him, I might not have ended up doing a Ph. D. at all, which would have been a great loss.

I have really appreciated the unique possibility given to me to devote myself for three years to play with cool lasers and stuff while at the same time trying to do my share at saving the world. However, the ride wouldn't have been nearly as rewarding if I hadn't been working with some of the best people I have yet come to know. You have always been positive and ready for fruitful discussions on all of the solar related topics that I have needed your help for, thereby doing your share at forming the contents of my thesis. At lunch breaks, coffee breaks, late evenings, conferences and cabin trips, you have been there, making sure that every day has had an enjoyable side. You have given me memories for life, I hope that I have given you something back. I'll remember you always.

My work on light-trapping structures would not have been the same without my cooperation with Jo Gjessing. Your competence, patience and collaboration on this topic has been greatly appreciated. My semiconductor and passivation expert, Halvard Haug has been a smile full of knowledge throughout my thesis.

I would like to thank my supervisors, Sean Erik Foss, Aasmund Sudbø and Erik Marstein for the valuable input and guidance I have received. Erik, you are always positive and encouraging, emphasizing that cool and important may very well be the same thing. Aasmund, your experience and knowledge has been invaluable, especially in the process of writing articles and the thesis. You are always patient and thorough, and my work has benefited greatly from your effort. Sean Erik, I probably haven't been the easiest of Ph. D. students, demanding quite a lot of space in your busy schedule. But I hope that you agree with me when I say that working together on finding our way through the maze that is laser processing for silicon solar cells has been a great journey. You have somehow always

found time for me, and our many discussions has lead us to some pretty interesting findings (although different findings than what we expected three years ago).

I wish to thank my parents for being there, always interested when I talk about my work (which must be pretty abstract for you by now), and always supportive no matter what. Finally, thank you, Åsa, love of my life. You never doubted that I could do this, even when I sometimes did. You make me stronger than I would be without you.

# ABSTRACT

Solar energy is rapidly becoming one of the most promising renewable energy sources available to us. Its abundant availability greatly surpasses any other energy source, and with the immense progress seen in production technology for photovoltaics (PV) over the last decade, the price for converting solar energy into electricity is rapidly decreasing. However, further price reductions are still required for solar energy to be directly cost competitive with conventional energy sources in the majority of the world.

This thesis focuses on the use of lasers as a processing tool for silicon based PV. Lasers may perform a range of solar cell processes, such as edge isolation, doping, removal of dielectrics, structuring and contact formation, and have the potential to enable processes required for advanced, high efficiency solar cell concepts.

Two objectives were formulated for this thesis. The first objective focuses on acquiring new fundamental knowledge on the interaction between ultrashort pulse lasers and silicon and dielectrics used for solar cells. Such knowledge is valuable in itself, and is important for process understanding and development. The second objective focuses on the development of laser based techniques for the production of light-trapping textures. This as light trapping gets increasingly important as the wafer thickness used in industry is constantly being reduced and as new wafering techniques may render traditional texturing methods obsolete.

On the interaction between pulsed lasers and silicon or dielectric layers, emphasis has been put on ultrashort laser pulses. Mechanisms causing ablation and the process result after ablation have been the main focus. The most investigated dielectric has been silicon nitride thin films. Through experiments and simulations it has been found that the dense electron-hole plasma created during the leading edge of an ultrashort laser pulse, either through linear or two-photon absorption, will play a prominent role in the ablation behavior of both silicon and silicon nitride using such ultrashort laser pulses. It has been shown that this plasma formation causes optical confinement of the laser energy which in silicon greatly reduces the optical penetration depth, and as such reduces the depth of the laser induced damage. Using lasers at a wavelength of 532 nm, the depth of the laser induced damage is reduced from approx. 3 μm to around 0.25 μm when going from nanosecond to picosecond pulse duration. Knowledge about the depth of laser damage as function of pulse duration is valuable when seeking the right laser for a given process. In

silicon nitrides, the plasma formation causes significant energy deposition into normally transparent films and may open for direct ablation of the dielectrics. It has also been shown that the ablation threshold on silicon is dependent on the temperature of the silicon substrate. In production, this would mean that the use of slightly elevated substrate temperatures would reduce the laser power required for a given throughput, or correspondingly increase throughput achievable with a given laser power.

On the topic of light-trapping structures fabricated by the use of lasers, two processes have been developed, and the performance of the textures has been measured. The patch texture, a geometric light-trapping texture for <100>-oriented monocrystalline silicon, showed a simulated increase in $J_{sc}$ of 0.5 mA/cm$^2$ when compared with the random pyramids texture, being the current industry standard. New wafering techniques provide thin silicon wafers for which the patch and random pyramids textures may not be applicable, and for which no industry standard texturing process exists. With this in mind, a diffractive honeycomb texture was developed. The use of microspheres on the wafer surface as focusing elements enabled the production of features with sizes well below 1 μm. The diffractive honeycomb texture shows a photogenerated current of 38 mA/cm$^2$ on 21 μm thick silicon wafers.

The results summarized above shows that both fundamental understanding of the laser-material interaction and results that are directly applicable have come from the investigation of laser-material interaction. The texturing processes that have been developed show that laser based texturing processes are capable of delivering high quality textures suitable for a range of different substrates.

# TABLE OF CONTENTS

# 1 INTRODUCTION

Electricity from sunlight. Direct harvesting of the immense and never-ending power brought to us by the sun. Not long ago, this elegant way of generating electricity was associated with satellites and space stations, or remote off-grid locations needing electricity to power a light bulb in a cabin. Today, on the other hand, we can read that Germany generates 50 % of its electric power from photovoltaic (PV) energy during mid-day hours on a sunny day [1]! In 2011, more than 28 GW of new PV generating capacity was installed globally [2]. This corresponds to about 200 $km^2$ of solar panels, or 1.5 times the size of the city of San Francisco! Obviously, our view on PV as a small niche market needs to be reviewed.

In a world where a rapidly increasing demand for energy is ever more strongly conflicting with an urgent need to cut back on greenhouse gas emissions, it seems necessary and inevitable that renewable energy sources will play a major role in our future global energy system. A recent report from the Intergovernmental Panel on Climate Change [3] predicts that wind and PV will account for up to 30 % of the world's electricity production by 2050, even in the moderate scenarios.

Direct solar energy is a tremendous energy resource, delivering around $4x10^{24}$ J of energy to the earth's surface per year (assuming a solar flux of 1 $kW/m^2$). The world's total energy consumption was in 2010 around $5.6x10^{20}$ J [4], meaning that the solar energy hitting the earth in about one hour is sufficient to cover the energy needs of the humanity for a whole year! This is by far the biggest source of energy available to us, and a great candidate for a transition to a more sustainable energy system. Furthermore, silicon based PV is based on non-toxic, abundant materials, silicon being the second most abundant element in the earth's crust after oxygen.

PV is currently the fastest growing renewable energy source, with an average growth rate of above 40 % per year since the year 2000 (Figure 1.1). Silicon based solar cells have an 85 % market share [5], and is thereby the absolutely dominant technology in PV. The growth in PV has been linked to economic incentives, and continued growth in

installed PV cannot rely on politically driven incentives alone. PV learning curves have, since the 1970's shown a 20 % reduction in module prices per doubling of cumulative production [6], a quite tremendous price reduction. This trend in price reductions however, has to be continued as incentives are continuously being reduced. This can either happen through reduction of production costs (fewer $ per solar cell), or by an increase in efficiency (more watts per solar cell). A combination of both would of course be ideal. In the current situation, the price for manufacturing of the solar cell and solar module has been dramatically reduced. This leads to a situation where balance of system costs, such as installation costs, the costs of mounting brackets, land usage costs etc. are beginning to dominate the total cost of a PV energy system [7]. Increased efficiency of the solar cell will reduce balance of system costs, e.g. by reducing the number of brackets and land area required for a given output power, meaning that retaining or improving the efficiency of the solar cell is essential for reduction of PV system costs.

The strive towards low cost, high efficiency solar cells has led to the introduction of several new processing tools and techniques that have enabled the impressive cost reductions seen in the PV industry. One group of tools that has the potential to change existing production techniques, and enable new processes and even new solar cell designs are lasers. Lasers have the ability to structure, cut or remove materials, alter the chemical composition of materials through the introduction of impurities, and several other processes. As shall be shown later in this thesis, there exists a range of solar cell related processes for which lasers can be applied. This thesis will focus on the use of lasers as a processing tool for improvement of silicon PV, where lasers have the potential to improve the efficiency of the solar cell and to reduce production costs.

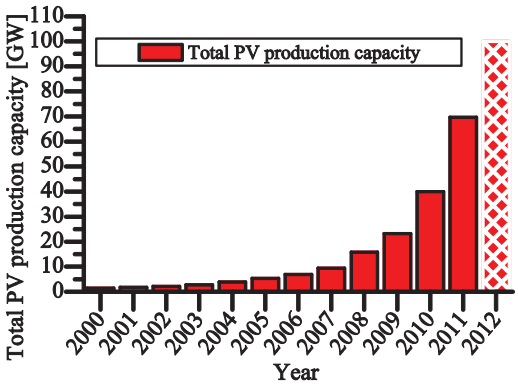


**Figure 1.1: Total installed PV production capacity. Taken from refs** [2], [8], [9]**. Preliminary data from 2012 indicates that the total installed PV production capacity has passed the 100 GW mark** [9]**.**

# 1.1 SILICON SOLAR CELLS

Solar cells operate by converting sunlight into electricity. In this section a brief review of the solar cell physics will be given. For a more thorough introduction, see e.g. [10].

One of the critical properties that make silicon suitable as a solar cell material is that it is a semiconductor, possessing a band-gap. This band-gap is a range of energies that the electrons in the materials are not allowed to have. The electron can either have an energy placing it in its ground energy state in the valence band, or it can be in an excited state in the conduction band. The electron can transition from valence band to conduction band and back through excitation and recombination processes described below. The energy required for an excitation may come from a photon, being the smallest package of energy one can divide light into. The sunlight consists of photons with a wide range of energies. The energy of the photon corresponds to what we observe as the color of the light, where the blue light consists of photons with a higher energy, and the red light consists of photons with lower energy. The energy of the photon also corresponds to a wavelength of the light, where the blue light has a shorter wavelength, and the red light has a longer wavelength. The spectral energy distribution of the sunlight is shown in Figure 1.3, adding up to 1000 $W/m^2$ at the earth's surface under given conditions, in what is known as the Air Mass 1.5 spectrum (AM1.5).

When a photon hits the silicon, it may be absorbed by an electron in the silicon, providing enough energy for the electron to be excited from its ground energy state in the valence band to an excited state in the conduction band, as indicated in Figure 1.2 a). Such an absorption process may only take place if the photon carries an energy corresponding to at least the band gap energy. The electron being excited will leave behind a hole in the valence band; an electron-hole pair is created. In a solar cell, the electron-hole pair moves by diffusion until it reaches the p-n junction. The p-n junction is a built-in asymmetry in the solar cell, where an electric field ensures that the electron will travel in one direction, while the hole travels in the opposite direction. As such, the electron may reach one of the electrical contacts, while the hole reaches the other contact, as a result of a combination of random diffusion and directional drift in an electric field. This is the principal mechanism for current generation in a solar cell. Only photons with high enough energy may be absorbed by the electrons. A photon with energy lower than the band-gap energy will not carry sufficient energy to lift the electron to the conduction band, and will as such not be absorbed in the semiconductor. Hence, its energy will not be converted into electricity.

This situation is indicated in Figure 1.2b), and is called sub-bandgap loss. On the other hand, photons with high energy can create an electron-hole pair as indicated in Figure 1.2 c), lifting the electron high above the conduction band edge. However, all the excess energy that is put into the electron will be rapidly lost, as the electron will collide with other electrons or atoms, losing energy until it reaches the conduction band edge. This loss process is called thermalisation.

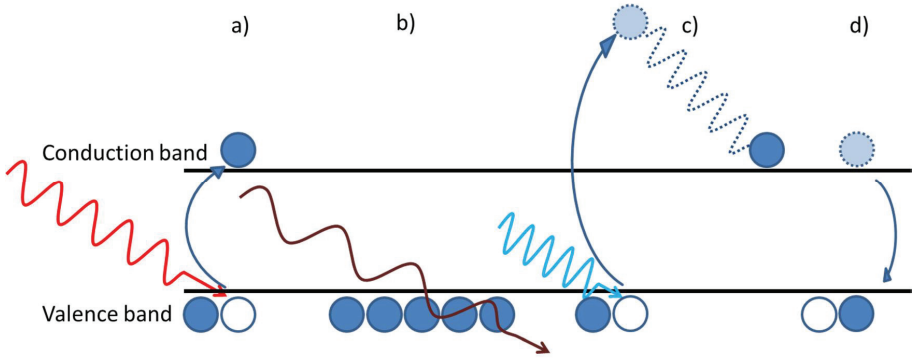


**Figure 1.2: Illustration of some absorption and loss mechanisms in a solar cell. a) Absorption, b) photon with insufficient energy for absorption, c) absorption and thermalisation, d) recombination.**

Figure 1.3 shows the spectral energy distribution from the sun as function of the wavelength of light. The area below the top graph indicates the total incoming solar energy, while the area below the lower graph indicates the energy available to us when taking into account the loss contributions discussed above, with a collective term called spectrum loss. Spectrum loss is a function of the band-gap energy of the semiconductor, and limits the efficiency of a silicon solar cell to below 50 %.

In a real solar cell, not all generated electron-hole pairs will contribute to current generation. There is always the chance that an electron finds a hole on its way to the contacts and relaxes back across the band gap, in a process called recombination, indicated in Figure 1.2 d).

Recombination may happen slowly in the bulk of a high-quality silicon wafer, but it will always take place even in a perfect material. These unavoidable recombination mechanisms are termed intrinsic recombination mechanisms. In a more realistic material, recombination happens faster. Examples of recombination-active areas are crystal defects or impurities in the silicon, highly doped silicon, silicon crystal boundaries or wafer surfaces and metal-silicon interfaces, such as contacts. By combining intrinsic recombination mechanisms with spectrum losses, we reach a maximum efficiency of a

solar cell, known as the Shockley-Queisser limit [11], which for silicon under an irradiance corresponding to the AM1.5 spectrum is around 29 % [12]. Currently, the record efficiency of a silicon solar cell is 25 % [13], which is actually quite close to the theoretical maximum of 29 % given by the Shockley-Queisser limit.

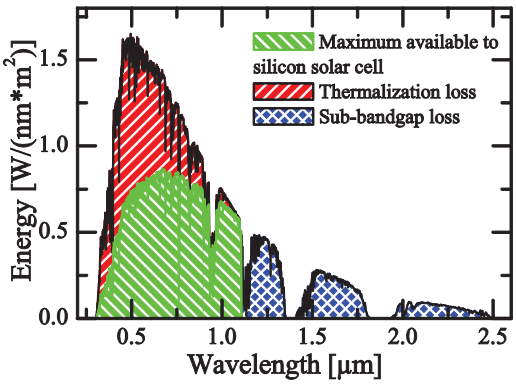


**Figure 1.3: Solar irradiance (upper, black curve) and the maximum available energy to a silicon solar cell when considering spectrum losses** [14].

The efficiency of the solar cell, $\eta$ is of course of outmost importance. Several factors determine this cell efficiency which can be collected into the expression

$$\eta = \frac{P_{cell}}{I_{solar}} = \frac{J_{sc}V_{oc}FF}{I_{solar}} = \frac{J_{mpp}V_{mpp}}{I_{solar}}. \qquad 1.1$$

In this expression, $P_{cell}$ is the output power density of the cell, $I_{solar}$ is the solar irradiance $J_{sc}$ is the current density at short circuit conditions, being the maximum current available from a solar cell. $V_{oc}$ is the voltage at open circuit conditions, being the maximum voltage available from a solar cell. As both open and short circuit conditions would lead to zero power output of the solar cell, the maximum power output of the solar cell is found by operating the solar cell at a voltage somewhat lower than $V_{oc}$, in what we call the maximum power point. $J_{mpp}$ and $V_{mpp}$ are current density and voltage at maximum power point, respectively, and the fill factor $FF$ is the ratio of $J_{mpp}V_{mpp}$ to $J_{sc}V_{oc}$. We see from the expression that $J_{sc}$, $V_{oc}$ and $FF$ should be as high as possible.

## 1.2 MOTIVATION AND OBJECTIVE OF THE THESIS

The record silicon solar cell with an efficiency of 25 % mentioned earlier is a beautiful example of solar cell engineering. The problem, however, is that in order to make such a cell, several processes that cannot be directly transferred into mass production are employed. A common feature of several high-efficiency solar cell concepts is that they require some form of local processing, which on lab-scale cells has been enabled by photolithography. Photolithography is, however, generally considered incompatible with the very high throughput required by the solar cell industry. As lasers provide excellent spatial resolution and translational control, they may provide similar local processing capabilities with much simpler processes, and may as such open for industrial scale local processing and high solar cell efficiencies in industrial production. Indeed, local laser processing is making its way into industrial production lines today. Laser processing may, however, only be successfully implemented if the process does not have a negative impact on the quality of the solar cell materials.

In order to develop low damage laser processes, fundamental insight into the physical interaction between the laser and the solar cell materials is absolutely crucial. Using pulsed laser sources, the laser-material interaction will depend on laser pulse duration, laser wavelength and material properties. Fundamental understanding of these dependencies will give understanding of the laser parameters required for successful laser processes. As such, knowledge about the dominating physical mechanisms involved in laser-material interaction will serve as a foundation for development of good laser processes, or even the other way around, serve as a pointer towards yet to be developed laser sources required for a given process. Fundamental knowledge about laser-material interaction would be useful also outside the field of silicon photovoltaics. As such, the first main objective of this thesis is:

> *To gain fundamental understanding of the interaction between pulsed lasers and materials relevant for silicon solar cells.*

The materials in focus shall be silicon and dielectric layers covering the silicon, functioning as e.g. anti-reflection coatings, passivation layers or diffusion or etch barriers.

The main focus shall be on parameter ranges giving material removal, called ablation, as ablation is required for a wide range of laser processes. This understanding shall be sought through a combination of experimental techniques and simulations. Laser sources with varying wavelength and pulse duration shall be applied on a selection of materials. Simulation models accounting for the physics encountered with the use of long (nanosecond) and ultrashort (picosecond) pulses shall be developed.

The second main topic of the thesis concerns thin silicon wafers. Silicon is an indirect band-gap semiconductor meaning that photons may travel quite a distance in silicon before they are absorbed. Thicker wafers would thus increase light absorption. Unfortunately, silicon is quite expensive, meaning that thick cells would be too costly. Currently, there is a strong drive in the industry to reduce the standard wafer thickness from the thickness used today (around 160 μm) to 120 μm by 2020 [15]. Today, wafers are typically manufactured by wire sawing, and almost half of the silicon is lost as "saw dust", or kerf loss. Several novel techniques are being developed in order to eliminate kerf loss and enable production of even thinner wafers, between 20 and 50 μm thick [16–19], thus drastically reducing silicon consumption. With this trend in mind, development of highly efficient light-trapping techniques for efficient collection of the sunlight is needed. For these new kerf-less wafers, traditional texturing methods may not be applicable, due to e.g. (i) the crystal orientation of the wafer or (ii) the lack of saw damage on the silicon surface for seeding of the structures or (iii) simply because currently available texturing processes remove too much of the silicon [20]. Several approaches have been suggested, but a solution suitable for mass production is yet to be developed. The use of lasers for texturing of silicon wafers is interesting, due to the laser's ability to create precisely defined geometrical patterns on the wafer surface. The use of a highly accurate laboratory laser setup would identify the practical limits to the texture quality achievable by laser based texturing. The second main objective for this thesis is

*To develop laser-based techniques for manufacturing of efficient light-trapping textures.*

The focus shall be on textures investigated theoretically in the literature, but for which no industry standard method exists. As laser-based texturing is not yet a mature technique,

emphasis shall be put on investigation of the achievable quality of the developed textures and their practical, rather than theoretical light-trapping potential.

## 1.3 STRUCTURE OF THE THESIS

This thesis is written as a collection of papers with an introductory text. The findings already presented in the papers will not be repeated to any length in the main text. The purpose of the main text is to provide an introduction to the field of solar cell research, motivate the topic of the thesis, and provide additional theory and experimental details that are not presented in the papers. The papers are appended at the end of the thesis.

The thesis is divided into 6 chapters. In chapter 1, the thesis is placed in a broader context and an introduction to solar cell technology is provided. At the end of the chapter, a summary of the articles is given.

Chapter 2 presents details of the main experimental tools and techniques utilized during the work with this thesis.

Chapter 3 is dedicated to laser-material interaction and laser damage. The chapter begins with an overview of the state of the art of laser processing for silicon solar cells. Then, laser-material interaction and the difference between long and ultrashort pulses are presented, followed by details on the simulation models applied within the thesis. Additional simulation results and physical insights that are not included in the papers are also presented in this chapter, and some methods for characterization of laser-induced damage are summarized.

Chapter 4 is dedicated to the subject of light trapping in silicon solar cells. The need for light-trapping structures is motivated, and some typical structures are presented. Some previously investigated methods for laser assisted structuring of silicon are reviewed, and the approach to laser assisted structuring chosen in this thesis is motivated. The industrial feasibility and potential of the processes is discussed, comparing the structures to industry standard methods.

Chapters 5 and 6 provide conclusions and suggestions on further work related to the investigation of laser-induced damage, investigation of laser-material interaction and further development of the light-trapping structures presented in the thesis and papers.

# 1.4 SUMMARY OF THE ARTICLES

This section presents an overview of the papers included in this thesis. The papers are appended in their entirety at the end of the thesis.

PAPERS I – IV consider textures for light trapping in silicon, while PAPERS V – VIII discuss the fundamentals of laser-material interaction for the silicon and dielectric on silicon systems.

**PAPER I** *J. Thorstensen and S. E. Foss, "Laser assisted texturing for thin and highly efficient monocrystalline silicon solar cells," in Proceedings of the 26th European Photovoltaic Energy Conference, pp. 1628 – 1631, 2011.*

In this conference contribution, a process was developed for production of inverted pyramids and patch textures on <100> - oriented monocrystalline silicon for light-trapping. These textures have a high potential for light-trapping, but are normally produced by photolithography. The process described in this paper is based on the use of a laser to create openings through an etch barrier, after which KOH etching of the underlying silicon develops a pattern consisting of <111> crystal orientations. The geometrical accuracy of the laser system is good, and the structures develop as intended, resulting in a texture with up to an estimated 94 % area coverage.

**PAPER II** *J. Thorstensen, S. E. Foss, and J. Gjessing, "Light-trapping properties of patch textures created using Laser Assisted Texturing," Progress in Photovoltaics: Research and Applications, available online, DOI: 10.1002/pip.2335, 2013.*

In this paper, the light-trapping properties of the patch texture developed in PAPER I was investigated. Jo Gjessing (IFE) was of great assistance during the optical measurements. Optical absorption measurements on a patch textured silicon wafer are performed and these measurements are compared with ray-tracing simulations. This enables us to extract information about the quality of the texture. From these simulations, the current-generating potential of the textures is extracted. It is found that the created texture gives an increase in $J_{sc}$ of up to 0.5 mA/cm$^2$ compared to the random pyramids texture, and as such, it is concluded that it is possible to generate high quality textures with laser based methods. The process would be interesting for application on <100>-oriented monocrystalline

silicon. It is recognized that the process must be simplified in order to justify the added process complexity.

**PAPER III** *J. Thorstensen, J. Gjessing, E. Haugan, and S. E. Foss, "2D periodic gratings by laser processing," Energy Procedia, vol. 27, pp. 343–348, 2012.*

In this conference contribution a process for producing diffractive structures in silicon is presented. The process is similar to the process described in PAPER I, but a monolayer of polystyrene microspheres is this time applied onto the etch barrier. In the laser processing step, the microspheres act as focusing elements, and serve to increase the spatial resolution of the laser to below 1 μm. An isotropic etch develops a texture consisting of nearly hemispherical dimples in a honeycomb pattern. The process is applicable to monocrystalline silicon with any crystal orientation, or to multicrystalline silicon. With this masked etching process, only the silicon from the dimples is removed, causing a thinning of the silicon wafer of below 350 nm, ideally suited for thin silicon wafers where preservation of wafer thickness is crucial. The paper serves as a proof of concept of the remarkable increase in spatial resolution brought about by the application of the micro-lens array made up by the microspheres.

**PAPER IV** *J. Thorstensen, J. Gjessing, E. S. Marstein, and S. E. Foss, "Light-trapping Properties of a Diffractive Honeycomb Structure in Silicon," IEEE Journal of Photovoltaics, vol.3, no. 2, pp. 709 – 715, 2013.*

In this paper, the honeycomb structure generated in PAPER III is examined in more detail. Firstly, the texture is applied to large area, by utilizing a top-hat beam shaper, an optical component transforming a Gaussian beam profile to a uniform, square intensity distribution. The structure is applied to silicon wafers with a thickness of 21 – 115 μm. Optical absorption characteristics were measured by Jo Gjessing, who also analyzed the contributions to optical loss. The observed trends are explained and the diffractive honeycomb textures are compared with random pyramids, isotropic etched samples and polished wafers, as these constitute various relevant references. It is found that the diffractive honeycomb structure delivers light trapping that surpasses many of the relevant references showing a photogenerated current of 38 mA/cm$^2$ on 21 μm thick wafers. As such, the texture has the potential to provide a significant increase in $J_{sc}$ on wafers where

random pyramids cannot be efficiently applied, e.g. for kerf-less wafers with a non-<100> crystal orientation.

**PAPER V** *J. Thorstensen and S. E. Foss, "Temperature dependent ablation threshold in silicon using ultrashort laser pulses," Journal of Applied Physics, vol. 112, no. 10, p. 103514, 2012.*

In this paper the physics of the interaction between silicon and ultrashort laser pulses is considered. Experiments are performed showing that the ablation threshold fluence varies with silicon substrate temperature. A numerical model is established, considering the dynamics of the absorption of the incoming laser light, i.e. the energy deposition, and the generation dynamics of conduction band electrons. From this model, information about the dominating physical processes is extracted, and the experimentally observed temperature dependence is reproduced in simulations. The paper contributes to new knowledge on the temperature and wavelength dependence of the ablation threshold of silicon using ultrashort laser pulses, in addition to interpretations on the underlying physical mechanisms.

**PAPER VI** *Jostein Thorstensen, Ragnhild Sæterli and Sean Erik Foss, "Laser ablation mechanisms in thin silicon nitride films on a silicon substrate," submitted to IEEE Journal of Photovoltaics, April 2013.*

In this paper the ablation of silicon nitrides with varying index of refraction from silicon is investigated. Varying laser pulse duration and three laser wavelengths are applied, and the mechanism for ablation is investigated. In this paper, TEM analysis was performed by Ragnhild Sæterli (NTNU). A transition region is observed when using a wavelength of 515 nm, where the ablation goes from indirect to direct. In some cases, both direct and indirect ablation is observed in the same spot. In these cases, it is found that the free-carrier contribution must be significant in the interaction between the laser pulse and the dielectric – silicon stack. The focus in this article on the underlying physical mechanisms of silicon nitride ablation is novel.

**PAPER VII** *Jostein Thorstensen and Sean Erik Foss, "New approach for the ablation of dielectrics from silicon using long wavelength lasers," submitted to Energy Procedia, March 2013.*

This conference contribution shows a different approach to ablation of dielectrics from semiconductors. By investigating the absorption characteristics of silicon and various PV-relevant dielectrics, it is found that in the mid- to far-IR, silicon is transparent, while the dielectrics are absorbing. This behavior is interesting, as it opens for energy deposition in the dielectric rather than in the silicon, potentially resulting in lower substrate damage. For the measurements of absorption in dielectrics, Ørnulf Nordseth (IFE) prepared samples with aluminum oxide ($AlO_x$), and Halvard Haug (IFE) prepared samples with silicon dioxide. Simulations on the temperature dynamics of the process are performed, and it is seen that short laser pulses may be able to remove the dielectric without melting the silicon substrate. In experiments however, signs of melting of the silicon are found, indicating that a pulse duration of 100 ns is still too long. As such, the paper brings the idea of a new process, while it remains to be proven if the process can be successful using shorter laser pulses.

**PAPER VIII** *Jostein Thorstensen and Sean Erik Foss, "Investigation of depth of laser damage to silicon as function of wavelength and pulse duration," accepted for publication in Energy Procedia, May 2013.*

This conference contribution describes an experiment determining the depth of laser induced damage. Ultrashort laser pulses at three wavelengths are applied to a silicon substrate. Thereafter, a controlled wafer thickness is removed by wet chemical etching, and the wafer is passivated. The minority carrier lifetime is measured as function of etch depth and the depth where bulk lifetime is restored gives a measure of the depth of the laser induced damage. The results are compared with previous investigations by Engelhart *et al.* [21], and show that the depth of damage is severely reduced when going to ultrashort laser pulses, as a result of reduced thermal diffusion and increased optical confinement due to non-linear absorption. While thermal and optical confinement is expected when using ultrashort laser pulses, the presented quantitative experimental evidence on silicon is novel. In addition, An estimate on the minority carrier lifetime in the laser damaged volume is presented. These calculations are also novel in the context of laser damage.

**MAIN FINDINGS**

On the topic of production of light-trapping structures on silicon using lasers, two innovative production techniques are presented, and the produced textures outperform important reference textures. As such, it is shown that it is possible to create high quality textures by the use of lasers. The processes would require significant modifications in order to be industrially relevant, however, for thin, non-<100>-oriented wafers, no industrially mature methods exist. As such, the process presented in PAPERS III and IV is of contemporary interest.

On the investigation of the physics of the interaction between pulsed lasers and solar cell materials, several new findings are presented. The temperature dependent ablation thresholds presented in PAPER V are novel, and are particularly interesting as the simulation model provides possible explanations to the underlying physical mechanisms. For practical applications, the use of a slightly elevated substrate temperature can significantly reduce the required laser power, or correspondingly increase the process throughput. This effect is strongest at the fundamental wavelength of the laser, making it more interesting to use this wavelength, thereby reducing the complexity of the laser equipment. In PAPER VIII, concrete evidence of thermal confinement and non-linear optical confinement is presented. Considering the interest in ultrashort-pulse lasers for industrial purposes seen over the last few years, these results should be directly applicable and relevant to the industry, as the depth of laser damage is a critical parameter in laser processing. PAPER VII is an example of how fundamental insight may spawn ideas to novel processes where the necessary tools are yet to be developed

# 2 EXPERIMENTAL TOOLS AND TECHNIQUES

In this thesis, a number of experimental tools and techniques have been applied. Silicon wafers must be cleaned and prepared for processing. Often, a dielectric coating has been deposited onto the wafer surface. The laser has been the primary process tool, often accompanied by wet chemical etching. For characterization of the process result, a range of optical characterization techniques such as spectroscopy and microscopy have been applied. Also the electrical properties of the samples have been characterized. This chapter presents an overview of the main experimental tools and techniques applied during this thesis.

## 2.1 LASERS

The laser is the most important processing tool in this thesis. To two laser systems have been available at the Department for Solar Energy (IFE), and other lasers have been applied at other locations. These will be described below. The laser parameters are summarized in Table 1.

*Green nanosecond laser*
The affordable workhorse laser for silicon processing is the green nanosecond laser, more specifically, the frequency doubled diode-pumped solid-state (DPSS) laser. A Rofin PowerLine 20 E – LP SHG2 laser has been available at IFE. It operates at 532 nm, with a pulse duration between approx. 50 and 250 ns. The laser has been used as reference in PAPER VIII and for process development for the patch pattern described in PAPER I and PAPER II.

*Other solid state lasers*
At the Laser Zentrum Hannover, experiments have been performed using solid state lasers with nanosecond pulse duration with a wavelength of 266 and 355 nm and 10-40 ns pulse

duration (Coherent AVIA) and 1064 nm and 30 ns pulse duration (IPG YLPM-1-A4-20-20).

*Short pulsed $CO_2$-laser*

For the work with PAPER VII, a short pulsed $CO_2$-laser from a commercial supplier was applied. The laser pulse duration was approx. 100 ns, and the wavelength was 9.3 µm.

*Ultrashort-pulse laser*

For the majority of the work in this thesis, an Amplitude Systemes s-Pulse HP laser was applied. This laser has a second harmonic – third harmonic generation (SHG – THG) module. The laser itself delivers pulses that by an adjustable pulse compressor can be freely selected to values between approx. 0.5 ps and 6.5 ps at a fundamental wavelength of 1030 nm. Second and third harmonic wavelengths of 515 and 343 nm are available by adjusting the power through the SHG – THG module. The laser is equipped with both a galvo scanner and fixed lenses, and an xyz-table for sample translation. For the processing in PAPER IV, a top-hat beam shaping element from Eksma Optics was applied. This element transforms a Gaussian beam profile into a uniform, square intensity distribution. Such an intensity distribution allows for uniform processing of larger areas, but the output intensity distribution is sensitive to the exact beam shape and quality of the incoming beam, as observed in PAPER IV.

**Table 1: Summary of laser parameters.**

| Laser model<br>Parameter | Oxford Laser/ Amplitude s-pulse HP | Rofin PowerLine LP | Other nanosecond lasers |
|---|---|---|---|
| Wavelength [nm] | 343, 515 and 1030 | 532 | 266,355, 1064 and 9300 |
| Pulse duration [s] | $0.5 - 6.5 \times 10^{-12}$ | $50 - 250 \times 10^{-9}$ | $10 - 100 \times 10^{-9}$ |
| Repetition rate [kHz] | 1-300 | 10-100 | |
| Beam diameter in focus [µm] | 9-40 | 40 | |
| Beam quality ($M^2$) | <1.3 | <1.3 | <1.4 |

For the majority of the work within this thesis, non-overlapping laser pulses are utilized, as incubation effects are observed where multiple pulses are applied [22]. Slight surface and volume modifications from previous pulses will increase absorption, thereby reducing the ablation threshold and cause the formation of larger surface structures (ultimately providing black silicon,) that are undesirable when investigating the topics of this thesis. Two types of incubation effects are shown in Figure 2.1, using ultrashort laser pulses. (Top left) SEM image of self-assembling structures similar to those found in so-called black silicon, developed by irradiating one spot with multiple pulses. (Top right) SEM image of laser-induced periodic surface structures (LIPSS). LIPSS are periodic waves or ridges with size on the order of the wavelength of the applied light, developed by applying partially overlapping pulses [23]. (Bottom left) AFM height profile of LIPSS. (Bottom right) Area covered with LIPSS viewed at different angles. Different viewing angles gives different wavelength, characteristic for diffraction.

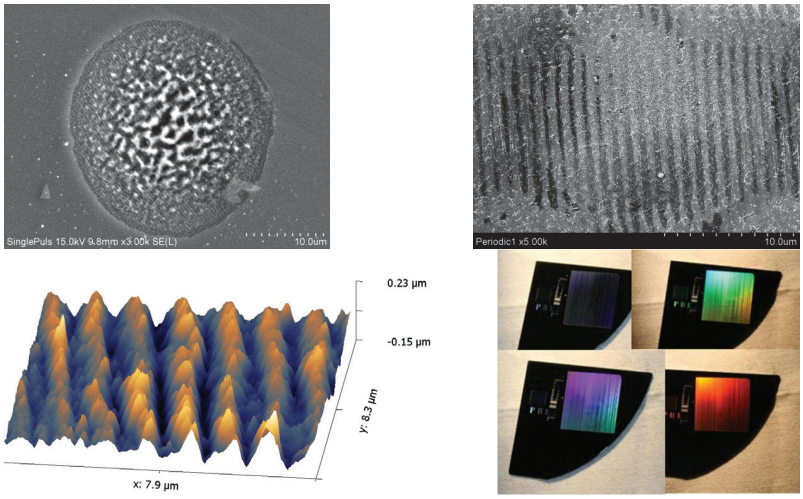


**Figure 2.1: Surface modifications caused by ultrashort laser pulses. Top left: SEM image of multiple pulse irradiation in one spot, causing surface structures to appear. Top right: SEM image of Laser-induced periodic surface structures (LIPSS). Bottom left: AFM height map of the same LIPSS structure. Bottom right: Wafer with LIPSS photographed at different angles, showing the typical rainbow-appearance characteristic of diffractive surfaces.**

## 2.2 EXTRACTION OF LASER PARAMETERS

As stated above, non-overlapping pulses were applied during the majority of the work with this thesis. Processing with these conditions normally gives a region on the wafer surface that has in some way been affected, and the extension of the affected area will depend on a

range of laser and process parameters. The process most frequently investigated in this thesis is the ablation of dielectrics from a wafer surface, and the ablated diameter is often sought. Examples of spots with a clearly defined ablated diameter are seen in Figure 2.1 (Top left) and Figure 2.2.

The laser ablation process is often characterized by the laser fluence required for ablation to take place, known as the ablation threshold fluence (ablation threshold) $F_{th}$. This quantity is of outmost importance when describing the ablation process, and is generally dependent on material parameters and laser parameters such as laser wavelength and pulse duration. While the wavelength is set directly by the laser, the pulse duration and laser fluence must be measured or controlled externally.

The laser fluence is only available to us indirectly, by measuring several quantities, these being average laser power, pulse repetition rate and spatial fluence distribution. The average laser power was measured using a PS19Q thermopile power sensor from Coherent Inc. This sensor has a rated sensitivity of 10 μW, and a calibration accuracy of 1 %. Practically, however, the measured power tends to fluctuate more than this, especially at low powers, as a result of power sensor inaccuracies or as a result of actual variations in laser output power. Therefore, 5 % has been used as the uncertainty of the laser power meter.

The spatial fluence profile of a laser beam may be quantified by its $M^2$ – number, where $M^2 = 1$ describes a Gaussian fluence distribution. This distribution is also the one where the tightest focus is obtainable. All other fluence distributions have an $M^2 > 1$, and as such have larger foci by a factor of $M^2$. The lasers applied in this thesis are nearly Gaussian, showing an $M^2$-value of below 1.3. As such, the fluence profile is assumed to be Gaussian. However, also the width of the Gaussian fluence distribution must be known, which will vary depending on how far from the focal plane the sample to be processed is located. Liu [24] describes a method for extracting the beam diameter of a Gaussian beam by measuring the diameter of the ablated area as function of pulse energy. The method also gives the ablation threshold fluence, and is as such a valuable tool in characterization of laser ablation, and is described by the expression:

$$r_{abl}^2 = \frac{c^2}{2} ln\left(\frac{F_0}{F_{th}}\right) = \frac{c^2}{2}\left[ln\left(\frac{2E}{\pi c^2}\right) - ln(F_{th})\right] \quad 2.1$$

Here, $r_{abl}$ is the ablated radius, $c$ is the beam radius measured at the point where the intensity has dropped to $1/e^2$ of the peak fluence level. $F_0$ and $F_{th}$ are the peak fluence

of the laser pulse and the ablation threshold fluence. Using the right hand side expression, requires only the ablated radius $r$ and pulse energy $E$, which both can be measured, and the unknown quantities, namely $F_{th}$ and $c$, that are found by fitting the expression to the measurement data.

The ablated diameter has been found using the image processing program ImageJ [25], by using the color contrast between the ablated spot and the remaining dielectric layer, as shown in Figure 2.2. One challenge using this technique is that the color change seldom is step-like. There will always be a blurry area where the color is in between that of the spot and the surroundings. This error contribution has been analyzed in PAPER V, and was found in combination with uncertainty in the power meter and deviations from the modeled trend to be around +/- 20 %. It is also seen in Figure 2.2 that the spot is not perfectly round. The ablated radius, $r_{abl}$, is estimated from the ablated area, $A_{abl}$ through the relation $r_{abl} = \sqrt{A_{abl}/\pi}$.

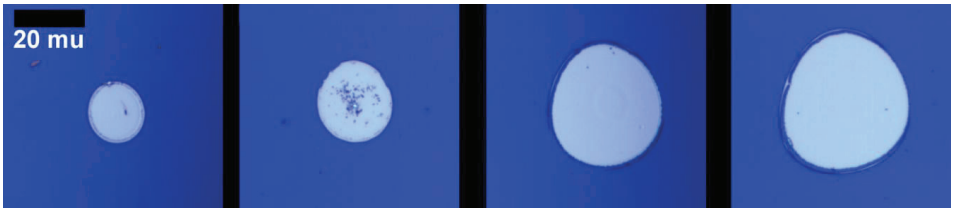


**Figure 2.2: Typical set of images used as data for the method by Liu** [24]**. Shown here is the ablated spot obtained when ablating $SiN_x$ from Si using a laser wavelength of 1030 nm and a pulse duration of 3 ps. The applied laser pulse energy increases from left to right.**

The pulse duration was only measured for the ultrashort pulses, at the fundamental wavelength using a PulseCheck 50 autocorrelator from APE (Angewandte Physik & Elektronik GmbH). The pulse duration at second and third harmonic wavelengths were not directly measured, as the autocorrelator was not built for these wavelengths. The pulse duration at harmonic wavelengths may be shorter than at the fundamental wavelength, as a result of the intensity dependence of the efficiency of the wavelength conversion process, or longer, as a result of dispersion effects. The manufacturer has measured the pulse duration at the second harmonic wavelength, finding that this pulse duration approximately equals that of the fundamental wavelength, possibly being marginally shorter. The laser manufacturer expects the same behavior at the third harmonic wavelength. In this work, it is assumed that the second and third harmonic pulse have the same pulse duration as the fundamental wavelength pulse.

## 2.3 THIN FILM DEPOSITION

In solar cell processing, thin dielectric films are frequently deposited onto the silicon wafer in order to improve optical or electrical properties. The typical blue color of a solar cell arises from a thin anti-reflection coating, reducing the reflectivity of the solar cell. Other films may primarily be deposited in order to reduce recombination at the wafer surfaces.

The dielectrics used in this work (with the exception of one thermal oxide) were all deposited by plasma-enhanced chemical vapor deposition (PECVD), a technique commonly used for dielectric deposition in the PV industry. In the PECVD process, reaction gases are ionized by an electric field, in the PECVD system applied in this thesis an RF field. This ionization helps improving the reaction rate and allows for fast deposition at relatively low temperatures. An Oxford Instruments Plasmalab System 133 PECVD system was used for this deposition. For laser processing, silicon nitride ($SiN_x$) has been most frequently used, but also some silicon oxide ($SiO_x$) and silicon oxynitride ($SiO_xN_y$) films. For passivation, amorphous silicon (a-Si) was used in order to obtain very low surface recombination velocity. Generally, all films deposited by PECVD will contain relatively large amounts of hydrogen, and the films deposited in this thesis are amorphous. As such, a more precise description of the films would be e.g. hydrogenated amorphous silicon nitride (a-$SiN_x$:H), but for convenience, the shorter notation given above shall be used. For PAPER VI, several different $SiN_x$ films were deposited. The composition of these films was varied by adjusting the flow of silane ($SiH_4$) to the chamber, while keeping all other deposition parameters (gas flows, pressure and temperature) constant.

As noted in PAPER VIII, surface-near damage to the silicon is observed after deposition of PECVD $SiN_x$, observed in the form of reduced lifetime on samples where the $SiN_x$ was removed in a 5 % hydrofluoric acid solution and the wafer was subsequently passivated with a-Si. As this damage was discovered late in the thesis, there was no time for more thorough investigation of the damage mechanisms, and the damage is tentatively attributed to ion bombardment from the deposition process.

## 2.4 MICROSCOPY

Both in the work with texturing processes and in the work on laser – material interaction, microscopy has been used extensively for measurements on ablated diameters and general

quality of process assessments. For this work, a Zeiss Axioskop 2 MAT optical microscope was used.

A Hitachi S-480 scanning electron microscope (SEM) has been applied for more detailed analysis. The SEM has very high depth of view and high resolution, and is as such well suited for the investigation of textured surfaces and small features. Bare silicon or silicon with a partial dielectric cover have been investigated in the SEM. The limited electrical conductivity of these samples has in some cases limited the resolution and contrast of the SEM images, but has the advantage that the process result is not covered up, as would be the case if coating the sample with a conductor before performing SEM.

For accurate height-profiles on the nano-scale, a PicoStation atomic force microscope (AFM) from Surface Imaging Systems has been applied. This AFM was not equipped with a microscope, and hence, searching across the sample was a tedious task. Furthermore, scanning as large as 47x47 µm requires rather large scan speeds, on the order of 10 µm/s. This results in vulnerability to loss of accuracy, especially when encountering debris on the surface. The open-source program Gwyddion [26] was used for post-processing of the images. As most AFM images show bow or tilt, a polynomial background ($2^{nd}$ order) was removed by masking out the laser spot and assuming that the wafer surface outside of the laser spots was flat. However, the leveling may not be completely accurate. As such, the line profiles may still carry some artifacts due to bow or tilt that hasn't been completely removed. In Paper VI, ablation craters from the ablation of $SiN_x$ are analyzed, showing height differences of a couple of tens of nanometers over a couple of tens of micrometers. Such slow height variations will be sensitive to residual bow, and the measured height differences should be treated with caution. These distortions are not expected to be critical to the analysis of the profiles, as e.g. step-like height profiles are still clearly visible.

## 2.5 WET CHEMICAL PROCESSING

Several different wet chemical processes have been applied in this thesis, either for cleaning or for structuring or removal of the silicon. These will be briefly summarized here.

*Cleaning*

All samples were dipped in a 5 % hydrofluoric acid (HF) solution for 1 minute before thin film deposition. This removes any oxide layer on the wafer surface. HF was also used after laser processing in the cases where remaining $SiN_x$ or $SiO_x$ needed to be removed, specifically if the wafer was to be passivated or the whole surface was to be etched.

Samples intended for lifetime measurements were in addition etched in a piranha solution (4:1 sulfuric acid:hydrogen peroxide, (4:1 $H_2SO_4$:$H_2O_2$)) and in concentrated hydrochloric acid (HCl), in order to ensure the best possible surface passivation. Piranha removes organic residues, while HCl removes metallic contaminations. These etches remove no or only very little silicon, and as the surface-near laser damage is sought, this processing will not influence the sought-after results.

*Silicon etches*

Three silicon etches have been applied in this thesis. Firstly, for the creation of the patch textures in PAPER I and PAPER II, a 10 % potassium hydroxide (KOH) solution at 88 °C was applied. Low concentration KOH solutions preferentially creates pyramidal structures by exposing <111> crystal planes. Increasing the concentration of KOH from 2 to 10 % ensured a more practical etch time reaching a depth of 10 µm in less than 10 minutes. Figure 2.3 (top left) shows an inverted pyramid structure which is not fully formed, as a result of too short etch time, and complete inverted pyramids by increasing etch time (top right).

For the etch-back experiments, flat surfaces are desired, and a homogenous etch is preferred. For this purpose, a 47 % KOH solution at 88 °C was used, as high concentration KOH solutions tend to leave behind a rather flat wafer surface. An example of a wire-sawn wafer etched in high concentration KOH is shown in Figure 2.3 (bottom left). The samples applied in this thesis are polished, and the result of high concentration KOH etching is very flat as shown in Figure 2.3 (bottom right). The high concentration KOH etch showed an etch rate of approx. 1 µm/min, and it was as such easy to achieve relatively shallow etches. Both KOH etches were kept in a water-bath for better temperature control.

For the diffractive structures in PAPER III and PAPER IV, an isotropic etch was required. An HNA (Hydrofluoric acid, Nitric acid, Acetic acid) etch was chosen. As described in PAPER III, the processing results were improved when increasing the HF content in the HNA solution from 1:40:15 to 5:40:15, as under-etching was suppressed. It is suspected that under-etching is caused by a mechanism allowing the acid to penetrate more rapidly along the wafer surface, thereby increasing the area of attack of the etch.

Such mechanisms could be either an interface oxide layer, as silicon oxide has a high etch rate in this solution, or surface-near crystal damage. Surface-near damage from ion bombardment is noted in PAPER VIII, and would be present also in the samples used in PAPER III and PAPER IV. Damaged crystals may have more attack points for the etch, and may as such have a higher etch rate than an undamaged crystal.

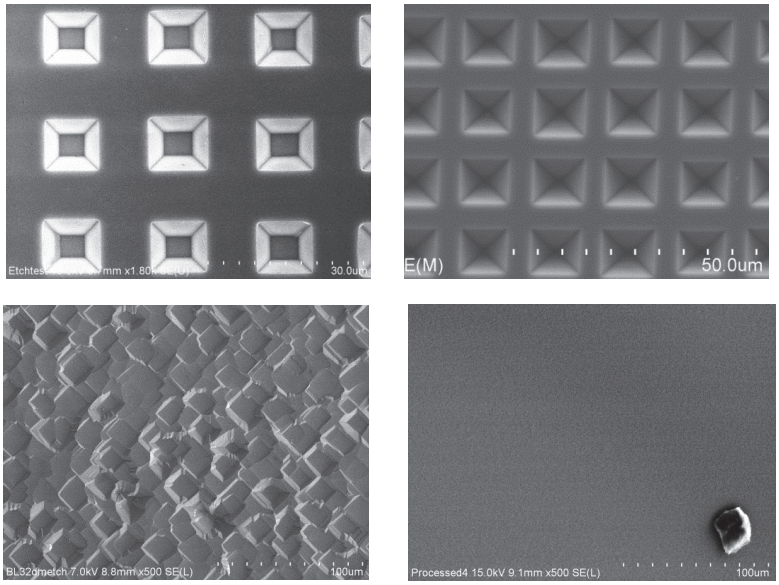


**Figure 2.3: (Top) Inverted pyramid structure showing incomplete (left) and complete (right) etching. (Bottom) KOH polishing etch on slurry-sawn wafer (left) and on polished wafer (right). No structures are observed on the polished wafer, an image with a piece of debris in the lower right corner is chosen in order to indicate the image resolution and contrast.**

## 2.6 REFLECTANCE AND TRANSMITTANCE MEASUREMENTS

For several of the experiments in this thesis, optical quantities must be characterized. For experiments on laser – material interaction, the reflectance gives information about the amount of laser energy entering the silicon. Reflectance for these samples was measured using a spectrometer-based setup from OceanOptics, using an integrating sphere in a one-port setup. Such a setup will introduce a substitution error when the calibration sample has a different reflectance than the sample to be characterized, the substitution error increasing with increasing difference between the reflectance of the calibration sample and that of the measurement sample. For these measurements, polished silicon was used as reference

sample, ensuring that the absolute error when measuring a reflectivity around 5 – 15 % is well below 1 %. As the reflectivity in the case of laser-material interaction experiments only influences the intensity entering the silicon by a small amount, this substitution error is acceptable, and much lower than e.g. the uncertainty in the method by Liu, described in section 2.2.

For measurements on light-trapping structures, on the other hand, greater accuracy is required. For the geometric light-trapping structures, the same spectrometer-based setup was used, but the integrating sphere was replaced with a two-port sphere. This sphere allows for the calibration sample to be mounted at one port and the sample to be mounted at a second port, allowing the sphere as such to remain unchanged between calibration and measurement. This eliminates the substitution error described above.

For the diffractive light-trapping structures (PAPER IV), Jo Gjessing (IFE) performed the optical measurements using a two-port integrating sphere setup as described above, but with a 30 W QTH (Quartz Tungsten Halogen) lamp, using a Digikröm DK240 monochromator from CVI Laser Corporation and a chopper, pre-amplifier and lock-in amplifier for the best signal-to-noise ratio.

The laser intensity dependence of the reflectance has also been estimated through rough measurements. As will be discussed in section 3.3.3, the dielectric response of a material containing a dense plasma of excited electrons may deviate from its steady-state value if the plasma contribution to the dielectric permittivity is considerable. In order to monitor this behavior, the reflectance was measured in-situ while laser processing. For these measurements, the sample was processed at 15° angle of incidence, and the reflected laser power was measured as function of incoming laser intensity using the thermopile power meter described above. This ratio gives the average reflectance. These measurements will be rough, as there is substantial uncertainty in the power measured with the power meter. Furthermore, the measured reflectance will be averaged both in time and over the whole area of the spot. Any diffusely reflected light will not be collected by the power meter. Still, there is a measurable trend towards higher reflectivity when increasing the optical intensity.

## 2.7 MINORITY CARRIER LIFETIME

In order to quantify the effect of laser induced damage, the effective minority carrier lifetime has been measured. Quasi-steady state photoconductance decay (QSSPC)

measurements have been applied, using a WTC-100 setup from Sinton instruments. This technique registers changes in conductivity of a sample under varying illumination, while at the same time measuring the illumination intensity. This gives information about how quickly the carriers decay in the wafer. Photoluminescence imaging (PL) has also been applied, using a LIS-R1 instrument from BTimaging. PL is a quick method for obtaining a spatially resolved lifetime map of a sample. This technique measures the photoluminescence signal from a wafer, and uses a QSSPC measurement to calibrate the relation between the photoluminescence signal and the minority carrier lifetime. The calibration measurement must be performed on a wafer or part of a wafer with relatively homogenous lifetime for good calibration accuracy.

Both of these measurement techniques measure the effective minority carrier lifetime. When measuring the lifetime of a laser processed sample, the inverse effective minority carrier lifetime can be expressed as the inverse sum of lifetime from various recombination mechanisms. Contributions may be divided into surface recombination, bulk recombination, recombination in the laser-damaged areas and any other relevant recombination mechanisms:

$$\frac{1}{\tau_{eff}} = \frac{1}{\tau_{surf}} + \frac{1}{\tau_{bulk}} + \frac{1}{\tau_{laser}} + \cdots . \qquad 2.2$$

In order to isolate the effect of the laser processing, $\tau_{surf}$ and $\tau_{bulk}$ should be large. A large $\tau_{bulk}$ is ensured by using a high-quality substrate while a large $\tau_{surf}$ achieved by applying an efficient surface passivation. As described above, amorphous silicon was used for surface passivation as it gives excellent surface recombination properties. $\tau_{laser}$ is discussed further in Appendix A, Section 3.4 and PAPER VIII.

# 2.8 SILICON SUBSTRATES

Throughout this thesis, polished silicon wafers have been applied. Hermann *et al.* [27] have shown that laser processing of textured substrates may induce more damage than if processing on polished substrates, and as such, the transition to textured surfaces is not expected to be trivial. For the diffractive texture described in section 4.3.2, it may be difficult to spin the microspheres onto non-polished wafers. Also the passivation of rough surfaces may be more difficult than passivating polished surfaces. Still, the use of polished substrates is relevant, firstly, as trends and results may be clearer and easier to interpret,

and secondly, as several of the emerging kerf-less wafering technologies deliver substrates with surfaces that are close to polished in appearance.

# 3 LASER PROCESSING FOR SILICON SOLAR CELLS

This chapter provides a review of the state of laser processing for silicon solar cells. Thereafter, the theory behind laser-material interaction is discussed, and the simulation models are presented. Some of the results from these simulations are presented, along with some thoughts on laser interaction with a free-electron gas. Thereafter, the characterization and quantification of laser damage is discussed.

## 3.1 STATE OF LASER PROCESSING FOR SILICON SOLAR CELLS

In many cases, a laser being directed at a material is nothing but a source of energy or heat. The laser carries energy which may be absorbed by the material, thereby depositing energy into the material. Depending on how much energy is deposited, the material may be heated, melted or vaporized / ablated. This mechanism is the primary mechanism by which lasers may process a material or device.

Laser processing of silicon is not a new idea. In the late 1970's scientists were applying lasers to anneal damage from ion implantation [28]. When annealing, the material, in this case silicon, is heated, normally by an infrared lamp, in order to increase the thermal energy of the atoms in the lattice. Thereby, defects, e.g. atoms that have been moved out of their regular place in the lattice, may diffuse back, restoring the regularity of the crystal. In laser annealing, the energy from the laser causes a controlled, localized heating of the wafer, and it was intended as an alternative to conventional thermal annealing.

For silicon solar cells, one of the primary motivations for applying lasers is the need for local processing, i.e. the need to process only a small part of a solar cell. Lasers show outstanding focusing, translational and temporal properties, making them potent tools

for local processing. A range of laser-related processes for silicon solar cells have been developed, some of which will be briefly summarized below. Some of these processes and their influence on solar cell performance are indicated in Figure 3.1.

*Laser edge isolation*
In a solar cell process, one often obtains a cell where the diffused emitter is wrapped all the way from the front side of the cell to the rear side of the cell, thereby shunting the cell. This shunt must be removed, and lasers may be applied for the process. By removing the emitter by laser ablation around the edge of the solar cell, the shunt is effectively eliminated, and the fill factor, $FF$, is increased [29], [30]. This is shown in Figure 3.1 as a grove through the emitter at the edge of the solar cell. Laser edge isolation is currently implemented in industry.

*Local contact openings*
The metal-semiconductor interface shows a very high rate of electron-hole recombination, and is as such a significant source of efficiency loss in a solar cell. By applying local rear contacts instead of contacting the entire rear surface of a solar cell, recombination losses may be strongly reduced. Reduced recombination increases $V_{oc}$, and also $J_{sc}$, by increasing the fraction of the generated electron-hole pairs that reach the contacts. Local contacts may be created using lasers, simply by applying a laser to locally remove a passivating dielectric layer from the wafer surface, and metallize through these holes, shown in Figure 3.1. The main obstacle for successful implementation of this process is the laser induced damage to the silicon substrate [31–34]. Locally contacted solar cell designs are on their way into industrial production, applying laser opening of the contacts.

*Laser fired contacts*
Laser fired contacts (LFC) is another method for creating local contact openings. In the LFC process, the silicon wafer is covered with a passivating dielectric layer, and the rear contact aluminum is deposited onto this dielectric. Contact with the silicon is created by irradiating this stack with a laser, whereby the aluminum, dielectric, silicon stack melts and the aluminum is forged into contact with the silicon [35], [36]. In this process, the silicon and aluminum are mixed, and aluminum diffuses into the silicon bulk. This creates a so-called back surface field, an electric field that will repel the electron from the recombinative metal-semiconductor surface, thereby strongly reducing recombination also in the metallized areas themselves. Industrial production equipment for LFCs is available [37].

*Laser transferred contacts*

One further way of creating metal contacts using lasers is the Laser transferred contacts or Laser induced forward transfer. In this method, a thin metal foil on a transparent carrier is kept close to the solar cell surface. A laser is irradiated through the transparent carrier, and the metal is ablated from its carrier, being deposited onto the solar cell [38].

*Laser doping*

Laser doping normally occurs through laser heating and melting of a silicon surface covered with a dopant-containing substance, whereby dopant atoms may be rapidly introduced into the silicon material, causing the silicon to become doped. Laser doping of silicon has been performed since the 1980's [39], [40]. Currently, laser doping is most relevant for the application of selective emitters, where doping is only performed on parts of the substrate, in order to form low resistance contacts, while allowing for a lighter emitter doping on the rest of the cell. Selective emitters thereby reduce series resistance, increasing $FF$, while reducing emitter recombination, thereby increasing $J_{sc}$. Several fabrication methods have been proposed. Firstly, doping from a solid state dopant source on the wafer surface may be applied. A spin-on dopant or the phosphorus glass from the emitter doping process may be used as dopant sources [41], [42]. Alternatively, laser chemical processing (LCP) has been proposed, in a method where the laser light is guided to the wafer in a jet of phosphoric acid, the acid serving both as a dopant source, light guide and cooling medium [43]. Also laser transfer doping has been suggested. This is a process similar to laser transferred contacts, where doped amorphous silicon is transferred to the wafer [44]. Selective emitters is shown in Figure 3.1 as a dark grey area under the front contacts. Selective emitters will allow for lower emitter doping on the rest of the wafer surface, thereby reducing recombination losses in the emitter, increasing the collection probability of the short-wavelength part of the sunlight, whereby increasing $J_{sc}$ and $V_{oc}$. Industrial production equipment for selective emitters by laser processing is available [45].

*Laser surface texturing*

Surface texturing increases light-trapping, thereby increasing $J_{sc}$. Several approaches to surface texturing by the use of lasers have been reported. Ultrashort-pulse lasers may be applied for laser texturing. When a silicon substrate is irradiated by multiple ultrashort laser pulses, self-organizing structures begin to emerge. These often cone-like structures reduce the front surface reflectance of the solar cell, in what is often called black silicon

[46]. Alternatively, a macroscopic pattern may be drilled into the wafer, in a process where the laser does the material removal [47]. A third option would be to use an etch mask that is opened locally using a laser, followed by etching through these holes. In this process, the etching does the material removal [48]. Laser surface texturing shall be considered in more detail in chapter 4.

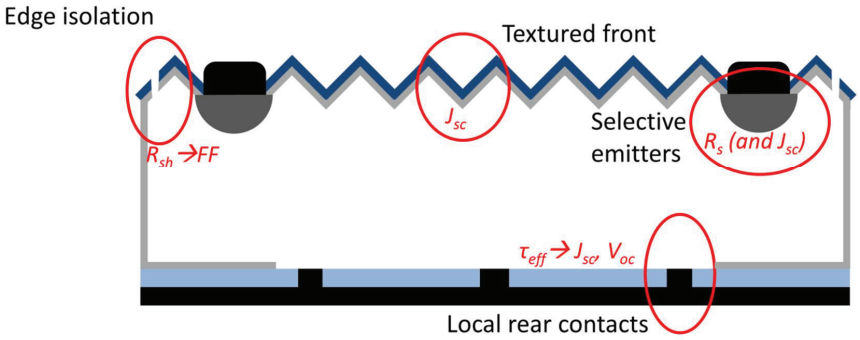


**Figure 3.1: Schematic cross-section of a solar cell, highlighting potential areas for laser processing, and their influence on solar cell performance. The silicon wafer is shown in white, the emitter in light grey, local over-doping under the contacts in dark grey, anti-reflection coating in dark blue, rear surface passivation layer in light blue, contacts in black. Residual laser damage may be present in all laser processes.**

*Alternatives to laser processing*

For the processes mentioned above, alternatives that do not apply lasers exist. Edge isolation may be performed by etching of the edges of the cell [49]. Selective emitters may be formed e.g. by creating a thick emitter over the whole wafer surface followed by a masked etch, whereby the thick selective emitter is left under the contacts, while the emitter is thinned over the rest of the wafer [50], or by applying doping from locally printed dopant sources [51]. Local contacts may be formed e.g. by dispensing the metallization paste in a pattern ensuring that the silicon-metal contact is formed only locally [52]. Surface texturing is currently performed by wet-chemical etching, but also reactive ion etching (RIE) and microwave plasma etching may be applied [53], [54]. Laser processing is not automatically beneficial for the solar cell, as it may damage the quality of the solar cell materials, e.g. by introducing defects into the silicon, thereby increasing recombination, and decreasing $V_{oc}$. As such, laser processing is only relevant in cases where the laser process outperforms the alternative in terms of overall increase in cell efficiency, process simplicity, or cost.

From the overview given in this section, it is seen that the interaction between laser and material can give rise to a wide variety of processes. It is also seen that the damage to

the material resulting from the laser process must be under control for successful process implementation. As such, knowledge about the laser-material interaction is crucial, as is knowledge about the laser induced damage. The next sections are devoted to these topics.

## 3.2 LASER-MATERIAL INTERACTION

One of the main topics of this thesis is the laser-material interaction. The silicon, or a silicon–dielectric stack, is irradiated with laser pulses, and the laser light is absorbed. How and where this absorption takes place, combined with the properties of the irradiated materials and the laser parameters, such as pulse duration, laser wavelength and laser intensity distribution determines the outcome of the laser processing. In order to predict experimental trends or understand experimental results, it is relevant for us to understand the laser–material interaction in detail.

For the case of silicon, there is an observable change in processing results when reducing the laser pulse duration. A transition happens somewhere between nanosecond ("long") and picosecond ("ultrashort") pulse duration. Some typical process results when removing silicon nitride from silicon is seen in Figure 3.2, showing SEM images of processing with long and ultrashort laser pulses in the UV (343 / 355 nm), visible (515 / 532 nm) and infra-red (IR) (1030 / 1064 nm). The ultrashort pulse laser operates at the shorter wavelengths. Starting with long pulses in the visible wavelength range, the result is a molten area in the silicon, however, with relatively homogenous size. Long pulses have time to melt a significant amount of silicon, and re-distribution, i.e. pits and silicon expulsion is frequently observed. Looking at long pulses in the IR, the situation is somewhat similar, the melting is clearly visible. However, the pulse to pulse variation in processing result is much larger. This as a result of the inherent instability of the process. When cold, silicon is nearly transparent to this wavelength, with the laser light penetrating several hundred micrometers. However, some of the laser light is still absorbed. The silicon is slowly heated to the point where it absorbs strongly, whereby the deposited energy density strongly increases and enough energy is deposited to melt and vaporize the material. This feedback mechanism makes processing near the process threshold unstable, as the onset of absorption may depend on local material parameters. At shorter wavelengths, the picture changes. In the UV, the laser energy is absorbed by the $SiN_x$, decomposing this. However, the image shows an inhomogenous process result. This is an indication that some of the laser light penetrates to the silicon, with the possibility that the

silicon is vaporized and expels some of the $SiN_x$. Experiments have also been performed at 266 nm, where the $SiN_x$ absorbs even stronger. Here, the instabilities observed when processing at 355 nm are not observed, as very little laser light will penetrate to the silicon. With ultrashort laser pulses, the picture changes somewhat. In the UV, the $SiN_x$ still absorbs, but no instabilities are observed. Also in the visible and IR, the process results are, in general, much more homogenous. Furthermore, the obvious signs of melting and expulsion are gone, leaving a seemingly flat wafer surface. Whether using a pulse duration of 0.5 ps or 10 ps, the process results look similar when observed by SEM. Processing in the far-IR using long pulses gives process results resembling those observed with pulses in the IR, as similar heat-dependent feedback-mechanisms are dominant also here, and as the pulses are long enough for material expulsion and redistribution.

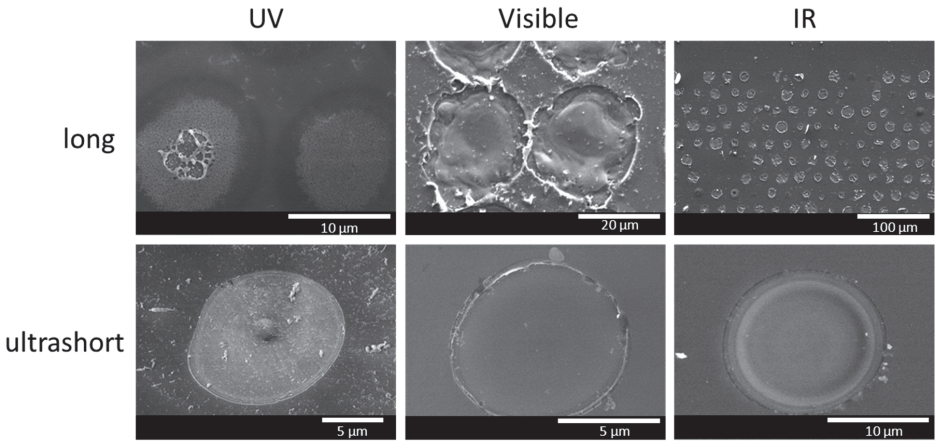


**Figure 3.2: Typical process results when irradiating a silicon nitride on silicon stack with long and ultrashort laser pulses at 355 (UV), 532 (Visible) and 1064 nm (IR).**

Above, it is stated that the laser light may be deposited into the $SiN_x$ if the wavelength is short enough. Using ultrashort laser pulses, it can sometimes be rather straightforward to see where the energy has been deposited. Figure 3.2 shows that when processing in the UV using ultrashort laser pulses, the surface is covered in fine debris. In this case, the energy is deposited into the $SiN_x$, and the $SiN_x$ is blown apart upon removal. This is in contrast to what is the case e.g. in the visible wavelength range, where the laser energy is deposited into the silicon. Here, it is frequently observed that the $SiN_x$ which is blown off remains in one single piece that can be found elsewhere on the wafer upon inspection. This is shown in Figure 3.3.

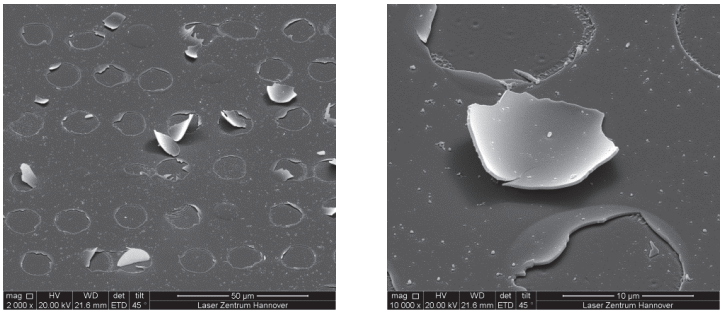


**Figure 3.3: SEM images of complete pieces of $SiN_x$ removed from the wafer surface using ultrashort pulses in the visible wavelength range. (Left: Overview, Right: closeup)**

As the mechanism for ablation is different in these two situations, a distinction shall be made. The process where the laser energy is deposited in the substrate, and the film is lifted off by the vapor pressure substrate shall be referred to as indirect ablation. On the other hand, if the energy is deposited into the film, we shall refer to the process as direct ablation.

Not only the appearance of the processing result changes when reducing the duration of the laser pulses. Also the physics of the interaction will change. Generally, the laser energy is absorbed by the electrons in the material, moving these to an excited state. When applying long laser pulses, this energy has time to dissipate to the lattice through collisions, whereby the electrons relax into less excited states. As such, there is equilibrium between the electron and lattice systems, the number density of excited electrons will remain moderate. There is also enough time for the heat to be transported a significant distance from where it is deposited.

This picture changes when going to ultrashort laser pulses. Now, the electrons will not have time to transfer their energy to the lattice before the pulse is through, and as such, the electrons may have significantly higher energy than the lattice during the pulse. Non-linear absorption may be encountered, meaning that the absorption is changing with the intensity of the applied light. The excited electrons in the conduction band may absorb light through free-electron absorption, and they may promote further electrons to the conduction band through impact ionization. Furthermore, the electrons may not have time to relax into less excited states, and very high densities of highly excited electrons may be obtained. If dense enough, this electron cloud may start to behave as a plasma, significantly altering the physical properties of the material. Furthermore, thermal diffusion is strongly limited when applying ultrashort laser pulses. Clearly, very different models are required when treating laser-material interaction with long or with ultrashort laser pulses.

## 3.3 SIMULATIONS ON LASER-MATERIAL INTERACTION

Simulation of laser-material interaction is a rather complex task. The process is three-dimensional, and if considering material transport, such as convection in a molten material or even ablation, i.e. material removal, the simulations get extremely large and time-consuming. For ultrashort laser pulses, many optical, electrical and thermal properties of the materials to be simulated are uncertain and must be applied far from equilibrium, in a material that is under influence of tremendous stress. It was chosen to apply somewhat simplified models in this thesis, in order to gain physical insight while keeping model complexity to a minimum.

For the simulations, one important parameter is the ablation threshold fluence, as this is the fluence required for the process to take place. Criteria for ablation are required in order to determine this ablation threshold. For long laser pulses, it is assumed that material is removed only if some material reaches vaporization temperature. Vaporization will remove material in itself, but it will also create recoil pressure that will expel more material. At fluencies close to the ablation threshold, the majority of the material will be removed through expulsion [23]. This ablation threshold will be valid both for long and ultrashort pulses. With ultrashort laser pulses, there may also exist other ablation mechanisms, as discussed in PAPER V. These mechanisms are connected to the point where a high number density of excited electrons creates a strongly absorbing plasma in the material. As such, in the case of ultrashort pulses, the second criterion for ablation is when the critical electron density is reached.

Two significant physical mechanisms are left out of the simulations, namely material removal and convection. When material is expelled from the melt pool or in other ways removed from the substrate, it will carry with it some of the laser energy. Furthermore, convection and stirring within the melt pool will alter the dynamics of the process. While it would be interesting to investigate these mechanisms as well, it would be outside the scope of this thesis. Still, some considerations can be made. Convection and stirring only has time to take place for long pulses. Generally, convection and stirring within the melt pool will decrease the vertical temperature gradient within the melt pool. The bottom of the melt pool will be hotter, potentially increasing the melting rate for the solid material surrounding the melt pool. As such, convection and stirring may increase the

obtained depth of the melt pool. At the same time, the surface temperature will be reduced, increasing the threshold for ablation. On the other hand, material removal will carry with it some of the laser energy, reducing the energy stored in the wafer, hence reducing the thermal impact to the wafer. Quantification of these effects would be difficult, however, Mangersnes *et al.* [55] have performed simulations omitting these effects, still obtaining good correspondence between simulations and experiments. This seems to indicate that the effect of convection and stirring may be minor when seeking to determine the ablation threshold fluence.

For the simulation of both long and ultrashort laser pulses, the partial differential equation solver pdepe [56] was applied. This is included as a standard routine in Matlab [57]. One approximation performed in all simulations is that the physical situation is one-dimensional. This implies that the laser irradiation is homogenous and the laser spot is infinitely large. This is of course not the case, however, the approximation is reasonable. The laser spot is normally on the order of 40 μm in diameter, while the laser energy is deposited within 1 μm from the wafer surface, sometimes within the first 0.1 μm from the surface. As such, the lateral length scale is much larger than the length scale into the substrate.

The pulses were assumed to have a Gaussian temporal distribution, with the pulse duration being the full-width half-maximum (FWHM) duration. The surface reflectivity was set to zero, looking at the optical intensity entering the material. This as the reflectivity can be changed rather arbitrarily by the application of suitable (anti-)reflection coatings.

### 3.3.1 LONG PULSES

Using long laser pulses, the absorption in the material is given by the linear absorption coefficient of the material. The temperature rise of the material is given by laser energy input, heat capacity and heat conductivity. The heat equation is given by [23]:

$$\frac{\partial U_l}{\partial t} = C_l \frac{\partial T_l}{\partial t} = \frac{\partial}{\partial x}\left(\kappa_l \frac{\partial T_l}{\partial x}\right) + \alpha I \qquad 3.1$$

where $U_l$ is the thermal energy of the material, $C_l$ is the heat capacity of the lattice, $T_l$ is the temperature, $\kappa_l$ is the thermal conductivity and $\alpha$ and $I$ are the optical attenuation coefficient and intensity respectively. This equation describes how the thermal energy of the system changes as a result of thermal conduction and as a result of energy input from optical absorption. The optical intensity distribution follows the Beer-Lambert law:

$$\frac{dI(t)}{dx} = -\alpha(T)I(x,t) \qquad \rightarrow \qquad I(x,t) = I_0(t)\, exp - \int_0^x \alpha(T(x'))\, dx' \qquad 3.2$$

with a constant $\alpha$, this expression gives an exponentially decaying intensity. However, $\alpha$ is generally temperature dependent. With temperature dependent $\alpha$, there is a feedback mechanism. Optical absorption causes a temperature rise, which again causes a change (normally an increase) in absorption by changing $\alpha$. Phase changes are taken into account by modifying $C_l$ into containing the enthalpy of phase change. The model developed by Mangersnes *et al.* [55], [58] was applied for simulations on long laser pulses in the visible wavelength range.

#### 3.3.1.1 Long laser pulses at long wavelengths

Semiconductors are generally considered to be transparent, for all practical purposes, for photon energies below the band-gap of the material, as the photon does not carry enough energy to bridge the band-gap. However, in some cases, free-carrier absorption may become relevant. Free carrier absorption is absorption by carriers in the conduction band, and has an absorption coefficient described by

$$\alpha_{fca} = \theta N \qquad 3.3$$

Normally, this effect is very weak, as the number density of conduction band electrons is fairly small. However, if the temperature of the semiconductor is high enough, a significant number of thermally excited electrons will exist. In addition, the free-carrier absorption coefficient $\theta$ generally increases with $\lambda^2$, meaning that this effect will be very pronounced at long wavelengths. With high temperature substrates and long wavelengths, free-carrier absorption may be strong, as is discussed in PAPER VII.

The model developed by Mangersnes *et al.* [55], [58] was adapted to be suitable for the absorption encountered at a wavelength of 9.3 µm, as discussed in PAPER VII. No experimental investigation was found describing the temperature dependence of the absorption in silicon at 9.3 µm. As such, a theoretical expression was used. In PAPER VII the temperature dependence of the free carrier absorption is described as

$$\alpha_{fca}(N,T) = \alpha_{fca}(10^{16},300) \times \frac{N(T)}{10^{16}} \times \frac{\mu(10^{16},300)}{\mu(N,T)}. \qquad 3.4$$

Here, $\alpha_{fca}(N,T)$ is the free-carrier absorption (FCA), the only contribution to absorption that is taken to be temperature dependent. Starting with FCA at room

temperature, the temperature dependence comes from the temperature dependence of the number density of conduction band electrons, $N(T)$ and from the temperature dependence of the mobility, $\mu(N,T)$. These two quantities have not been investigated close to the melting point of silicon, where the simulations are most sensitive to the value of $\alpha_{fca}$. This constitutes a serious source of uncertainty in the simulations. Another source of error is the thermal interface resistance between the dielectric and silicon. This quantity is taken to be temperature independent, however, at least when the dielectric melts, the interface thermal resistance must be expected to change. The paper also clearly shows that correspondence between simulations and experiments is rather poor, the only result that should be valid is that shorter pulses will allow for less heat transfer to the silicon substrate.

As for the experimental investigations of laser ablation by $CO_2$-lasers, the lack of lasers with shorter pulse durations has excluded the exploration of potentially very interesting parameter ranges.

### 3.3.2 *ULTRASHORT PULSES*

The term ultrashort pulses has probably arisen from the need of a counterpart to the rather short pulses in the nanosecond range, which are in this context regarded as "long". Normally, the term "ultrashort pulses" is applied to pulses with a duration in the pico- and femtosecond range. Here, "ultrashort pulses" is taken to mean pulses where non-linear interaction is expected to be a significant part of the physics, but where the assumption that the extension of the pulse is large compared to e.g. optical absorption lengths etc. is still valid. This will hold well for pulse durations down to 0.5 ps, the shortest pulses applied within this thesis, having an extension in silicon of about 35 µm. As described in section 3.2, ultrashort laser pulses call for a different physical model than long pulses. As a result of the potentially different temperature in the electron and lattice systems, two coupled heat equations are required in order to describe the system, one for the electrons and one for the lattice, following the work by Sim *et al.* [59] and van Driel [60]:

$$\frac{\partial U_e}{\partial t} = \frac{\partial}{\partial x}\left(\kappa_e \frac{\partial T_e}{\partial x}\right) - \frac{3Nk_b}{\tau_{e-l}}(T_e - T_l) + q_{tot} \qquad 3.5$$

$$\frac{\partial U_l}{\partial t} = \frac{\partial}{\partial x}\left(\kappa_l \frac{\partial T_l}{\partial x}\right) + \frac{3Nk_b}{\tau_{e-l}}(T_e - T_l) \qquad 3.6$$

In equations 3.5 and 3.6, $U_{e/l}$, $T_{e/l}$ and $\kappa_{e/l}$ are the thermal energy, temperature and heat conductivity of the electron/lattice system, respectively. $\tau_{e-l}$ is the electron-lattice

coupling time, $q_{tot}$ is the total energy input from the laser, $N$ is the number density of conduction band electrons and $k_B$ is the Boltzmann constant. As the number density of electrons is not constant, but is changing through generation and recombination mechanisms, the number density of electrons must be accounted for, adding a third coupled equation:

$$\frac{\partial N}{\partial t} = \frac{\partial}{\partial x}\left(D_0 \frac{\partial N}{\partial x}\right) - \gamma N^3 + \delta N + \sum \frac{a_n I^n}{n\hbar\omega} \qquad 3.7$$

Here, $D_0$ is the electron diffusivity, $\gamma$ is the Auger coefficient, $\delta$ is the impact ionization coefficient, $a_n$ is the n-th order absorption coefficient and $\hbar\omega$ is the photon energy. The total energy input from the laser is:

$$q_{tot} = \alpha_{eff} I = (\sum a_n I^{n-1} + \theta N) I \simeq (\alpha + \beta I + \theta N) I \qquad 3.8$$

where the summation indicates all relevant multi-photon absorption processes, and the last term is the free-carrier absorption. $\beta$ is the two-photon absorption coefficient. When working on silicon, linear absorption, two-photon absorption and free-carrier absorption will be the dominant processes. Two-photon absorption is the simultaneous absorption of two photons, and is a mechanism which has an absorption coefficient that is proportional to the optical intensity. Two photon absorption may induce absorption in materials where the photon energy is not high enough to bridge the band-gap, but where two photons combined have sufficient energy, or it may increase absorption significantly in cases where linear absorption is weak, e.g. for photon energies close to the band-gap energy in silicon.

Looking at the equations, it is clear that the laser energy is deposited into the electron system, while the electron-lattice coupling term causes an energy flow between the hotter electron system and the colder lattice system until the two reach equilibrium. Impact ionization and band-to-band absorption cause an increase in the number density of conduction band electrons, while Auger recombination removes electrons. Free-carrier absorption does not contribute to the number density of conduction band electrons, but causes an increase in the temperature of the electron system. The absorption in the medium becomes dependent both on the optical intensity and on the number density of conduction band electrons.

In the model described above, the expressions for optical absorption and assumptions on constant optical reflectivity break down when approaching the critical electron density, as a result of the free-electron contribution to the dielectric constant of the

material. This implies that anything happening to the substrate after this point, such as phase transformations and material removal is not accurately described in the simulations. In fact, the physics behind melting or disordering mechanisms resulting from ultrashort-pulse irradiation of semiconductors is quite complex. Several authors have pointed towards melting of the semiconductor (as opposed to e.g. Coulomb explosion) [61], and that the melting turns non-thermal by ultrafast disordering mechanisms if the laser fluence is sufficiently above the melting threshold [62], [63]. Also breaking of the material resulting from internal stress caused by the strong temperature gradients obtained by ultrashort laser pulses has been suggested as material removal mechanism [64].

Other mechanisms that are not considered within the two-temperature model are the incomplete thermalisation between optical and acoustic phonons, the electric field arising within the material due to electron emission and modification of material properties due to deformation of the material itself [64], [65]. While these mechanisms have an influence on the interaction dynamics, this thesis focused on obtaining meaningful results while keeping the complexity of the model and the number of uncertain material parameters to a minimum. Results in PAPER V indicate that the main physical mechanisms are included also in the two-temperature model, and that the choice of model as such is a sensible one.

The pdepe solver is able to solve sets of coupled partial differential equations. However, the expression for optical intensity cannot be explicitly obtained, and needs to be found from the integral expression in equation 3.2. In order to make the solution converge, a set of iterations are implemented. Firstly, a temperature distribution and distribution of number density of electrons are set as functions of time and space coordinates, assuming quite limited heating and excitation. From these distributions, the optical intensity is calculated as function of time and space, starting with quite low incoming optical fluence. Then, this optical intensity distribution is used as the source term in the equations. When a solution is found, the temperature and electron distributions are used to re-calculate the intensity distribution, and repeat until the solution converges. Thereafter, the incoming optical fluence is increased by a certain $\Delta F$, and the previously found temperature and electron distributions are again used to calculate the optical intensity distribution, and the procedure is repeated.

These iterations are repeated until one of the criteria for ablation is reached. These criteria are discussed in section 3.3, and are that the lattice reaches vaporization temperature, or that the number density of electrons in the conduction band reaches the

critical electron density, $N_{cr}$. Then, the $\Delta F$ is reduced, until two pulse fluencies are found, one being above the ablation threshold and one below, and the difference between them is lower than 3 %.

#### 3.3.2.1 Some results from the simulations

Figure 3.4 shows the optical intensity normalized to the intensity at the wafer surface as a function of depth into the silicon wafer, in order to illustrate the optical attenuation. The figure shows data for a laser wavelength of 1030 nm, 0.575 J/cm$^2$ and a substrate temperature of 300 K. The pulse duration is 3 ps (FWHM). Three curves are shown, at 3 ps before the peak of the pulse, at the peak of the pulse, and at 3 ps after the pulse. At 3 ps before the pulse, both the optical intensity and the number density of excited electrons are low, and hence the relatively weak linear absorption dominates. This gives only very moderate absorption. At the peak of the pulse, the optical intensity is very high, and the absorption is dominated by two-photon absorption. At 3 ps after the pulse, the optical intensity is equal to the intensity at 3 ps before the pulse, and linear and two-photon absorption are in principle equal in these two cases. The fact that highest absorption is observed at the trailing end of the pulse indicates that free-carrier absorption is dominant late in the pulse. (Heating of the silicon will increase the linear absorption coefficient late in the pulse, but this effect is less dominant than the effects described above.) It is clear that, at least for the case of IR-irradiation of silicon using ultrashort pulses, the laser energy is confined close to the silicon surface when the laser intensity and number density of electrons rise. Also shown in Figure 3.4 is the same data for a pulse with a laser wavelength of 515 nm. Although the absorption increases with time during the pulse, probably as a result of free-carrier absorption, the difference is less prominent than for 1030 nm laser wavelength.

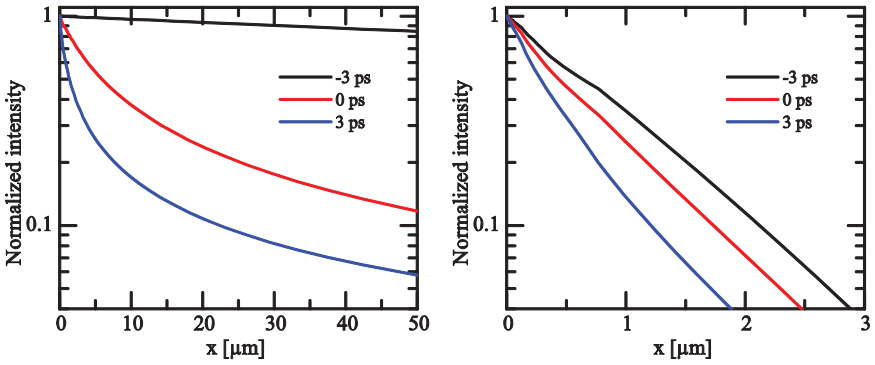


**Figure 3.4: Normalized intensity distribution through a silicon slab at various times during a laser pulse of 3 ps duration. The laser wavelength is 1030 nm (left) and 515 nm (right). Non-linear absorption mechanisms are far more prominent for the case of irradiation at 1030 nm, as the linear absorption is quite strong at 515 nm. Note the differences in x-scale.**

## 3.3.3 FREE ELECTRON THEORY

In a dielectric or semiconductor, a high number density of electrons in the conduction band can be generated e.g. by optical excitation. These electrons (and their corresponding holes in the valence band) are quasi-free, and may be described as a plasma. The dielectric response of the material will be affected by the presence of such a plasma, and free-electron theory may be applied in order to describe this response. Free-electron theory is treated in PAPER V, however, this field shall be reviewed here in some more detail. The dielectric response of a material can, in free-electron theory be described by [66], [67]:

$$\epsilon = \epsilon' + i\epsilon'' = \epsilon_{bg}\left(1 - \frac{\tilde{\omega}_p^2}{\omega^2+\gamma^2}\right) + i\frac{\epsilon_{bg}\tilde{\omega}_p^2\gamma}{\omega(\omega^2+\gamma^2)} \qquad 3.9$$

where $\epsilon_{bg}$ is the background relative permittivity of the silicon material without free carriers. Here, $\tilde{\omega}_p$ is defined as

$$\tilde{\omega}_p^2 = \frac{Ne^2}{\epsilon_{bg}\epsilon_0 m_{eff}}, \qquad 3.10$$

being the plasma frequency with a dielectric background. $\gamma$ is the reciprocal collision time, $m_{eff}$ is the effective electron mass and $\omega$ is the frequency of the applied electric field. With

$$n + ik = \sqrt{\epsilon}, \qquad 3.11$$

the Fresnel reflection can be calculated as

$$R = \frac{(n-1)^2+k^2}{(n+1)^2+k^2} \qquad 3.12$$

for normally incident light on a substrate with index of refraction $n$ and extinction coefficient $k$. Depending on the ratio between $\omega$, $\tilde{\omega}_p$ and $\gamma$, the reflectance as function of number density of electrons can show different shapes. This has effects for laser processing with ultrashort pulses. Figure 3.5 shows the theoretical reflectance curves as functions of electron density in silicon and silicon nitride for the case of irradiation at a wavelength of 515 nm. Silicon has a high index of refraction, giving high reflectivity for the case of low electron densities, while silicon nitride has a lower index of refraction. Now, $\gamma$ is related to the mobility of the material. Using a mobility of 100 $cm^2/Vs$ in silicon (high carrier density [68]), and 1 $cm^2/Vs$ in silicon nitride [69], it is evident that the reflectance behavior at high electron densities is very different in the two cases.

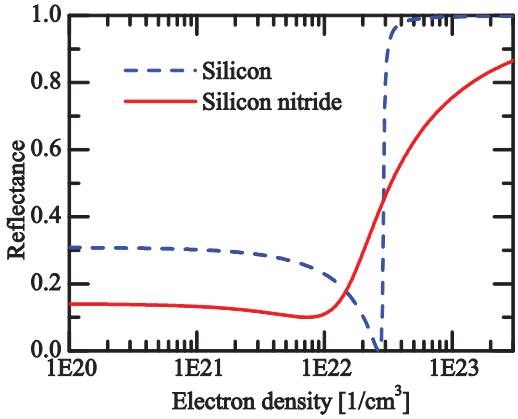


**Figure 3.5: Theoretical reflectance as function of free electron density in silicon and silicon nitride. The shape of the curves is very different in the two cases, as a result of the different ratio between $\omega$, $\tilde{\omega}_p$ and $\gamma$. Silicon has a fairly high electron mobility (resulting in $\gamma \ll \omega$), while silicon nitride has a fairly low electron mobility (resulting in $\gamma \gg \omega$). As such, the plasma response in silicon is dominated by the rapidly alternating electrical field, while the response in silicon nitride is dominated by collisions within the material. This difference results in a well-defined plasma frequency in silicon, while the increase in reflectance is much slower for silicon nitride.**

The fairly high electron mobility in silicon results in $\gamma \ll \omega$, while the fairly low electron mobility in silicon nitride results in $\gamma \gg \omega$. As such, the plasma response in silicon is dominated by the rapidly alternating electrical field, while the response in silicon nitride is dominated by collisions within the material. This difference results in a well-defined plasma frequency in silicon. The reflectance drops when approaching the critical electron density, increasing rapidly to unity thereafter. In this situation, it will be very difficult to introduce more laser energy into the material once the critical electron density has been

reached, as the laser light will be completely reflected. For the case of silicon nitride, on the other hand, the reflectivity varies more slowly. Here, it will always be possible to continue laser energy input.

# 3.4 LASER INDUCED DAMAGE

When laser processing silicon, the material is normally heated and molten, or in some other way structurally altered. The process result will be a silicon wafer with some degree of crystal damage, as re-crystallization or re-structuring seldom is damage-free. It can be expected that the area influenced by the laser process will be degraded in some way, and this degradation will have a negative influence on the solar cell performance.

In order to get a view on the quality and applicability of the laser process, the laser damage must be quantified in some way.

This section considers methods for characterization of laser induced damage, and the influence on effective minority carrier lifetime from a laser damaged area is analyzed.

## *3.4.1 CHARACTERIZATION OF LASER-INDUCED DAMAGE IN SILICON*

The quality of a solar cell is closely linked to its efficiency, where the highest possible efficiency is desirable. Any process reducing the efficiency of the cell must therefore outweigh this efficiency decrease by some other benefit, often lower production costs. Laser processing of silicon solar cells is one such process with the potential to reduce the efficiency of the cell, and ideally, the efficiency of a cell with laser processing should be compared to a damage-free reference process in order to quantify laser-induced damage. However, it is not always desirable, practical or even beneficial to create complete solar cells and monitor the resulting efficiency, and often more indirect ways of quantifying laser-induced damage are applied. In this section, some methods for characterization of laser damage are discussed.

When looking at a silicon wafer, one important material parameter influencing the potential efficiency of a solar cell made from that wafer is the minority carrier lifetime. Laser damage may reduce this lifetime, decreasing the maximum potential efficiency of the finished solar cell. This reduction in lifetime comes from the introduction of recombination sites, such as various crystallographic defects. Whether using long laser

pulses resulting in melting and recrystallization of silicon or ultrashort pulses where the material processing may take place by ultrafast disordering mechanisms, the resulting crystal quality must always be considered. Especially in the case of ultrashort pulses, one is often lead to believe that the ablation may be completely damage-free, as redistribution of silicon may be suppressed, and the process result may look very smooth and clean. Transmission Electron Microscopy (TEM) is rather frequently used for investigation of laser damage, and may reveal seemingly perfect silicon crystals under such ablation spots. However, TEM is not necessarily the best suited characterization tool for finding defects which may be small and low-concentration. A good example is shown in Figure 3.6. This figure shows TEM images of cross-sections of ablation spots from irradiation by a nanosecond laser at 1064 nm wavelength on an atomic scale. As shown by Engelhart *et al.* [21], such a laser produces electrically active defects down to around 25 µm below the wafer surface, while the TEM images show amorphous silicon at the surface of the wafer, and very good crystal quality below a couple of tens of nanometers. TEM is unable to reveal the damage leading to reduced lifetime, which may not be very surprising. As shown by Davis *et al.* [70], electrically active defects may affect silicon solar cell performance even at defect levels between $10^{11}$ and $10^{16}$ 1/cm$^3$, corresponding to a defect level of less than one ppm (and potentially much lower). Although the density of defects in a laser treated area is unknown, it is not impossible that one is looking for one defect among a million silicon atoms, a task that is impossible for TEM analysis. As such, it seems obvious that electrical characterization is imperative in order to quantify laser damage.

One way of quantifying laser damage is to measure the effective lifetime of a laser-irradiated wafer as described in section 2.7. The laser damage will result in a lowering of the lifetime, potentially revealing information about the extent of the laser damage.

During this thesis, several experiments have been performed ablating $SiN_x$ from silicon wafers using lasers with pulse duration from ~100 ns to 500 fs and from UV to IR, and the effective lifetime of these samples has been measured. However, it was observed in all of these experiments that the effective lifetime was the same, and corresponded to the lifetime of a single sided diffusion limited surface recombination. This behavior shall be discussed in further detail.

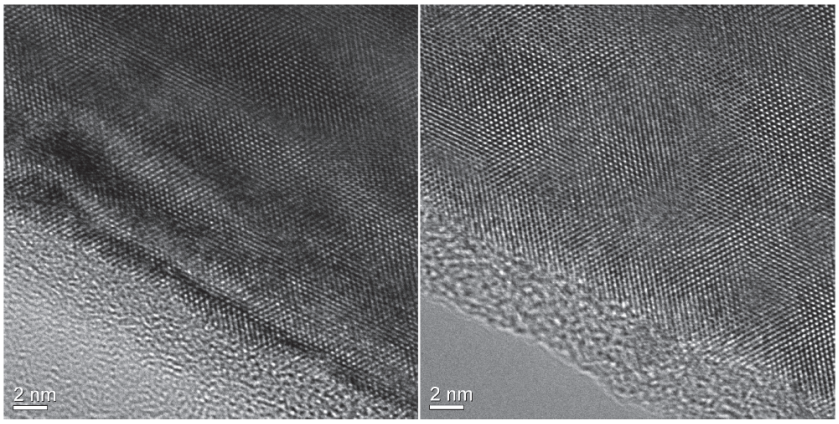


**Figure 3.6: TEM images of silicon wafer irradiated by nanosecond pulses with a wavelength of 1064 nm. The images show cross-sections of the laser spot, where an amorphous silicon layer can be observed in the lower-left corners (near the wafer surface), and an ordered silicon crystal in the upper-right part of the images. (TEM performed by Annett Thøgersen, UiO.)**

Consider a wafer with a bulk lifetime $\tau_{bulk}$, and surface recombination velocities $S_1$ and $S_2$. Now, introduce a laser damaged region close to one wafer surface, as shown in Figure 3.7. To a first approximation, it is assumed that the wafer has been degraded to a certain depth below the wafer surface, and that in this region, the lifetime has been lowered to the value $\tau_{laser}$. In this situation, a recombination current will flow into the laser damaged area. Inserting a virtual boundary between the laser damaged area and the undamaged bulk, it is possible to assign an effective surface recombination velocity to the recombination caused by the laser damage, $S_{laser}$. In Appendix A, such an expression is derived, assuming that $S_2$ is small compared to the recombination taking place in the laser damaged bulk. In this case, $S_{laser}$ is given by:

$$S_{laser} = \sqrt{\frac{D}{\tau_{laser}}}\, tanh\left(\frac{w}{\sqrt{D\tau_{laser}}}\right). \qquad 3.13$$

where $D$ is the electron diffusion coefficient and $w$ is the width of the laser damaged region. With $\sqrt{D\tau_{laser}} \gg w$, i.e. if the laser damaged region is much thinner than the diffusion length, this expression goes to zero. If, on the other hand, $\sqrt{D\tau_{laser}} \ll w$, i.e. if the laser damaged region is much wider than the electron diffusion length, this goes to $\sqrt{D/\tau_{laser}}$. According to Sproul [71], the surface lifetime reaches a limiting value of $\tau_{s,min} = \frac{4}{D}\left(\frac{W}{\pi}\right)^2$ when $S_{laser} > 10^5$ cm/s.

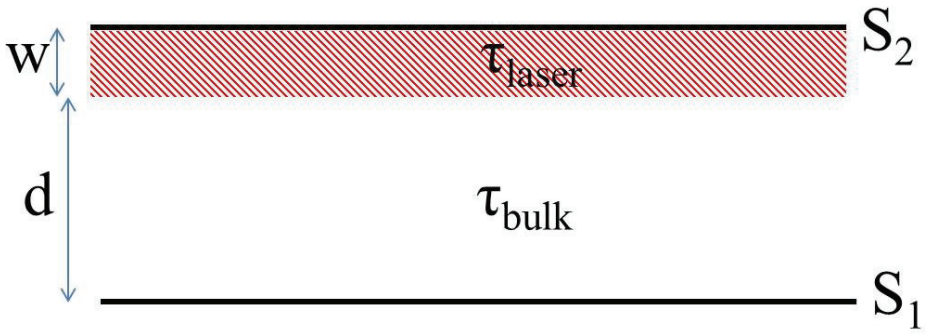


**Figure 3.7: Schematic representation of a wafer with a laser damaged region. The laser damaged region has a width w and a lifetime $\tau_{laser}$.**

However, the depth of the laser induced damage is still unknown. PAPER VIII describes measurements on lifetime in laser-irradiated silicon wafers as function of etch depth. By removing a controlled thickness of the laser damaged region, the effective lifetime of the wafer will increase, until the point where the complete laser damage has been removed, and the bulk lifetime is restored. Equation 3.13 can be used to extract $\tau_{laser}$ from the behavior of the experimentally determined $\tau_{eff}$ as described in section A.3. In PAPER VIII, it is found that, using a laser wavelength and pulse duration of 515 nm and 3 ps, the lifetime is completely restored when removing 230 nm from the wafer surface, and that the lifetime in the laser damaged region must be on the order of 1 ns. For long pulses, geometric factors are taken into account, and $\tau_{laser}$ is estimated to around 100 ns. In PAPER VIII, it is also found that, while nanosecond lasers show damage several micrometers from the surface, ultrashort laser pulses show damage confined to a much more shallow depth. These findings can be implemented in simulation models predicting the efficiency decrease that can be expected from the laser process.

In samples with emitters, the measured effective lifetime is strongly reduced, due to recombination in the emitter. As a result, the laser-induced lifetime degradation is not necessarily as pronounced as with lowly doped silicon. In this case, one should rather use the dark saturation current density, as this can be related directly to the achievable open circuit voltage, $V_{oc}$ [31], [72]. Also analysis of the diode ideality factor can give information about the damage [27]. Such analysis has not been performed within this thesis.

# 4 LIGHT-TRAPPING STRUCTURES IN SILICON SOLAR CELLS

This chapter motivates the use of light-trapping structures in silicon solar cells and presents the benefits of light trapping. Then, some typical light-trapping structures are shown, followed by a description of some of the alternative routes to fabrication of light-trapping structures using lasers. Thereafter, the approach taken in this thesis to the fabrication of light-trapping structures using lasers is presented. Finally, the results and the applicability of the textures are discussed.

## 4.1 LIGHT MANAGEMENT IN SILICON SOLAR CELLS

In a solar cell, one major task is to make sure that as much as possible of the incoming sunlight is converted into electricity. In order to achieve this, optical losses must be reduced as much as possible. The effort of reducing these losses is termed light management. Figure 4.1 shows a sketch of possible optical losses in a silicon solar cell. $R_f$ denotes the front surface reflection, which consists of the light being reflected off the front surface without entering the solar cell. $R_{esc}$ denotes the escape light, light which has entered the solar cell, but is able to escape before being absorbed. Three parasitic absorption mechanisms, absorption that does not generate current in the solar cell, are also indicated. $A_{Reflector}$ denotes optical absorption in an imperfect rear mirror, free-carrier absorption, $A_{FCA}$, is the absorption by conduction band electrons, an optical absorption mechanism which does not generate electron-hole pairs. This mechanism is intrinsic to silicon, and is strongest in highly doped silicon, such as in the emitter. Also the anti-reflection coating may absorb some of the incident light, here denoted as $A_{ARC}$.

With a quite high index of refraction, bare silicon reflects on the order of 30 % of the incoming sunlight due to Fresnel reflection. In order to reduce $R_f$, two tricks are normally applied. Firstly, an anti-reflection coating can be applied to the surface, consisting of a transparent layer with a thickness of $\lambda/4$ and an index of refraction ideally equal to $\sqrt{n_{Si}}$, thus minimizing or eliminating reflection at the target wavelength, and significantly reducing overall reflection. (For an introduction to Fresnel and thin-film optics, see e.g. [73].) Typically, when weighting the reflectance spectrum with the AM1.5 spectrum, integrating over a 300 – 1200 nm wavelength range, an integrated reflectance of around 10 % can be achieved by application of an anti-reflection coating. Secondly, texturing of the surface may further increase the optical coupling into the silicon. If the light experiences multiple bounces off the silicon surface, each bounce will reduce the total reflectance.

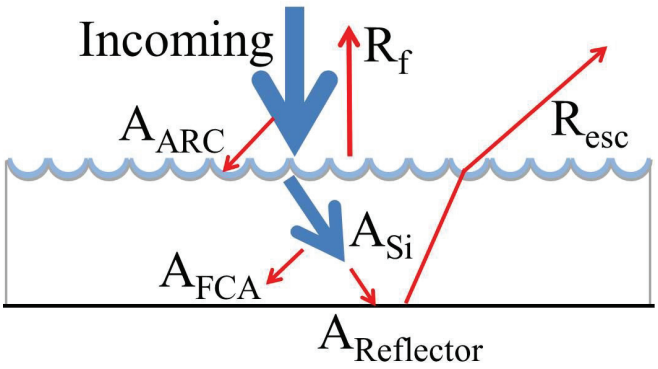


**Figure 4.1: Sketch of a wafer showing various contributions to optical absorption and loss in a solar cell. The rear reflector is shown in black, while the anti-reflection coating is shown in blue. $A_{Si}$ denotes the silicon absorption, the only absorption mechanism generating electron-hole pairs. The optical loss is divided into front side reflectance, $R_f$ , escape light, $R_{esc}$, absorption in the rear reflector, $A_{Reflector}$, absorption in the AR-coating, $A_{ARC}$, and absorption by free carriers, $A_{FCA}$**

Silicon is an indirect band-gap semiconductor, meaning that the optical absorption process must be assisted by absorption or emission of a phonon for momentum conservation. This characteristic makes silicon a rather poor optical absorber. While other solar cell materials may show acceptable absorption in a 1 µm thick absorber, silicon requires quite long absorption lengths. This trend is especially clear for photon energies near the band-gap energy of silicon.

In Figure 4.2 (left), the attenuation coefficient and optical penetration depth in silicon is shown. The optical penetration depth is defined as the distance the light has to

travel through silicon in order to be attenuated to 1/e intensity level. The hatched range is a range of penetration depths ranging from 160 µm to 20 µm. 160 µm is around the current industry standard wafer thickness, while 20 µm corresponds to a realistic long-term target thickness. It is seen that wavelengths above approx. 800 nm will have the possibility to penetrate the thinnest of these wafers, the penetration depth easily reaches several millimeters at wavelengths above 1100 nm, meaning that the light can travel much further than the thickness of the wafer before being absorbed. It is at wavelengths showing a penetration length on the order of, or longer than the thickness of the wafer that contributions to $R_{esc}$ are expected. In order to reduce loss contributions from $R_{esc}$, the path length of the light through silicon must be increased. The act of increasing the path length is often called light trapping. Figure 4.2 (right) shows the photogenerated current, $J_{ph}$ generated from band-to-band absorption by sunlight (AM1.5) passing through a given path length in silicon. Optical losses occur even to optical path lengths exceeding 1000 µm.

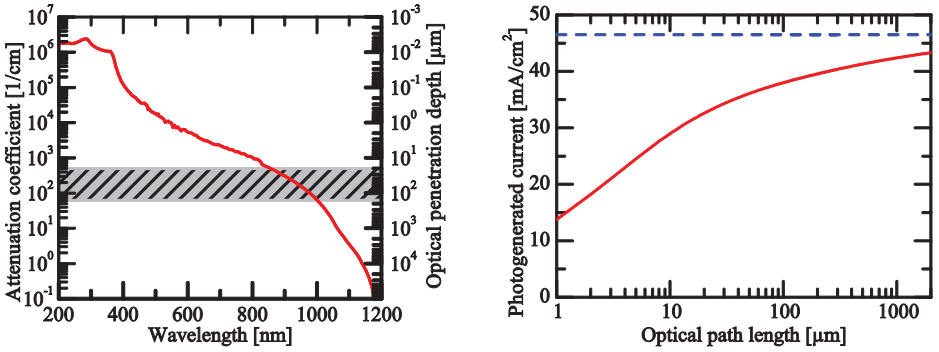


**Figure 4.2: Left: The optical attenuation coefficient and corresponding optical penetration depth in silicon as function of wavelength. Also indicated is a relevant range of wafer thicknesses for solar cell applications. The need for light-trapping for wavelengths above 800 – 1000 nm depending on wafer thickness is obvious. Right: The photogenerated current from sunlight (AM1.5) absorbed by a given path length in silicon (solid line). Also indicated is the maximum current available (dashed line). Data taken from ref.** [74]**.**

Figure 4.3 shows a collection of light-trapping strategies. A shows a planar silicon slab with no rear reflector, where the light gets only one straight pass through the wafer. This must be considered as an absolute worst case scenario. B shows a planar structure with a rear reflector, ensuring two straight passes through the wafer. In a solar cell, the rear metal contact often acts as a mirror (although not a perfect one). C shows a front side textured structure, where the path length in the silicon is increased as a result of the oblique angle taken by the light passing through the wafer. A high probability of escape after two passes is indicated. In silicon, any light hitting the silicon / air interface will be totally

internally reflected if the incidence angle $\theta_i$ is larger than $\theta_i = \sin^{-1}(n_1/n_2)$, which for silicon in air, at wavelengths near the band-gap equals approx. 16.5°, a fairly shallow angle. Angles below 16.5° are referred to as the escape cone, as light within this cone will have a high probability of escaping the silicon wafer.

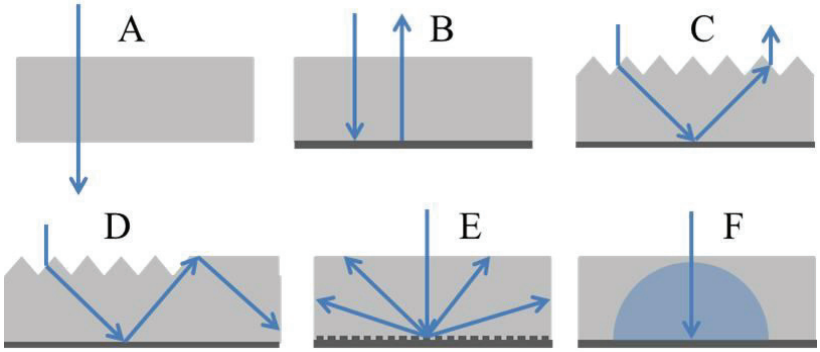


**Figure 4.3: Sketch of various light-trapping schemes. A - no light trapping, B - rear reflector, C – front surface texture, D – symmetry-breaking front side texture, E – diffractive rear reflector, F – Lambertian rear reflector.**

D and E are examples of more advanced light-trapping structures. In D, a textured surface is shown, but unlike C, the symmetry of the texture is broken. Created correctly, such symmetry-breaking structures can cause most of the light to hit the wafer surfaces at angles outside the escape cone, thereby causing total internal reflection to be dominant, and multiple passes are ensured for the majority of the light. E is meant to indicate a diffractive rear reflector, where the incoming light is diffracted into several diffraction orders. The angle of the diffraction orders can be tuned by varying the grating period so that total internal reflection is ensured for all but the specular diffraction order. If, in addition, the specular order is suppressed, the light trapping can be very efficient. F is meant to indicate the case of Lambertian light trapping. Lambertian light trapping is an idealized theoretical light-trapping scheme, where a perfect rear reflector reflects the light homogenously in all directions, independent of the angle of the incoming light. It can be shown that the Lambertian light trapping is the maximum achievable light trapping for a sample uniformly illuminated from all directions. The path length of light in a Lambertian light-trapping scheme can be calculated to $4wn^2$ [75], where $n$ is the refractive index of the material and w is the wafer thickness. In silicon, this path length enhancement $4n^2$ is about a factor 50. While light-trapping is not critical in thick wafers, Figure 4.2,(right) shows that thinner wafers benefit strongly from light-trapping. Increasing the path length

in a wafer from 20 µm by the Lambertian factor to 1000 µm would increase the photogenerated current from around 70 % of the available photocurrent to above 90 %.

The industry standard for mono-crystalline silicon texturing is today the double-sided random pyramid structure. This is created by etching a <100>-oriented silicon wafer in a diluted KOH solution, often adding an alcohol for improved quality of the texture. Such an etch preferentially exposes the <111> crystal planes, leaving a random pattern of upright pyramids. This texture shows a low front surface reflectance, due to the steep angles of the pyramids, and also shows very decent light trapping, as there will be a strong randomization of the direction of the light when refracted or reflected off the various pyramid facets. For multi-crystalline silicon, the random pyramid texture is less efficient, as the direction of the pyramids is dependent of the crystal orientation of the wafer. Therefore, for multi-crystalline wafers or mono-crystalline wafers with e.g. a <111> orientation, isotropic acidic etching is normally applied. This texture will form random dimple-like structures. As the dimples are generally flatter than the pyramids, the chance of experiencing multiple bounces off the front surface is limited, and the front surface reflectance is significantly higher than for the random pyramids. The light-trapping properties, however, are rather good, as is discussed in PAPER IV.

Common for both of these textures, is that they require some form of seeding or attack points in order to form uniformly. Such seed points are readily available today, as most wafers are cut by wire sawing, where the saw damage generates seed points. However, several new wafering technologies are emerging, where no saw damage is present. This poses a challenge for the traditional texturing methods. Furthermore, wafer thickness is expected to decrease, caused by a need to reduce silicon consumption and silicon costs. The traditional texturing methods will remove significant wafer thickness, being less suitable for thin wafers. To overcome these hurdles, new texturing methods must be developed. This thesis presents two ways of creating light management structures on silicon by laser assisted methods.

## 4.2 STATE OF LASER TEXTURING

Already, several approaches to laser texturing of silicon exist. These will be briefly reviewed in this section, and a motivation is given for the approach to laser texturing taken in this thesis.

*Black silicon*

So-called black silicon can be created by irradiation of a silicon surface using ultrashort laser pulses. If a single spot is irradiated by multiple pulses, self-assembling structures tend to emerge, shown in Figure 4.4 (left) [46]. Such structures are often created in a sulfur hexafluoride ($SF_6$) – atmosphere, but they may also be created in air [22]. Black silicon, as the name suggests, displays an extremely low reflectivity over the whole relevant wavelength range, and is as such very close to the ideal anti-reflection coating. On the more practical side, one obstacle seems difficult to bridge. In articles describing black silicon formation, typical parameters may be: Pulse energy density 0.9 J/cm$^2$, repetitions 300 [46]. Using these numbers and multiplying by the size of a 5 inch wafer, a total laser energy of around 44 kJ is required. In current production, 1 wafer/second (or more) is the benchmark for a relevant process. In order to deliver 44 kJ of energy to a wafer in such a short period of time, one would need a 44 kW laser. Not only are such lasers far away from state of the art, but even if one could find such a laser, it would be very interesting to see how a silicon wafer would react to such a violent energy input. With very little material removal, the majority of the laser energy must remain in the silicon wafer. Using the heat capacity and melting enthalpy of silicon, 44 kJ is the energy required to heat and melt a 5 inch wafer with a thickness of around 350 µm. Another issue when working with black silicon in general is the very large surface area that is created. The passivation of such a surface must be of very high quality in order for surface recombination not to be a serious problem. Passivation of black silicon surfaces by the use of atomic-layer deposited $Al_2O_3$ is showing promising results [76].

*Laser Drilling*

A second option for laser texturing is simply to drill a suitable geometric structure, such as the honeycomb structure in mc-silicon shown in Figure 4.4 (middle) [47]. Holes are drilled, and thereafter, the structure is etched in order to remove the laser damaged areas and debris from the process. While this process significantly reduces front surface reflectance for mc-silicon, material removal by laser ablation is an energy intensive process. In this case, 10 J/cm$^2$ and 3 repetitions were applied. Assuming an effective area coverage of 25 % (the 10 J/cm$^2$ would not be applied to the whole surface), the required energy for texturing of a 5 inch wafer is around 1 kJ. While this is much better than what was the case for black silicon, and in a range where industrial lasers do exist, this is still quite a lot of energy to put into a wafer within one second.

*Masked laser processing*

A third option for laser processing is masked laser processing, shown in Figure 4.4 (right) [48]. Here, a $SiN_x$ etch barrier has been applied to the wafer, and the laser is applied only for creating openings through the barrier. A wet-chemical etch (in this case an isotropic etch) is applied for material removal and structure development. By this approach, the laser does virtually no material removal, and much lower laser energy can be applied. Typical pulse energies required for silicon nitride removal is around 0.7 J/cm$^2$. With an area coverage of around 10 % (the image shown has an area coverage of around 5 %), the energy required for opening the etch barrier on a 5 inch wafer is around 10 J, corresponding to a 10 W laser for 1 wafer / second. This is indeed feasible laser power, and easily available today. This masked approach also uses a diffractive optical element (DOE) in order to create several openings through the etch barrier per laser pulse. This relaxes the demand for accurate, high speed scanning and high repetition rate lasers. The requirements on pulse energy rise with the number of spots per pulse, but lasers tend to have pulse energies easily allowing for a high number of simultaneously processed holes.

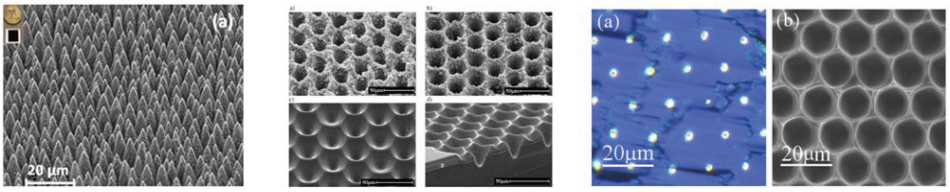


**Figure 4.4: Images of black silicon structure** [46] **(left), laser drilled texture** [47] **(middle) and masked texture with etching** [48] **(right).**

# 4.3 MASKED LASER TEXTURING

Masked laser texturing followed by wet chemical etching seems to be the most promising approach to laser texturing of silicon. Firstly, as the estimations above show, it is the process requiring the absolutely lowest laser power for relevant process speeds. Of course, also the time needed for etching must be taken into account, however, wet chemical etching can be performed as a batch process, significantly reducing processing time per wafer. Secondly, if done properly, the etch process may remove any laser damage, ensuring that the texturing process is free of laser damage. Thirdly, wet-chemical etching is extensively used in solar cell processing, and is as such a well-known process. Therefore, masked texturing followed by wet-chemical etching is the approach chosen in this thesis. Two structures have been created, with strongly differing characteristics. The structures are

discussed in PAPER I-IV, and be referred to as the patch texture and the diffractive structure. SEM micrographs of these textures are shown in Figure 4.5.

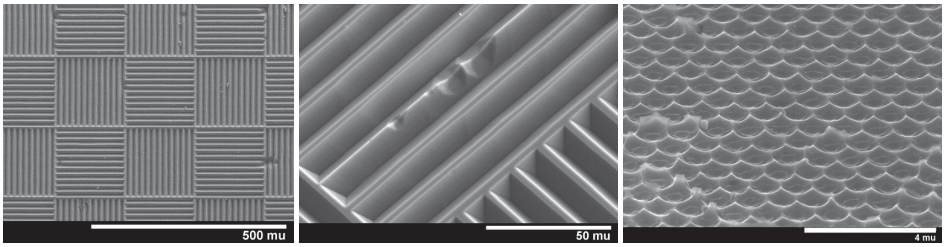


**Figure 4.5: Patch texture (left, center). Diffractive dimple structure (right).**

In order to predict the performance of geometric light-trapping structures, the ray-tracing program TracePro [77] was used. TracePro was used for PAPER II, where the performance of the patch texture was investigated.

Diffractive structures receive their properties from interference effects, and ray-tracing is no longer an adequate method. Predictions on the light-trapping properties of diffractive structures rely on the work by Jo Gjessing. Both the work presented in his Ph.D. thesis [78] and more recent work have been applied.

## *4.3.1 PATCH TEXTURE*

In a series of articles, Campbell *et al.* [79–81] investigated several light-trapping schemes for monocrystalline silicon. One of these schemes has the potential to outperform the random pyramid texture, and at the same time be quite insensitive to the angle of the incoming sunlight, namely the patch texture. This texture would be an interesting alternative to today's industry standards.

The patch texture is schematically shown in Figure 4.6 (left). It consists of patches of trenches oriented alternatingly along orthogonal directions. The size of the patch is adjusted to the thickness of the wafer in such a way that the light which is reflected off the rear reflector hits the neighboring patch (as indicated by the white arrow), where the direction of the trench ensures total internal reflection. In this way, the light is trapped very efficiently. As the angle traveled by the light inside of the silicon wafer is only weakly dependent on the angle of the incident light, the light-trapping properties will be largely preserved also at other angles of incidence. The drawback with the patch texture is of course that it requires some kind of masked etching in order to develop the desired pattern.

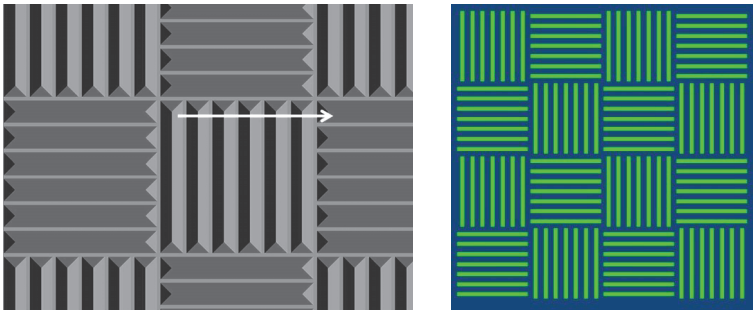

**Figure 4.6: Sketch of the patch texture (left). Indicated by the white arrow is the function of the texture, namely that light hitting a point on one patch will hit the front surface at the corresponding point in the neighboring patch, whereby total internal reflection is ensured. Also shown is the pattern which must be opened through the etch barrier for development of the texture (right).**

The patch texture is scalable, making it possible to start with relatively large structures as a proof-of-concept, developing the process gradually, reducing feature sizes. $SiN_x$ was chosen as the etch barrier, as $SiN_x$ shows high stability in KOH solutions. Patch textures were created opening the etch barrier locally by laser irradiation. An anisotropic KOH etch then developed the pattern. The process and performance of the textures are described in PAPER I and PAPER II.

It was found that the patch texture, under some circumstances, can deliver higher $J_{sc}$ than the random pyramid texture taken as reference. The improvement, however, is fairly modest as a result of the fact that the random pyramid texture is a very good light-trapping structure. It has a low front surface reflectance and decent path-length enhancement. This, combined with the simplicity of the random pyramid texturing process makes it a hard reference to beat. Furthermore, the performance of the patch texture improves when reducing the feature sizes. This, in turn, puts great demands on the performance of the laser system. Single laser pulses were applied, and the pattern was drawn using an xy-table for translation. This is a very slow process, not at all industrially suitable. A galvo scanner would increase scanning speed, but only to a certain degree. A patch pattern with 5 µm wide trenches would require a line somewhat longer than 3 km to be written on a 5 inch wafer, a formidable task even if disregarding accuracy and the fact that it is not simply a straight, continuous line that has to be written. The use of a diffractive optical element (DOE) or other beam-shaping element would have to be applied for industrially relevant implementation of the process. Figure 4.6 (right) shows an image of the laser pattern required for the creation of a patch pattern. If an area on the wafer of 400x400 µm could be processed with one pulse, a laser with 100 kHz repetition rate and a

scan speed of 40 m/s would be required. These are still rather strict requirements for a laser system, but more feasible than the one spot per pulse alternative.

The second challenge related to the small feature sizes is the positioning accuracy and accuracy of the laser intensity. The positioning accuracy ultimately determines the area coverage as discussed in PAPER II, and demands on positioning accuracy rises with decreasing feature size. A further benefit of using a DOE is that the requirement for relative positioning accuracy between spots would also be greatly reduced, as one spot would cover a larger area. Furthermore, small features require tight laser foci. Tight foci have small focal depth, meaning that the distance to the wafer must be very well controlled in order for the laser fluence to remain within process tolerances. The process would be simplified if using an etch barrier that can be deposited without the need for vacuum processing, such as e.g. spin-coating.

### 4.3.2 *DIFFRACTIVE STRUCTURE*

Diffractive structures have feature sizes on the order of the wavelength of light. As a result of interference effects, the light will be scattered into certain angles or diffraction orders. For the simplest case of a one-dimensional grating, light incident on the grating at an angle $\theta_i$ will be diffracted at angles $\theta_m$ described by the grating equation

$$d(\sin\theta_i + \sin\theta_m) = m\lambda\,, \qquad 4.1$$

where $d$ is the grating period, $\lambda$ is the wavelength of the light and $m = 0,1,2,\ldots$ is the diffraction order [82]. Varying $d$, the diffraction angles with a given angle of incidence and wavelength may be tuned. By creating the structure in a suitable manner, e.g. by applying a blazed grating, the specular component ($0^{th}$ order diffraction) may be strongly suppressed. If, in addition, the higher diffraction orders are diffracted outside of the escape cone of silicon, which, as described earlier is approx. 16.5°, one may be able to create highly efficient light-trapping structures. Such structures have been explored theoretically by Jo Gjessing [83–85].

Diffractive structures are generally to be applied where geometric light-trapping textures for some reason are not suitable. For thin wafers, geometric structures may simply be too large, removing too much of the silicon material. Another aspect is the fact that the textures currently being applied require seed points for proper formation. Such seed points are currently in rich supply, originating from the wafer sawing process. For thin wafers, on

the other hand, new production methods are emerging. These kerf-less technologies do not apply sawing, and as such, seeding for etching of the textures may become an issue. Considering these points, the need for suitable light-trapping textures is higher for thin wafers. Unfortunately, diffractive structures are a bit challenging to manufacture, due to the small sizes and periodicity required. Common techniques, besides photolithography, include hot embossing and nanoimprint- or interference lithography [53], [86–88] using reactive ion-etching and plasma-etching. Still, these techniques are not yet implemented in industrial processes, and more attractive alternatives should be investigated.

In this thesis, a technique for creating diffractive structures in silicon is presented. According to the work by Jo Gjessing [78] and Einar Haugan [89], hexagonally ordered dimples was a realistically achievable structure showing good light-trapping potential. An etch barrier was deposited onto a silicon substrate, and self-ordering microspheres were deposited onto the etch barrier. Then, laser pulses were applied to this structure, whereby the laser light was focused by the microspheres, as investigated by Piglmayer *et al.* [90], creating openings through the etch barrier underneath each microsphere. Isotropic wet-etching created hexagonally ordered dimple structures. In this process, the spheres are the focusing elements. This has the benefit that very tight foci are obtainable without the focal depth becoming an issue. Furthermore, by applying a laser spot of 170x170 μm, close to 30 000 holes are created through the etch barrier with each laser pulse. However, spin-coating of each individual wafer does not seem like an industrially viable solution, especially considering the cost of consumables. An alternative could be to use micro-lens arrays as the focusing elements, potentially being re-usable. A process using microspheres on carriers as micro-lens arrays is described by Piglmayer *et al.* [90].

As the diffractive dimple structure is suitable for wafers where traditional surface textures do not yield good results, it has a higher potential for improving solar cell performance than the patch texture, which delivers only modest improvement over existing textures.

# 5 CONCLUSION

This thesis had two main objectives. The first objective was to gain fundamental understanding of the interaction between pulsed lasers and materials relevant for silicon solar cells, with an emphasis on parameter ranges leading to ablation. The understanding of laser-material interaction is important from a fundamental point of view, as it forms the basis for the successful development of laser processes. The second objective was to develop laser-based techniques for manufacturing of efficient light-trapping textures. Emphasis was to be on the investigation of the practically achievable quality of textures already explored theoretically in literature. Light-trapping structures are highly relevant for silicon solar cells, considering the decrease industry standard of wafer thickness and the new emerging wafering technologies.

On the topic of light trapping, two processes were developed for the production of two light-trapping structures, namely the patch texture and the diffractive honeycomb texture. The performance of these textures was investigated by optical absorption and transmission measurements, and compared with reference textures. It was found through simulations that the patch texture gives an increase in $J_{sc}$ of up to 0.5 mA/cm$^2$ compared to the random pyramids texture. The diffractive honeycomb structure delivered a photogenerated current of 38 mA/cm$^2$ on 21 µm thick silicon wafers. The lack of industry standard methods makes comparison somewhat arbitrary, but at a wafer thickness of 100 µm, the diffractive honeycomb structure gives an increase in $J_{ph}$ of 2 and 4 mA/cm$^2$ when compared to isotropically etched and polished samples, respectively. As such, it was clearly shown that laser based texturing may provide highly efficient light-trapping structures suitable for thin substrates, including substrates with a crystal orientation different than the <100> orientation.

On the topic of laser-material interaction, several investigations have been undertaken. The investigations, while focusing on different topics, all revolve around the topic of ablation mechanisms. The four papers on laser-material interaction focus on:

Temperature dependent ablation of silicon, ablation of silicon nitrides, laser damage resulting from ablation and ablation of dielectrics using long wavelength lasers.

In order to understand the interaction between ultrashort pulse lasers and the silicon substrate, a simulation model known as the two-temperature model was implemented. In experiments, it was found that the ablation threshold of silicon is dependent on the temperature of the silicon substrate. At a laser wavelength of 1030 nm, the ablation threshold is reduced from 0.43 J/cm$^2$ at room temperature to 0.24 J/cm$^2$ when the substrate temperature is 320 °C. The simulation model reproduced the experimental trends. Combining results from experiments and simulations, it was found that a high number density of electrons in the silicon substrate causes the ablation, rather than substrate melting and vaporization as would be the case for pulses in the nanosecond range. For practical applications, the use of a slightly elevated substrate temperature can significantly reduce the required laser power, or correspondingly increase the process throughput. The largest reduction in ablation threshold is observed with a laser wavelength of 1030 nm making this wavelength comparably more interesting. As the use of this wavelength eliminates the need for wavelength conversion stages, the complexity of the laser equipment may be reduced.

The differences in interaction between silicon and long (ns) and ultrashort (ps) laser pulses were investigated through the characterization of the depth of the laser induced damage. It was found that the depth of the laser-induced damage is considerably smaller when applying ultrashort laser pulses than when applying long pulses, being reduced from around 3 μm when using long pulses to around 0.25 μm when using ultrashort pulses at a laser wavelength of 532 nm. This is a result of stronger thermal and optical confinement of the laser energy. An estimate on the minority carrier lifetime in the laser irradiated areas is also presented. Knowledge about the depth of laser damage as function of pulse duration and wavelength is a valuable tool when seeking the right laser for a given process.

When investigating the interaction between various silicon nitrides and ultrashort laser pulses, it was found that, using a laser wavelength of 532 nm, the laser energy was deposited either in the silicon or in the dielectric, depending on the laser pulse duration and the composition of the silicon nitride. Low refractive index nitrides or long laser pulses gave indirect ablation, while high refractive index nitrides or short pulses gave direct ablation. The possible absorption mechanisms were investigated, pointing towards significant interaction between the laser pulse and a dense electron-hole plasma in the silicon nitride. As direct and indirect ablation give differing process results, detailed

knowledge on the ablation behavior of silicon nitrides with varying composition as function of laser pulse duration and laser wavelength is valuable for process development.

The use of long wavelength lasers for the ablation of dielectrics from silicon was investigated theoretically and experimentally, as long wavelength lasers may be absorbed directly in the dielectric, without being absorbed in the silicon. Simulations predict that short laser pulses would provide ablation with minimal heating of the silicon. Experiments using a $CO_2$-laser operating at a wavelength of 9.3 μm with a pulse duration of 100 ns, however, shows silicon melting, and hence too strong silicon heating. As such, the concept remains to be proven.

This thesis brings contributions to the understanding of the interaction between laser pulses, in particular ultrashort laser pulses, and silicon and dielectrics. This fundamental knowledge adds to the previous literature on the topic, and may serve as basis both for further fundamental studies and for process development. On the topic of light-trapping, two laser based methods are developed for the production of geometric and diffractive light-trapping structures on silicon. It is shown that high-quality light-trapping textures may be produced by laser based processes.

# 6 DISCUSSION AND OUTLOOK

In this chapter, a discussion of the work in this thesis is given, along with suggestions on the possible continuation of this thesis.

On the topic of light trapping, the high quality of laser-based texturing processes has been demonstrated. The main weakness of this work does not lie in the performance of the textures, but in the complexity of the production processes. In order to achieve the required process speeds, the patch texture requires the use of a diffractive optical element in order to process larger areas with each laser pulse, as discussed in PAPER I.

For the diffractive honeycomb structure, large laser spots can be utilized, and much lower positioning accuracy is required. As such, the laser processing stage is not the critical part of this process. Here the deposition and use of microspheres for the focusing of the laser light is the major obstacle for industrial application. If the microspheres were to be replaced by a re-usable microlens array, the process would be simplified significantly. Both texturing processes would benefit from the implementation of an etch barrier deposition technique that is simpler than the PECVD deposition used within this work. The implementation of the two textures in solar cells would constitute final evidence that the textures have a positive overall influence on a complete solar cell.

On the topic of laser-material interaction, a series of investigations have been undertaken within this thesis, and several interesting and directly applicable findings have been made. The continuation of this work could follow several paths, either towards further fundamental studies and simulations, or towards more application oriented studies. As a direct continuation of the work presented in PAPER VII, short pulse, long wavelength laser ablation should be investigated further. E.g. optical parametric oscillators (OPOs) could be able to produce pulses significantly shorter than the 100 ns tested herein, with a tunable laser wavelength. Such lasers would be a powerful tool for investigation of long wavelength laser ablation, provided that they deliver sufficient pulse energy. Alternatively, or in parallel, improvement of the simulation models would lead to better prediction of the parameter ranges required for ablation of dielectrics without silicon substrate melting. As

simulation results are no more accurate than the physical parameters used in the simulations, it would be beneficial to acquire more detailed knowledge on the temperature dependence of several critical parameters used in the simulations. E.g. thermal properties of the dielectrics and free-carrier absorption coefficients have not been explored at temperatures close to the melting temperature of silicon.

As a continuation of the work on ablation of silicon nitrides, the practical differences between direct and indirect ablation of silicon nitrides should also be investigated further. Both the minority carrier lifetime of the substrate and the specific contact resistance of metallizations applied through the contact openings should be investigated for both direct and indirect ablation

It has been demonstrated within this thesis that several important laser processes yield some degree of laser damage. However, the location of the laser damage also affects to which degree the solar cell performance is affected. As such, it would be interesting to perform a thorough analysis of the influence of the geometry of the laser damage on solar cell performance. A comparison of laser damage in the bulk, emitter, space charge region and directly under contacted areas would be interesting in order to extract the acceptable level of laser damage in each of the cases.

Instead of trying to develop low laser damage processes, it could also be possible to repair laser damage after it has occurred. Thermal annealing [91] and hydrogen plasma annealing [92], [93] of laser induced damage has been characterized by the use of deep-level transient spectroscopy (DLTS), showing the successful removal of laser damage to below the detection limit of the DLTS measurements.

For solar cell applications, the minority carrier lifetime is the relevant measurement quantity, and an investigation of the minority carrier lifetime after such annealing would be interesting. If post-treatment such as annealing is capable of restoring also the minority carrier lifetime in silicon wafers, this could be a very promising tool for enabling low damage laser processes.

# BIBLIOGRAPHY


[1] Erik Kirschbaum, "Germany sets new solar power record, institute says," *Reuters*, 2012. [Online]. Available: http://www.reuters.com/article/2012/05/26/us-climate-germany-solar-idUSBRE84P0FI20120526. [Accessed: 23-Nov-2012].

[2] European Photovoltaic Industry Association, "Annual report 2011," Dec. 2011.

[3] Intergovernmental Panel on Climate Change, "Renewable Energy Sources and Climate Change Mitigation, Special Report of the Intergovernmental Panel on Climate Change," 2012.

[4] U S Energy Information Administration, "Annual Energy Outlook 2012," 2012.

[5] International Renewable Energy Agency, "Renewable energy technologies: Cost analysis series," 2012.

[6] C. Breyer and A. Gerlach, "Global overview on grid-parity event dynamics," in *Proceedings of the 25th European Photovoltaic Solar Energy Conference*, 2010, pp. 5283–5304.

[7] X. Wang, L. Kurdgelashvili, J. Byrne, and A. Barnett, "The value of module efficiency in lowering the levelized cost of energy of photovoltaic systems," *Renewable and Sustainable Energy Reviews*, vol. 15, no. 9, pp. 4248–4254, Dec. 2011.

[8] European Photovoltaic Industry Association, "Global market outlook for photovoltaics until 2016," 2012.

[9] European Photovoltaic Industry Association, "HIGHLIGHT: World's solar photovoltaic capacity passes 100-gigawatt landmark after strong year." [Online]. Available: http://www.epia.org/news/news/#news-45 (February 2013).

[10] J. Nelson, *The Physics of Solar Cells*. Imperial College Press, UK, 2003.

[11] W. Shockley and H. J. Queisser, "Detailed Balance Limit of Efficiency of p-n Junction Solar Cells," *Journal of Applied Physics*, vol. 32, no. 3, pp. 510–519, 1961.

[12] M. J. Kerr, P. Campbell, and A. Cuevas, "Lifetime and efficiency limits of crystalline silicon solar cells," in *Proceedings of the 29th IEEE Photovoltaic Specialists Conference*, 2002, pp. 438 – 441.

[13] J. Zhao, A. Wang, and M. A. Green, "24·5% Efficiency silicon PERT cells on MCZ substrates and 24·7% efficiency PERL cells on FZ substrates," *Progress in Photovoltaics: Research and Applications*, vol. 7, no. 6, pp. 471–474, Nov. 1999.

[14] National Renewable Energy Laboratory (NREL), "Reference Solar Spectral Irradiance: Air Mass 1.5." [Online]. Available: http://rredc.nrel.gov/solar/spectra/am1.5/.

[15] "International Technology Roadmap for Photovoltaics (ITRPV), third edition," 2012.

[16] R. A. Rao, L. Mathew, S. Saha, S. Smith, D. Sarkar, R. Garcia, R. Stout, A. Gurmu, E. Onyegam, D. Ahn, D. Xu, D. Jawarani, J. Fossum, and S. Banerjee, "A novel low cost 25µm thin exfoliated monocrystalline Si solar cell technology," in *Proceedings of the 37th IEEE Photovoltaic Specialists Conference*, 2011, pp. 001504–001507.

[17] M. Ernst and R. Brendel, "Layer transfer of large area macroporous silicon for monocrystalline thin-film solar cells," in *Proceedings of the35th IEEE Photovoltaic Specialists Conference*, 2010, pp. 003122–003124.

[18] F. Henley, S. Kang, Z. Liu, L. Tian, J. Wang, and Y.-L. Chow, "Beam-induced wafering technology for kerf-free thin PV manufacturing," in *Proceedings of the 34th IEEE Photovoltaic Specialists Conference*, 2009, pp. 001718–001723.

[19] P. Rosenits, F. Kopp, and S. Reber, "Epitaxially grown crystalline silicon thin-film solar cells reaching 16.5% efficiency with basic cell process," *Thin Solid Films*, vol. 519, no. 10, pp. 3288–3290, Mar. 2011.

[20] J. Cichoszewski, M. Reuter, and J. H. Werner, "+0.4% Efficiency gain by novel texture for String Ribbon solar cells," *Solar Energy Materials and Solar Cells*, vol. 101, pp. 1–4, Jun. 2012.

[21] P. Engelhart, R. Grischke, S. Eidelloth, R. Meyer, A. Schoonderbeek, U. Stute, A. Ostendorf, and R. Brendel, "Laser Processing for Back-contacted Silicon Solar Cells," in *ICALEO Congress Proceedings*, 2006, pp. 218–226.

[22] J. Bonse, S. Baudach, J. Krüger, W. Kautek, and M. Lenzner, "Femtosecond laser ablation of silicon-modification thresholds and morphology," *Applied Physics A*, vol. 74, no. 1, pp. 19–25, Jan. 2002.

[23] D. Bäuerle, *Laser Processing and Chemistry*, 3rd ed. Berlin Heidelberg: Springer, 2000.

[24] J. M. Liu, "Simple Technique for measurements of pulsed Gaussian-beam spot sizes," *Optics Letters*, vol. 7, no. 5, pp. 196 – 198, 1982.

[25] W. Rasband, "ImageJ." [Online]. Available: http://rsbweb.nih.gov/ij/index.html. [Accessed: 02-Jun-2013].

[26] "Gwyddion Home Page." [Online]. Available: http://gwyddion.net/. [Accessed: 02-Jun-2013].

[27] S. Hermann, T. Dezhdar, N.-P. Harder, R. Brendel, M. Seibt, and S. Stroj, "Impact of surface topography and laser pulse duration for laser ablation of solar cell front side passivating SiNx layers," *Journal of Applied Physics*, vol. 108, no. 11, p. 114514, 2010.

[28] R. T. Young, C. W. White, G. J. Clark, J. Narayan, W. H. Christie, M. Murakami, P. W. King, and S. D. Kramer, "Laser annealing of boron-implanted silicon," *Applied Physics Letters*, vol. 32, no. 3, pp. 139–141, 1978.

[29] A. Bertram and J. R. Köhler, “Improved laser edge isolation process for Si-solar cells,” in *Proceedings of the 26th European Phtovoltaic Solar Energy Conference and Exhibition*, 2011, pp. 2051–2054.

[30] V. Juzumas, J. Janusonis, K. Sulinskas, D. Andrijauskas, V. Cyras, S. Pakalka, A. Isciukiene, and R. Gurklys, “Characterization of laser edge isolation by ultrashort laser pulses,” in *Proceedings of the 26th European Phtovoltaic Solar Energy Conference and Exhibition*, 2011, pp. 1791–1795.

[31] P. Engelhart, S. Hermann, T. Neubert, H. Plagwitz, R. Grischke, R. Meyer, U. Klug, A. Schoonderbeek, U. Stute, and R. Brendel, “Laser Ablation of SiO2 for Locally Contacted Si Solar Cells With Ultra-short Pulses,” *Progress in Photovoltaics: Research and Applications*, vol. 15, pp. 521–527, 2007.

[32] P. Engelhart, N.-P. Harder, T. Horstmann, R. Grischke, R. Meyer, and R. Brendel, “Laser Ablation of Passivating SINx Layers for Locally Contacting Emitters of High-Efficiency Solar Cells,” in *Proceedings of the 4th IEEE World Conference on Photovoltaic Energy*, 2006, pp. 1024–1027.

[33] K. Mangersnes, S. E. Foss, and A. Thøgersen, “Damage free laser ablation of SiO2 for local contact opening on silicon solar cells using an a-Si:H buffer layer,” *Journal of Applied Physics*, vol. 107, p. 043518, 2010.

[34] A. Knorz, M. Peters, A. Grohe, C. Harmel, and R. Preu, “Selective Laser Ablation of SiNx Layers on Textured Surfaces for Low Temperature Front Side Metallizations,” *Progress in Photovoltaics: Research and Applications*, vol. 17, pp. 127–136, 2009.

[35] E. Schneiderlöchner, R. Preu, R. Lüdemann, and S. W. Glunz, “Laser-fired rear contacts for crystalline silicon solar cells,” *Progress in Photovoltaics: Research and Applications*, vol. 10, no. 1, pp. 29–34, Jan. 2002.

[36] U. Zastrow, L. Houben, D. Meertens, A. Grohe, T. Brammer, and E. Schneiderlöchner, “Characterization of laser-fired contacts in PERC solar cells: SIMS and TEM analysis applying advanced preparation techniques,” *Applied Surface Science*, vol. 252, no. 19, pp. 7082–7085, Jul. 2006.

[37] “M-Solv - Laser fired contacts.” [Online]. Available: http://www.m-solv.com/laser-fired-contacts. [Accessed: 02-Jun-2013].

[38] T. C. Röder, E. Hoffmann, J. R. Köhler, and J. H. Werner, “30 µm wide contacts on silicon cells by laser transfer,” in *Proceedings of the 35th IEEE Photovoltaic Specialists Conference*, 2010, pp. 3597–3599.

[39] T. F. Deutsch, J. C. C. Fan, G. W. Turner, R. L. Chapman, D. J. Ehrlich, and R. M. Osgood, “Efficient Si solar cells by laser photochemical doping,” *Applied Physics Letters*, vol. 38, no. 3, pp. 144–146, 1981.

[40] T. F. Deutsch, D. J. Ehrlich, D. D. Rathman, D. J. Silversmith, and R. M. Osgood, “Electrical properties of laser chemically doped silicon,” *Applied Physics Letters*, vol. 39, no. 10, pp. 825–827, 1981.

[41] A. Esturo-Breton, M. Ametowobla, J. R. Köhler, and J. H. Werner, "Laser Doping for Crystalline Silicon Solar Cell Emitters," in *Proceedings of the 20th European Photovoltaic Solar Energy Conference*, 2005, no. June, pp. 851–854.

[42] P. Oesterlin and U. Jäger, "High Throughput Laser Doping for Selective Emitter Crystalline Si Solar Cells," in *Proceedings of the 18th IEEE Conference on Advanced Thermal Processing of Semiconductors - RTP 2010*, 2010, pp. 146–153.

[43] D. Kray, M. Aleman, A. Fell, S. Hopman, K. Mayer, M. Mesec, R. Müller, G. P. Willeke, S. W. Glunz, B. Bitnar, D.-H. Neuhaus, R. Lüdemann, T. Schlenker, D. Manz, A. Bentzen, E. Sauar, A. Pauchard, and B. Richerzhagen, "Laser-doped silicon solar cells by Laser Chemical Processing (LCP) exceeding 20% efficiency," in *Proceedings of the 33rd IEEE Photovolatic Specialists Conference*, 2008, pp. 1–3.

[44] R. Ferré, R. Gogolin, J. Müller, N.-P. Harder, and R. Brendel, "Laser transfer doping for contacting n-type crystalline Si solar cells," *Physica Status Solidi (a)*, vol. 208, no. 8, pp. 1964–1966, Aug. 2011.

[45] "Manz AG - Laser processing technology." [Online]. Available: http://www.manz.com/products-services/crystalline-solar-cells/laser-processing-technology. [Accessed: 02-Jun-2013].

[46] B. K. Nayak, V. V. Iyengar, and M. C. Gupta, "Efficient light trapping in silicon solar cells by ultrafast-laser-induced self-assembled micro / nano structures," *Progress in Photovoltaics: Research and Applications*, vol. 19, pp. 631–639, 2011.

[47] M. Abbott and J. Cotter, "Optical and Electrical Properties of Laser Texturing for High-efficiency Solar Cells," *Progress in Photovoltaics: Research and Applications*, vol. 14, pp. 225–235, 2006.

[48] H. Morikawa, D. Niinobe, K. Nishimura, S. Matsuno, and S. Arimoto, "Processes for over 18.5% high-efficiency multi-crystalline silicon solar cell," *Current Applied Physics*, vol. 10, no. 2, pp. S210–S214, Mar. 2010.

[49] J. Arumughan, T. Pernau, A. Hauser, and I. Melnyk, "Simplified edge isolation of buried contact solar cells," *Solar Energy Materials and Solar Cells*, vol. 87, no. 1–4, pp. 705–714, May 2005.

[50] F. Book, S. Braun, A. Herguth, A. Dastgheib-Shirazi, B. Raabe, and G. Hahn, "The etchback selective emitter technology and its application to multicrystalline silicon," in *Proceedings of the 35th IEEE Photovoltaic Specialists Conference*, 2010, pp. 001309–001314.

[51] A. Uzum, A. Hamdi, S. Nagashima, S. Suzuki, H. Suzuki, S. Yoshiba, M. Dhamrin, K. Kamisako, H. Sato, K. Katsuma, and K. Kato, "Selective emitter formation process using single screen-printed phosphorus diffusion source," *Solar Energy Materials and Solar Cells*, vol. 109, pp. 288–293, Feb. 2013.

[52] C. Kick, B. Thaidigsmann, M. Linse, F. Clement, A. Wolf, and D. Biro, "Printed fire-through contacts (FTC) - an alternative approach for local rear contacting of passivated solar cells," in *Proceedings of the 27th European Phtovoltaic Solar Energy Conference and Exhibition*, 2012, pp. 544 – 546.

[53] H. Hauser, B. Michl, V. Kübler, S. Schwarzkopf, C. Müller, M. Hermle, and B. Bläsi, "Nanoimprint Lithography for Honeycomb Texturing of Multicrystalline Silicon," in *Energy Procedia*, 2011, vol. 8, pp. 648–653.

[54] O. Schultz, G. Emanuel, S. W. Glunz, and G. P. Willeke, "Texturing of multicrystalline silicon with acidic wet chemical etching and plasma etching," in *Proceedings of the 3rd World Conference on Photovoltaic Energy Conversion*, 2003, pp. 1360–1363.

[55] K. Mangersnes and S. E. Foss, "A thermodynamic model for the laser fluence ablation threshold of PECVD SiO2 on thin a-Si:H films deposited on crystalline silicon," in *Proceedings of the Materials Research Society*, 2010, vol. 1245, pp. 1245–A16–02.

[56] The MathWorks Inc, "Math works documentation center, pdepe." [Online]. Available: http://www.mathworks.se/help/matlab/ref/pdepe.html. [Accessed: 02-Jun-2013].

[57] The MathWorks Inc, "Matlab - The Language of Technical Computing." [Online]. Available: http://www.mathworks.se/products/matlab/. [Accessed: 02-Jun-2013].

[58] K. Mangersnes, "Back-contacted back-junction silicon solar cells," University of Oslo, 2010.

[59] H. S. Sim, S. H. Lee, and K. G. Kang, "Femtosecond pulse laser interactions with thin silicon films and crater formation considering optical phonons and wave interference," *Microsystem Technologies*, vol. 14, no. 9–11, pp. 1439–1446, Jan. 2008.

[60] H. M. van Driel, "Kinetics of high-density plasmas generated in Si by 1,06- and 0,53-μm picosecond laser pulses.pdf," *Physical review. B, Condensed matter*, vol. 35, no. 15, pp. 8166 – 8176, 1987.

[61] N. Bulgakova, R. Stoian, A. Rosenfeld, I. Hertel, and E. Campbell, "Electronic transport and consequences for material removal in ultrafast pulsed laser ablation of materials," *Physical Review B*, vol. 69, no. 5, p. 054102, Feb. 2004.

[62] K. Sokolowski-Tinten, J. Bialkowski, and D. von der Linde, "Ultrafast laser-induced order-disorder transitions in semiconductors," *Physical Review B*, vol. 51, no. 20, pp. 14186–14198, 1995.

[63] A. Cavalleri, K. Sokolowski-Tinten, J. Bialkowski, M. Schreiner, and D. von der Linde, "Femtosecond melting and ablation of semiconductors studied with time of flight mass spectroscopy," *Journal of Applied Physics*, vol. 85, no. 6, pp. 3301–3309, 1999.

[64] L. A. Falkovsky and E. G. Mishchenko, "Electron-lattice kinetics of metals heated by ultrashort laser pulses," *Journal of Experimental and Theoretical Physics*, vol. 88, no. 1, pp. 84–88, Jan. 1999.

[65] N. Bulgakova, R. Stoian, A. Rosenfeld, I. Hertel, and E. Campbell, "Fast electronic transport and coulomb explosion in materials irradiated with ultrashort laser pulses," in *Laser ablation and its applications*, 1st ed., C. Phipps, Ed. Boston, MA: Springer Science+Business Media LLC, 2010, pp. 17–36.

[66] N. Ashcroft and N. Mermin, *Solid state physics*, 1st ed. Thomson Learning, inc, 1976.

[67] J. Reitz, F. Milford, and R. Christy, *Foundations of electromagnetic theory*, 4th ed. Addison-Wesley Publishing Company, 1993.

[68] N. D. Arora, J. R. Hauser, and D. J. Roulston, "Electron and Hole Mobilities in Silicon as a Function of Concentration and Temperature," *IEEE Transactions on Electron Devices*, vol. ED-29, no. 2, pp. 292–295, 1982.

[69] S. W. Hsieh, C. Y. Chang, Y. S. Lee, C. W. Lin, and S. C. Hsu, "Properties of plasma-enhanced chemical-vapour-deposited a-SiNx:H by various dilution gases," *Journal of Applied Physics*, vol. 76, no. 6, pp. 3645–3655, 1994.

[70] J. R. Davis, A. Rohatgi, R. H. Hopkins, P. D. Blais, P. Rai-Choudhury, J. R. McCormick, and H. C. Mollenkopf, "Impurities in silicon solar cells," *IEEE Transactions on Electron Devices*, vol. ED-27, no. 4, pp. 677–687, Apr. 1980.

[71] A. B. Sproul, "Dimensionless solution of the equation describing the effect of surface recombination on carrier decay in semiconductors," *Journal of Applied Physics*, vol. 76, no. 5, pp. 2851–2854, 1994.

[72] M. Ametowobla, "Characterization of a Laser Doping Process for Crystalline Silicon Solar Cells," Universität Stuttgart, 2010.

[73] O. S. Heavens, *Optical properties of thin solid films*. New York: Dover Publications, Inc., 1991.

[74] E. D. Palik, *Handbook of Optical Constants of Solids*. Elsevier, 1998.

[75] E. Yablonovitch and G. D. Cody, "Intensity enhancement in textured optical sheets for solar cells," *IEEE Transactions on Electron Devices*, vol. ED-29, no. 2, pp. 300–305, Feb. 1982.

[76] P. Repo, A. Haarahiltunen, L. Sainiemi, M. Yli-Koski, H. Talvitie, M. C. Schubert, and H. Savin, "Effective Passivation of Black Silicon Surfaces by Atomic Layer Deposition," *IEEE Journal of Photovoltaics*, vol. 3, no. 1, pp. 90–94, Jan. 2013.

[77] "TracePro." p. http://www.lambdares.com/software_products/tracepro/, [Accessed: 02-Jun-2013].

[78] J. Gjessing, "Photonic crystals for light trapping in solar cells," University of Oslo, 2011.

[79] P. Campbell and M. A. Green, "Light Trapping Properties of Pyramidally Textured Surfaces," *Journal of Applied Physics*, vol. 62, no. 1, pp. 243–249, 1987.

[80] P. Campbell, S. R. Wenham, and M. A. Green, "Light trapping and reflection control with tilted pyramids and grooves," in *Conference Proceedings of the 20th IEEE Photovoltaic Specialists Conference*, 1988, pp. 713–716.

[81] P. Campbell and M. A. Green, "High performance light trapping textures for monocrystalline silicon solar cells," *Solar Energy Materials and Solar Cells*, vol. 65, no. 1–4, pp. 369–375, Jan. 2001.

[82] E. Hecht, *Optics*, 4th ed. San Francisco, CA: Addison Wesley, 2002.

[83] J. Gjessing, E. S. Marstein, and A. Sudbø, "2D back-side diffraction grating for improved light trapping in thin silicon solar cells," *Optics express*, vol. 18, no. 6, pp. 5481–5495, Mar. 2010.

[84] J. Gjessing, A. S. Sudbø, and E. S. Marstein, "Comparison of periodic light-trapping structures in thin crystalline silicon solar cells," *Journal of Applied Physics*, vol. 110, no. 3, p. 033104, Aug. 2011.

[85] J. Gjessing, A. S. Sudbø, and E. S. Marstein, "A novel back-side light-trapping structure for thin silicon solar cells," *Journal of the European Optical Society: Rapid Publications*, vol. 6, p. 11020, 2011.

[86] S. H. Zaidi, J. M. Gee, and D. S. Ruby, "Diffraction grating structures in solar cells," in *Proceedings of the 28th IEEE Photovoltaic Specialists Conference*, 2000, pp. 395–398.

[87] H. Hauser, A. Mellor, A. Guttowski, C. Wellens, J. Benick, C. Müller, M. Hermle, and B. Bläsi, "Diffractive Backside Structures via Nanoimprint Lithography," *Energy Procedia*, vol. 27, no. 2011, pp. 337–342, 2012.

[88] B. Bläsi, H. Hauser, O. Höhn, V. Kübler, M. Peters, and A. Wolf, "Photon Management Structures Originated by Interference Lithography," *Energy Procedia*, vol. 8, pp. 712–718, Jan. 2011.

[89] E. Haugan, H. Granlund, J. Gjessing, and E. S. Marstein, "Colloidal crystals as templates for light harvesting structures in solar cells," *Energy Procedia*, vol. 10, pp. 292–296, 2011.

[90] K. Piglmayer, R. Denk, and D. Bäuerle, "Laser-induced surface patterning by means of microspheres," *Applied Physics Letters*, vol. 80, no. 25, pp. 4693–4695, 2002.

[91] A. Barhdadi and J. C. Muller, "Electrically Active Defects in Silicon after various Optical Thermal Processing," *Rev. Energ. Ren.*, vol. 3, pp. 29–38, 2000.

[92] E. M. Lawson and S. J. Pearton, "Hydrogen passivation of laser-induced acceptor defects in p-type silicon," *Physica Status Solidi (a)*, vol. 72, pp. 55–58, 1982.

[93] J. L. Benton, C. J. Doherty, S. D. Ferris, D. L. Flamm, L. C. Kimerling, and H. J. Leamy, "Hydrogen passivation of point defects in silicon," *Applied Physics Letters*, vol. 36, no. 8, p. 670, 1980.

# A. ANALYTICAL EXPRESSION FOR RECOMBINATION BY LASER DAMAGED REGION

For the analysis presented in section 3.4.1, "Characterization of laser-induced damage in silicon" some analytical expressions may come in handy. In this appendix, an expression for the influence from a laser damaged area on a wafer is derived. Figure A.1 shows the assumed geometry. A wafer with thickness $d + w$ has a bulk lifetime $\tau_{bulk}$, and surface recombination velocities $S_1$ and $S_2$. A laser damaged region is located near surface 2, and has a width $w$ and a degraded lifetime $\tau_{laser}$, where $\tau_{laser}$ is assumed to be constant throughout the damaged region. We wish to investigate the influence of the parameters $w$ and $\tau_{laser}$ on effective lifetime in this structure. In order to do so, we seek to quantify the recombination taking place in the laser damaged region. The local recombination is quantified as

$$U = \frac{n}{\tau} \qquad \text{A.1}$$

where $U$ is the recombination rate per unit volume, $n$ is the local number density of excess carriers and $\tau$ is the lifetime of these carriers. Integrating over the recombining region $x \in [d, d + w]$, we obtain the recombination rate per unit area,

$$U_s = \int_d^{d+w} \frac{n}{\tau} dx \qquad \text{A.2}$$

where $U_s$ is the total recombination per unit area from the laser damaged region. As the laser damage is a surface-near defect, we wish to express the recombination taking place in the laser damaged region as a surface recombination rate. Inserting a virtual surface at the boundary between bulk and damaged region, we use the definition of surface recombination velocity:

$$U_s \equiv S_{laser} * n_s \quad \text{A.3}$$

where $n_s$ is the number density of electrons at the boundary ($x = d$), and $S_{laser}$ is the effective laser surface recombination velocity. In order to solve these expressions, we need to find the electron distribution, $n(x)$.

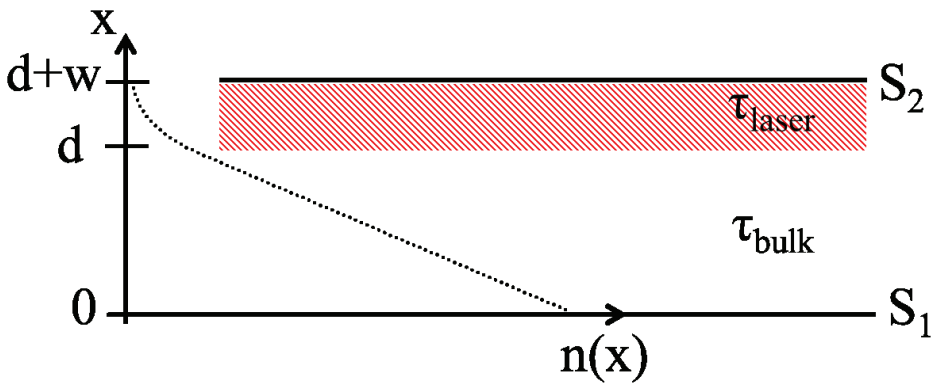


**Figure A.1: Assumed geometry of a laser damaged wafer. Indicated are the surfaces with surface recombination velocities, $S_1$ and $S_2$, being located at $x = 0$ and $x = d + w$. A laser damaged region extending from $x = d$ to $x = d + w$ is shown in hatched red. Also indicated as a dotted line is the shape of the electron distribution resulting from such a geometry (with $S_2 = S_1 = 0$ and $\tau_{bulk} = \infty$), being linear in the bulk, and exponentially decaying in the laser damaged region.**

# A.1 ELECTRON DISTRIBUTION

As a first approximation, we assume that $S_1 = S_2 = 0$, while $\tau_{bulk} = \infty$, meaning that the only recombination takes place in the laser damaged region. We also assume that the photogeneration is taking place close to surface 1 ($x = 0$). We use the continuity equation:

$$\frac{\partial n}{\partial t} = G - U - \frac{\partial J}{\partial x} \quad \text{A.4}$$

where $n$ is the number density of electrons, $t$ is time, $x$ is the distance through the wafer, $G$ is the bulk generation rate, $U$ is the bulk recombination rate and $J$ is the electron current. As we seek a stationary solution, we require the time derivative to be zero. With only surface photogeneration, $G = 0$. We relate recombination to lifetime

$$U = \frac{n}{\tau} = -\frac{\partial J}{\partial x} \quad \text{A.5}$$

and consider only diffusion current (in electrons /cm$^2$ s)

$$J = -D\frac{\partial n}{\partial x}. \quad \text{A.6}$$

Here, $D$ is the electronic diffusivity. For a stationary solution with no photogeneration in the bulk, we then have

$$\frac{n}{\tau} = D\frac{\partial^2 n}{\partial x^2}. \quad \text{A.7}$$

The boundary conditions are:

$$J(x = 0) = G_s, \quad \text{A.8}$$

where $G_s$ is the surface photogeneration rate, and

$$J(x = d + w) = 0 \quad \text{A.9}$$

as there is no surface recombination at surface $S_2$. Furthermore, there is continuity in number density of carriers and in current at the boundary between bulk and laser damaged area:

$$n_1(x = d) = n_2(x = d) \quad \text{A.10}$$

$$\frac{\partial n_1}{\partial x}(x = d) = \frac{\partial n_2}{\partial x}(x = d) \quad \text{A.11}$$

This yields solutions of the form:

$$n_1(x) = A_1 x + B_1 \quad \text{A.12}$$

$$n_2(x) = A_2 e^{x/\sqrt{D\tau}} + B_2 e^{-x/\sqrt{D\tau}} \quad \text{A.13}$$

Applying boundary conditions yields

$$n_1(x) = -\frac{G_s}{D}(x - d) + B_{1'} \quad \text{A.14}$$

$$n_2(x) = A_2 2e^{d+w}\cosh\left(\frac{x-(d+w)}{\sqrt{D\tau}}\right) \quad \text{A.15}$$

where

$$B_{1'} = G_s\sqrt{\frac{\tau}{D}}\tanh\left(\frac{w}{\sqrt{D\tau}}\right) \quad \text{A.16}$$

and

$$A_2 = -\frac{G_s}{2e^{d+w}\sinh\left(\frac{w}{\sqrt{D\tau}}\right)}\sqrt{\frac{\tau}{D}}\ . \qquad \text{A.17}$$

The electron distribution following from equations A.14 – A.17 is shown in Figure A.1.

## A.2 SURFACE RECOMBINATION VELOCITY

Now that we have obtained expressions for the electron distribution in the laser damaged region and the undamaged bulk, we can solve equation A.2. using the electron density obtained in equation A.15.

$$U_s = \frac{A_2 2e^{d+w}}{\tau}\int_d^{d+w}\cosh\left(\frac{x-(d+w)}{\sqrt{D\tau}}\right)dx$$

$$= \frac{2e^{d+w}G_s\sqrt{D\tau}}{\tau 2e^{d+w}\,sinh\left(\frac{w}{\sqrt{D\tau}}\right)}\sqrt{\frac{\tau}{D}}\left[sinh\left(\frac{w}{\sqrt{D\tau}}\right)\right] = G_s \qquad \text{A.18}$$

To no surprise. The laser damaged region is the only recombination source, and must balance out the photogeneration. Solving equation A.3 for $S_{laser}$ by using the findings in equations A.14 and A.16 gives

$$S_{laser} \equiv \frac{U_s}{n_s} = \frac{U_s}{n(x=d)} = \frac{G_s}{B_{1'}}$$

$$= \frac{G_s\,tanh\left(\frac{w}{\sqrt{D\tau}}\right)}{G_s\sqrt{\frac{\tau}{D}}} = \sqrt{\frac{D}{\tau}}\ tanh\left(\frac{w}{\sqrt{D\tau}}\right). \qquad \text{A.19}$$

If $\sqrt{D\tau} \ll w$, i.e. if the laser damaged region is much wider than the electron diffusion length, this goes to $\sqrt{D/\tau}$. (holds to within 4% if $w/\sqrt{D\tau} > 2$). The width of the laser damaged region does not make any difference anymore. The recombination is diffusion limited. In the other extreme, with a very narrow laser damaged region, S goes to zero.

The expression for $S_{laser}$ can also be obtained without any assumptions on the bulk of the wafer, simply using equation A.13 for $n_2$.

## A.3 EFFECTIVE LIFETIME

Using the expression by Sproul [71] for the surface lifetime,

$$\frac{1}{\tau_s} = \alpha_0^2 D \qquad \text{A.20}$$

where $\alpha$ is the smallest eigenvalue solution of the equation

$$tan(\alpha_0 w) = (S_{laser} + S_2)/(\alpha_0 D - \frac{S_{laser} S_2}{\alpha_0 D}) \quad \text{A.21}$$

and using that the effective lifetime is given as

$$\frac{1}{\tau_{eff}} = \frac{1}{\tau_b} + \frac{1}{\tau_s} \quad \text{A.22}$$

we can calculate the effective lifetime as function of the width and lifetime of the laser damaged area. Assuming a bulk lifetime of $\tau_{bulk} = 1800\ \mu s$ and a thickness of the wafer of 300 µm, we obtain the result shown graphically in Figure A.2. With high lifetime in the laser damaged region or a very shallow laser damaged region, the effective lifetime is limited by the bulk lifetime, while for very low lifetime in the laser damaged region or very thick laser damaged region, the effective lifetime is that of diffusion limited recombination at one surface.

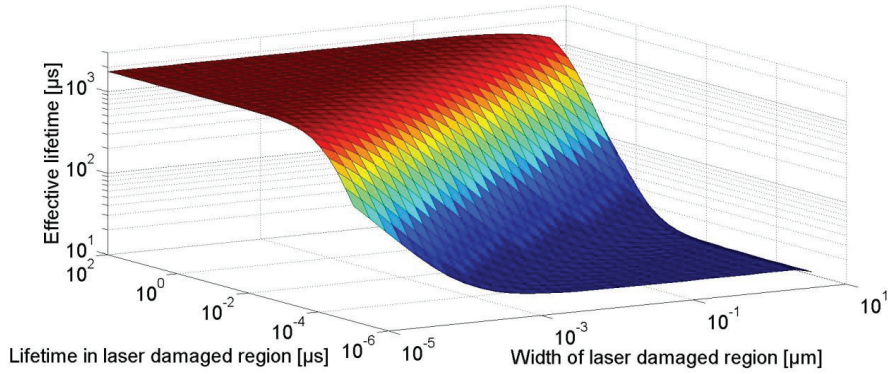


**Figure A.2: Effective lifetime as function of the lifetime in the laser damage region and the width of the laser damaged region.**

# LIST OF ABBREVIATIONS

| Abbreviation | Meaning |
|---|---|
| AM1.5 | Air Mass 1.5. Standard solar spectrum for solar cell efficiency measurements |
| ARC | Anti-reflection coating |
| AFM | Atomic Force Microscopy |
| DLTS | Deep-level transient spectroscopy |
| DOE | Diffractive Optical Element |
| FTIR | Fourier-Transform Infrared Spectroscopy |
| FCA | Free-carrier absorption |
| FWHM | Full Width Half Maximum |
| IR | Infra-red |
| IFE | Institute for Energy Technology |
| LCP | Laser Chemical Processing |
| LFC | Laser fired contacts |
| LIPSS | Laser Induced Periodic Surface Structures |
| HNA | Mix containing Hydrofluoric acid, Nitric Acid, Acetic Acid |
| MFD | Mode Field Diameter |
| OPO | Optical parametric oscillator |
| PL | Photoluminescence imaging |
| PV | Photovoltaic energy |
| PECVD | Plasma-Enhanced Chemical Vapor Deposition |
| QSSPC | Quasi-steady state photoconductance decay |
| RIE | Reactive Ion Etching |
| SEM | Scanning Electron Microscopy |
| SHG | Second Harmonic Generation |
| SRV | Surface recombination Velocity |
| THG | Third Harmonic Generation |
| TEM | Transmission Electron Microscopy |
| UV | Ultra-violet |

# PAPER I

J. Thorstensen and S. E. Foss, "Laser assisted texturing for thin and highly efficient monocrystalline silicon solar cells," *in Proceedings of the 26th European Photovoltaic Energy Conference,* pp. 1628 – 1631, 2011.

# PAPER II

J. Thorstensen, S. E. Foss, and J. Gjessing, "Light-trapping properties of patch textures created using Laser Assisted Texturing," *Progress in Photovoltaics: Research and Applications,* available online, DOI: 10.1002/pip.2335, 2013.

# PAPER III

J. Thorstensen, J. Gjessing, E. Haugan, and S. E. Foss, "2D periodic gratings by laser processing," *Energy Procedia,* vol. 27, pp. 343–348, 2012.

Available online at www.sciencedirect.com

SciVerse ScienceDirect

Energy Procedia 27 (2012) 343 – 348

Energy Procedia

SiliconPV 2012, 03-05 April 2012, Leuven, Belgium

# 2D periodic gratings by laser processing

J. Thorstensen[a], J. Gjessing, E. Haugan, S.E. Foss

*Institute for Energy Technology, Pb. 40, 2027 Kjeller, Norway*

**Abstract**

As the thickness of crystalline silicon wafers for use in solar cells is reduced, transmission-related losses become increasingly important. Very thin silicon solar cells will benefit from surface structures exhibiting efficient light trapping, such as 2D periodic structures with diffractive properties. Furthermore, multicrystalline silicon solar cells will benefit from a front surface texture which exhibits lower reflectance than the standard iso-etch. In this paper, we investigate three new methods for creating such structures based on the formation of a 2D periodic template from a colloidal suspension of microspheres and subsequent laser processing and etching.

Polystyrene spheres with 1 μm diameter are spin-coated onto a silicon wafer, and forms a hexagonal pattern through self-ordering. The wafer is irradiated with an ultrashort-pulse laser with sufficient power to form pits in the wafer surface below the individual polystyrene spheres, thus transferring the hexagonal pattern to the silicon wafer. The maximum obtained diameter and depth of the pits are 600 nm and 100 nm respectively.

To increase the depth of the pits we deposit the self-ordering microspheres on a silicon nitride etch barrier, followed by laser irradiation for local opening of the barrier and an isotropic etch through these holes. With this approach we are able to create structures with a base diameter of 800 nm and a depth of 350 nm. These structures are found in simulations to have good light-trapping properties and the method may therefore be suitable for the fabrication of 2D photonic crystals for light-trapping in silicon solar cells.



*Keywords*: Light trapping; photonic crystals; etching; laser processing

## 1. Introduction

Light management in very thin silicon solar cells (<50 μm) is an important topic for several reasons. Firstly, these cells will be so thin that efficient absorption of long wavelength light will be difficult, due to

[a] Corresponding author. Tel.: +47 63806445 fax: +47 63812905
*E-mail address*: Jostein.thorstensen@ife.no

1876-6102 © 2012 Published by Elsevier Ltd.Selection and/or peer review under responsibility of the Centro de Micro Análisis de Materiales, Universidad Autónoma de Madrid.
doi:10.1016/j.egypro.2012.07.074

the long absorption length at these wavelengths. To further complicate matters, the traditional approach of wet chemical etching may be unsuitable due to the relatively large structures created by these methods, and the large amount of wafer material removed in the texturing process. Furthermore, some methods for creating thin silicon wafers will produce <111> oriented wafers [1], which are not suitable for anisotropic KOH texturing at all.

Diffractive structures for light trapping in thin silicon solar cells has received a lot of attention, due to their potential to increase the light absorption in thin solar cells. Various structures have been shown theoretically in simulations to provide good light trapping, but the production of cost effective large scale diffractive structures remains a challenge for commercial realization. Fabrication methods that have been suggested include nano-imprint lithography or hot embossing [2] and interference lithography [3]. Also, methods using self-ordered spheres have been reported [4]. Gjessing et al. [5,6] has theoretically investigated the light trapping potential of cylinders, cones, inverted pyramids and dimples in a square pattern, all of which show good light trapping potential with lattice periods in the range of 0.7 – 1 μm and a fill factor from 0.6 to max fill factor (pi/4 for non-overlapping circular structures). The optimum depth of the features is reported to be in the range of 200 - 500 nm. Structures in a triangular / hexagonal pattern were also reported to achieve similar performance as the square patterns.

In this work, we seek to produce a diffractive dimple structure similar to that reported in [5], based on a honeycomb / hexagonal pattern of pits. Our production method is based on the deposition of self-ordering colloidal spheres on a silicon wafer. These spheres will, under correct deposition-parameters, preferentially grow hexagonal / honeycomb 2D-crystals, and they will act as microlenses when irradiated by a laser [7]. Previous work has shown the potential for creating surface structures using such microlenses [8].

We propose three different processes for creating the desired structures, summarized in Table 1. In the simplest form of the process, the spheres are deposited directly on the silicon wafer, followed by laser irradiation. Here, the laser irradiation itself should remove a substantial material volume, and create structures suitable for light trapping. This would be the process requiring the least number of processing steps. Another possibility is to deposit the spheres on an etch barrier, e.g. a silicon nitride ($SiN_x$) layer, let the laser create small openings in the $SiN_x$, and perform an isotropic etch through these openings. In this process, the etching, rather than the laser irradiation ensures material removal and the creation of the pattern. The third process which we investigate is a process where we cover a Si wafer with spheres and subsequently deposit PECVD $SiN_x$ on top of this structure. Thereafter, the spheres are removed by sonication. This process will leave openings in the $SiN_x$ etch barrier where the spheres have been in direct contact with the silicon wafer.

Table 1: Summary of the process steps involved in the three processes for creating 2D periodic structures

| Process 1 | Process 2 | Process 3 |
|---|---|---|
| Microsphere deposition | $SiN_x$ deposition | Microsphere deposition |
| Laser irradiation | Microsphere deposition | $SiN_x$ deposition |
| | Laser irradiation | Microsphere removal |
| | Etching | Etching |

## 2. Experimental

The method for depositing self-organizing colloidal spheres follows the work in [9]. A 30 % (vol) solution of 1 μm polystyrene (PS) or 800 nm silica beads was applied to a hydrophilic polished silicon wafer surface, or a silicon wafer covered in a 150 nm thick PECVD-deposited $SiN_x$-layer. Self-assembly was achieved by spin-coating the sample at 4000 – 7000 RPM. The result was a mono-layer of poly-crystalline hexagonally ordered beads covering most of the wafer.

Irradiation of the samples was performed using an ultrashort-pulse laser with 3 ps pulse duration and a wavelength of 515 nm. The beam had a Gaussian spatial distribution. Single (non-overlapping) pulses were employed. For experiments with the $SiN_x$ etch barrier, isotropic etching through the openings in the barrier was performed using a hydrofluoric acid, nitric acid, acetic acid (HNA) solution. The HF concentration was varied from $1HF:40HNO_3:15CH_3COOH$ (HNA 1:40:15) to $5HF:40HNO_3:15CH_3COOH$ (HNA 5:40:15), whereby the etch rate in this range at 21 °C increased with HF content from around 300 nm/min to around 2500 nm/min.

For characterization of the processing results, Scanning Electron Microscopy (SEM) and Atomic Force Microscopy (AFM) were used.

## 3. Results

### *3.1. Process 1: Microspheres on silicon wafer*

In this process the microspheres were deposited directly on silicon wafers and irradiated by laser. In the irradiation process, the microspheres are blown off the wafer along with the silicon ablated from the wafer. Any remaining microspheres were rinsed off in DI water before further characterization. SEM images revealed a hexagonal pattern of pits, corresponding to the pattern of the microspheres. The size of the pits varied with the distance from the center of the Gaussian beam as illustrated in Fig. 1a. In the center of the spot, it is clearly seen that the substrate has melted completely, destroying the hexagonal pattern, while far from the center of the spot, the pits created are rather small. In fact, at the edges of the Gaussian distribution, we routinely obtain structures with sizes below 250 nm, which is far smaller than the wavelength of the applied light, and a nice proof of the resolution obtainable using microspheres for the focusing of the light.

Fig. 1b shows a close-up of an area with a laser intensity giving relatively large pits. Here, the pits have a diameter of around 600 nm, giving a lower fill factor than the optimum calculated in [7], but in the range where an increase in light trapping efficiency is simulated. Higher intensities lead to melting of the substrate, instead of creating ordered structures with larger pits. In the right image we observe a rim of debris around the pits. This rim has also been observed in Ref. [8], where an HF dip was suggested to remove the rim. We performed a 5 min, 20 % HF dip, which removed the rim, but which also degraded some of the smoothness of the processing result. The depth of the pits was investigated in an AFM, before removal of the rim. We found the depth of the pits to be around 100 nm. This is a considerable depth, but shallower than the depth suggested in [5].

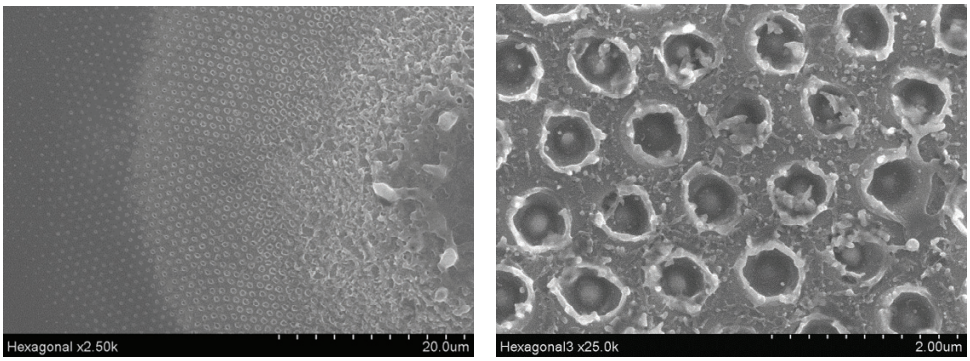


Fig. 1. Wafer surface after laser irradiation through microspheres.(a) The Gaussian intensity distribution, leading to melting near the center of the beam. (b) A close-up of the pits created

### *3.2. Process 2: Local opening of etch barrier by laser irradiation*

Our second approach (see Table 1) is based on depositing the PS-spheres on top of a $SiN_x$ etch barrier, using the laser to create local openings in the $SiN_x$. Microspheres were deposited on a 150 nm thick $SiN_x$ etch barrier on a silicon wafer, and this structure was irradiated by laser, forming openings in the etch barrier and pits into the silicon. Remaining spheres were removed with sonication. Thereafter, a 15 - 30 second etch in the 1:40:15 HNA solution was performed. It was observed that, while this etch enhanced the depth of the pits in the silicon, considerable under-etching of the etch barrier was also observed, thereby limiting the available etch time before etch barrier collapse. Therefore, rather limited pit depths were obtained using this solution. A possible reason for the under-etch, could be an interface oxide layer between the silicon and the $SiN_x$. To overcome the problem of under-etching, we increased the HF-concentration gradually to HNA 5:40:15. If the under-etch rate is limited by transport in the layer between the silicon and the $SiN_x$, a more rapid etch would allow for deeper pits while limiting the under-etch. This is indeed what was observed, shown in Fig. 2. Shorter etches in a more HF-rich HNA solution provided deeper pits without etch barrier collapse.

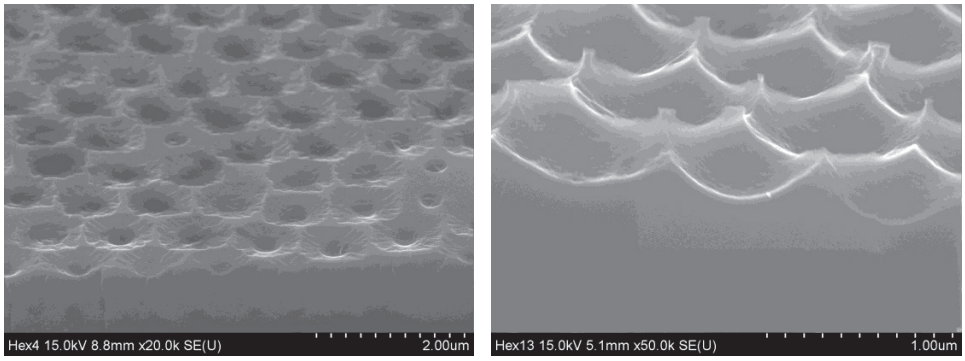


Fig. 2. Wafer surface after laser irradiation through etch barrier and subsequent etching, using (a) 1:40:15 HNA (b) 3:40:15 HNA

Structures similar to those shown in Fig. 2, but etched with a 5:40:15 HNA solution were also investigated using AFM for depth profiling. The results are shown in Fig 3. A depth of around 350 nm and a base diameter of around 800 nm were observed, giving nearly hemispherical pits.

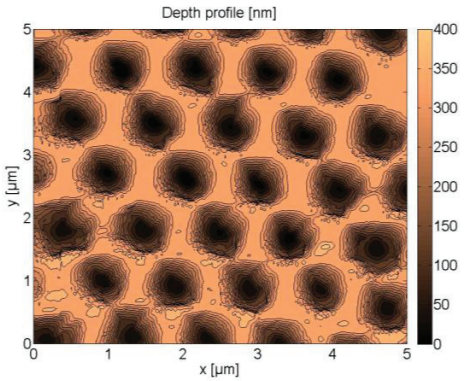


Fig. 3. Depth profile of wafer surface after laser irradiation through etch barrier and subsequent etching, using 5:40:15 HNA. The depth of the structures is around 350 nm and the base diameter around 800 nm

### *3.3. Process 3 : $SiN_x$ deposition on microspheres*

The third processing possibility investigated, was to deposit silica mircospheres on the silicon wafer, followed by PECVD-deposition of $SiN_x$ on top of this structure. After this deposition, the silica spheres were removed by sonication. In [9], this method was shown to give a shallow $SiN_x$ coverage over the majority of the wafer, while small openings remained where the spheres had been in contact with the wafer. In [9], a KOH etch was performed through these openings, showing that the $SiN_x$ acted as an etch barrier, and that the attack points were on the order of 100 nm. We reproduced this result using a KOH etch, however, we did not succeed in creating hemispherical structures using the HNA etch. We observed a rapid collapse of the etch barrier, and the structures created were very shallow. In [9] the thickness of the $SiN_x$ layer was suggested to be below 5 nm, a thickness which would rather rapidly be dissolved in our HF-containing HNA-solution.

## 4. Discussion

We have investigated three different processes to create hemispherical dimples in silicon wafers. These processes are summarized in Table 1. Process 3 proved to have an insufficient etch barrier for the HNA etch, failing to give depth to the structures. Process 1 gave dimples in the silicon, but the dimples were too shallow for our simulated target depth. Process 2 gave close to hemispherical shapes with a depth of around 350 nm. These shapes are of a size which is simulated to give good light trapping properties.

For large-area processing, Fig. 1a shows the industrial potential of this method. A high energy laser pulse would have the possibility to create thousands or even millions of pits using a single laser pulse. However, a top-hat laser beam profile would be required, in order to avoid the inhomogeneous processing resulting from the gaussian beam. A square, top-hat laser beam could be scanned over the surface of the wafer, rapidly being able to cover the whole wafer surface. A laser with a spot size of 400x400 µm and a repetition rate of 100 kHz would be able to cover a 5 inch wafer in one second. In [10], a method is

presented where the microspheres, instead of being deposited on the wafer, is deposited on a transparent carrier placed above the wafer. This method could allow for re-use of the 2D template, potentially simplifying the process.

## 5. Conclusion

We have created hexagonally ordered pits in a silicon wafer with 1 μm lattice period based on self-ordered PS-spheres. When depositing the spheres directly on a silicon wafer followed by irradiation by laser, pits with a diameter and depth of 600 nm and 100 nm respectively were created.

When depositing the spheres on a $SiN_x$ etch barrier, followed by laser irradiation and a subsequent isotropic etch, close to hemispherical dimples were created in the silicon, with a depth of around 350 nm and a base diameter of 800 nm. These dimensions are in a range where light trapping properties are expected. As we employ an isotropic etch, this process will be suitable for <100> and <111> mono-crystalline silicon as well as for multi-crystalline silicon.

## Acknowledgements

This work has been funded by the Research Council of Norway through the project “Thin and highly efficient silicon-based solar cells incorporating nanostructures”, NFR Project No. 181884/S10.

## References

[1] F. Henley, S. Kang, Z. Liu, L. Tian, J. Wang and Y.-L. Chow, “Beam-induced wafering technology for kerf-free thin PV manufacturing”, Proceedings of the 34th IEEE Photovoltaic Specialists Conference, Philadelphia, Pennsylvania, USA, 2009, pp. 001718-001723

[2] A. Gombert, K. Rose, A. Heinzel, W. Horbelt, C. Zanke, B. Bläsi and V. Wittwer, “Antireflective submicrometer surface-relief gratings for solar applications”, Sol. Energy Mater. Sol. Cells 54, 333 (1998)

[3] S. H. Zaidi, J. M. Gee and D. Ruby, Proceedings of the 28th IEEE Photovoltaic Specialists Conference, Anchorage, AK, 2000, pp. 395–398.

[4] P. C. Tseng, M. A. Tsai, P. Yu and H. C. Kuo, “Antireflection and light trapping of subwavelength surface structures formed by colloidal lithography on thin film solar cells”, Progress in Photovoltaics: Research and Applications, 2011.

[5] J. Gjessing, A. S. Sudbø and E. S. Marstein, “Comparison of periodic light-trapping structures in thin crystalline silicon solar cells,” Journal of Applied Physics 110 (3), 033104, (2011)

[6] J. Gjessing, E. S. Marstein and A. Sudbø, “2D back-side diffraction grating for improved light trapping in thin silicon solar cells.,” Optics express 18 (6), pp. 5481-95, 2010.

[7] S. M. Huang et al., “Pulsed laser-assisted surface structuring with optical near-field enhanced effects,” Journal of Applied Physics 92 (5), p. 2495-2500, 2002.

[8] D. Brodoceanu, L. Landström and D. Bäuerle, “Laser-induced nanopatterning of silicon with colloidal monolayers,” Applied Physics A 86 (3), pp. 313-314, 2006.

[9] E. Haugan, H. Granlund, J. Gjessing and E. S. Marstein, “Colloidal Crystals as Templates for Light Harvesting Structures in Solar Cells,” Proceedings of the European Materials Research Society Conference, 2011, pp. 1-5.

[10] K. Piglmayer, R. Denk and D. Bäuerle, “Laser-induced surface patterning by means of microspheres,” Applied Physics Letters, vol. 80, no. 25, p. 4693, 2002.

# PAPER IV

J. Thorstensen, J. Gjessing, E. S. Marstein, and S. E. Foss, "Light-trapping Properties of a Diffractive Honeycomb Structure in Silicon," *IEEE Journal of Photovoltaics,* vol.3, no. 2, pp. 709 – 715, 2013.

# PAPER V

J. Thorstensen and S. E. Foss, "Temperature dependent ablation threshold in silicon using ultrashort laser pulses," *Journal of Applied Physics,* vol. 112, no. 10, p. 103514, 2012.

# Temperature dependent ablation threshold in silicon using ultrashort laser pulses

Jostein Thorstensen[1,2,a)] and Sean Erik Foss[1]
[1]*Institute for Energy Technology, P.O. Box 40, 2027 Kjeller, Norway*
[2]*University of Oslo, Department of Physics, P.O. Box 1048 Blindern, 0316 Oslo, Norway*

(Received 26 April 2012; accepted 20 October 2012; published online 21 November 2012)

We have experimentally investigated the ablation threshold in silicon as a function of temperature when applying ultrashort laser pulses at three wavelengths. By varying the temperature of a silicon substrate from room temperature to 320 °C, we observe that the ablation threshold for a 3 ps pulse using a wavelength of 1030 nm drops from 0.43 J/cm$^2$ to 0.24 J/cm$^2$, a reduction of 43%. For a wavelength of 515 nm, the ablation threshold drops from 0.22 J/cm$^2$ to 0.15 J/cm$^2$, a reduction of 35%. The observed ablation threshold for pulses at 343 nm remains constant with temperature, at 0.10 J/cm$^2$. These results indicate that substrate heating is a useful technique for lowering the ablation threshold in industrial silicon processing using ultrashort laser pulses in the IR or visible wavelength range. In order to investigate and explain the observed trends, we apply the two-temperature model, a thermodynamic model for investigation of the interaction between silicon and ultrashort laser pulses. Applying the two-temperature model implies thermal equilibrium between optical and acoustic phonons. On the time scales encountered herein, this need not be the case. However, as discussed in the article, the two-temperature model provides valuable insight into the physical processes governing the interaction between the laser light and the silicon. The simulations indicate that ablation occurs when the number density of excited electrons reaches the critical electron density, while the lattice remains well below vaporization temperature. The simulated laser fluence required to reach critical electron density is also found to be temperature dependent. The dominant contributor to increased electron density is, in the majority of the investigated cases, the linear absorption coefficient. Two-photon absorption and impact ionization also generate carriers, but to a lesser extent. As the linear absorption coefficient is temperature dependent, we find that the simulated reduction in ablation threshold with increased substrate temperature is linked to the temperature dependence of the linear absorption coefficient. Another factor influencing the ablation threshold is the wavelength dependence of the interaction with the excited electron plasma. This wavelength dependence can explain that we observe experimentally similar ablation thresholds for a wavelength of 1030 nm at 320 °C and for 515 nm at room temperature, even though the linear absorption coefficient in the latter case is much higher.
 [http://dx.doi.org/10.1063/1.4766380]

## I. INTRODUCTION

Ultrashort pulse lasers are finding their way into industrial applications as a result of their minimal thermal influence on the workpiece, and their ability to process more or less any material, including materials which are transparent at moderate optical intensities.[1–3] In solar cell research and industry, ultrashort pulse lasers are of growing interest, due to the lower thermal influence and potentially higher quality process results and lower degradation of the electronic quality of the solar cell material.[4–6] In this article, we experimentally and theoretically investigate the interaction between ultrashort laser pulses and silicon.

When processing with laser pulses in the nanosecond range and moderate laser intensities, the laser can essentially be described as a heat source, providing a distributed energy input to the material. The material experiences a temperature rise described by the (linear) laser absorption coefficient and pulse duration, and by material parameters such as heat capacity and heat conductivity. The heat equation can be applied in order to solve for the temperature evolution in the substrate. Observable changes to the material normally occur when melting or vaporization temperatures are reached.[1]

With ultrashort pulses in the pico- and femtosecond range, the interaction between light and matter starts to deviate from this behavior. In semiconductors, we have to describe the laser as an energy source to the conduction band electron system (from here: electron system), raising both the temperature and the number density of this system. The laser penetration depth (or the corresponding effective absorption coefficient) becomes dependent on laser intensity through non-linear absorption and on the number density of conduction band electrons (from here: electron density) through free-carrier absorption. The electron system dissipates energy to the lattice system through collisions on a time-scale which can be comparable to, or longer than the

[a)]Author to whom correspondence should be addressed. Electronic mail: jostein.thorstensen@ife.no.

 

pulse duration. As a result of this, the temperature of the electron system may, during the pulse, be significantly higher than the temperature of the lattice system. In order to model the evolution of such a system, we need separate coupled heat equations for the electron and lattice systems. Bulgakova *et al.*[7] provide an excellent review of several different approaches to the modeling of interactions between ultrashort laser pulses and dielectrics, semiconductors and metals. The more elaborate models take electron emission from the surface and electric fields within the material into account.

In this work, we perform ablation from a silicon substrate using 3 ps laser pulses at wavelengths of 343, 515, and 1030 nm. The temperature of the silicon substrate is varied between 25 and 320 °C, and the ablation threshold fluence is measured as a function of temperature. The ablation threshold fluence (ablation threshold) is defined as the minimum laser pulse fluence required for material removal. In order to explain the experimental results and trends, we wish to model the interaction between the laser pulse and the silicon substrate. A model often chosen for its relative simplicity is referred to as the two-temperature model, where we have separate heat equations for the electron and lattice systems. Significant work on the two temperature model has been performed, some main findings summarized by Bäuerle.[1] When choosing to use the two-temperature model, we are aware that this is a simplified model, leaving out a number of effects which are described in the three-temperature model or in full kinetic models. The three-temperature model divides the lattice system into optical and acoustic phonons, and energy transfer from the electrons is primarily to optical phonons, which in turn transfer the energy to the acoustic phonons. As such, the two-temperature model will give a stronger and more rapid lattice heating than if using the three-temperature model. Effects which can be described in full kinetic models, such as incomplete thermalization of electrons and drift in electric fields and phenomena related to the elastic stress of the silicon crystal are also left out of our model. Nevertheless, we believe that we can extract much information about the physics of our experiments with the comparatively less elaborate two-temperature model. Sim *et al.*[8] present a theoretical study on the two- and three-temperature models in silicon, while Mao *et al.*[9] apply a two-temperature model with electron emission. Christensen *et al.*[10] apply a two-temperature model for metals. We vary the simulated substrate temperature, and extract information about the dynamics of the ablation process.

## II. EXPERIMENTS

We have performed experiments investigating the temperature dependence of the ablation threshold of an 80 nm thick layer of amorphous silicon nitride ($SiN_x$) with an index of refraction of $n = 2.1$, deposited by plasma-enhanced chemical vapor deposition (PECVD) at 400 °C, on a silicon wafer. In these experiments, the $SiN_x$, a dielectric commonly investigated for thin film ablation, plays a passive role, and is only included in order to make the ablation more easily visible. The $SiN_x$ will be lifted off in the areas where the Si experiences ablation. We apply pulses with pulse duration of 3 ps, a repetition rate of 1 kHz and three wavelengths, namely 343, 515, and 1030 nm to the silicon wafer. An xy-table translates the wafer, ensuring a spatial separation of the pulses of 100 $\mu$m. The $1/e^2$ diameters of the Gaussian intensity profile of the pulses are approximately 10, 30, and 44 $\mu$m at 343, 515, and 1030 nm, respectively. A to-scale illustration of the irradiation geometry is shown in Fig. 1. We see that the $SiN_x$ film thickness and the laser penetration depth are both much smaller than the spot radius. We apply several different intensities per wavelength and temperature, and apply the method of Liu,[11] where the relation between ablated radius and pulse energy is used in order to accurately determine the ablation threshold fluence and beam diameter,

$$r_{abl}^2 = \frac{c^2}{2}\ln\left(\frac{F_0}{F_{th}}\right) = \frac{c^2}{2}\left[\ln\left(\frac{2E}{\pi c^2}\right) - \ln(F_{th})\right]. \quad (1)$$

Here, $r_{abl}$ is the ablated radius, $c$ is the beam diameter at $1/e^2$ fluence level, $F_0$ and $F_{th}$ are the peak fluence of the laser pulse and the ablation threshold fluence, respectively. The right hand side expression contains only the ablated radius and pulse energy $E$, which both can be measured, and the unknown quantities, namely ablation threshold and beam diameter. We have measured the wavelength-dependent reflectance of our samples, and subtract the reflected light from our reported ablation thresholds so that we are only looking at the light entering the silicon.

The temperature of the silicon wafer was varied by placing the wafer on a heating plate in ambient air. The temperature was recorded both at the heating plate and at the surface of the silicon wafer, both measured using a thermocouple. The discrepancy between these measurements indicates imperfect thermal contact in our setup. The temperature recorded at the silicon surface is taken as the sample temperature, while the temperature of the heating plate is taken as an upper boundary.


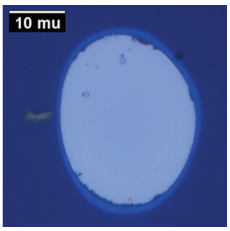


FIG. 1. Left: The irradiation geometry. The silicon wafer (grey) is covered with a thin silicon nitride ($SiN_x$) layer (blue) which is removed by a laser pulse (green). $SiN_x$ film thickness and laser penetration depth are both small compared to the laser spot radius. Right: Microscope image of an ablated spot, showing the contrast between silicon (light blue) and surrounding $SiN_x$ (dark blue).

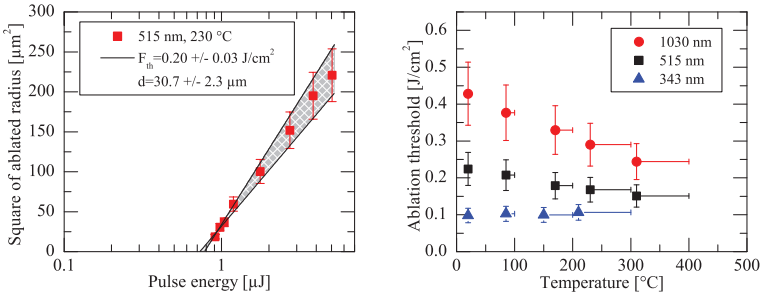


FIG. 2. Experimental data for determination of ablation threshold (left) (before subtracting reflectance). Ablation threshold for silicon at 343, 515, and 1030 nm, 3 ps pulse duration (right).

## III. EXPERIMENTAL RESULTS

The reflectance is measured at low light intensity using a broadband light source consisting of a deuterium and a tungsten halogen lamp, at an incidence angle of 8° in a spectrometer-based integrating sphere setup. The reflection coefficients measured are 0.60, 0.17, and 0.16 at 343, 515, and 1030 nm, respectively. At high optical intensities, however, the reflection coefficient will change from its low intensity value, due to the influence on dielectric constants from the large number density of excited electrons as will be discussed in Sec. IV B. In an experiment, we have monitored reflected power as function of incident power as we irradiate our samples using our laser at wavelengths 515 nm and 1030 nm using the laser parameters described in Sec. II, at 15° incidence angle, thereby measuring the time-averaged reflectance from our sample. The wafer was moved using the xy-table, ensuring non-overlapping laser spots, as described in Sec. II. At intensities below the observed ablation threshold, we observe a decrease in reflectance by 2% absolute (12% relative). The observed variation, however, is on the order of the inaccuracy of our reflectance measurements. Increasing the incident power beyond the ablation threshold, the reflectance rises steadily by up to 70% relative at laser intensities much higher than the ablation threshold. A decrease in reflectance can be expected at electron densities approaching the critical electron density,[12] followed by a sharp increase in reflectance when the critical electron density is reached (Fig. 3). The observed increase in average reflectivity indicates that the critical electron density is encountered earlier in the pulse with increasing laser fluence. However, near the ablation threshold, critical electron density is encountered late in the pulse. For the fluence range discussed herein, the reflectance remains at the low intensity value, or is in fact lowered somewhat, and we therefore approximate the reflectance to be constant at the low intensity value.

An example of the data for extraction of the ablation threshold is shown in Fig. 2 (left), along with the measured ablation thresholds at 343, 515, and 1030 nm at temperatures from room temperature to 320 °C (right). Well-defined ablation spots are observed, and we estimate an uncertainty in the measured ablation threshold of ±20%, based on uncertainty in measured ablated diameter and deviation from the trend in Eq. (1) and the uncertainty of the power meter. The ablation threshold at 515 and 1030 nm decreases with increasing substrate temperature, while it remains constant at 343 nm.

## IV. SIMULATION MODEL

In order to investigate the physics behind the experimental results, simulations are performed, using the before mentioned two-temperature model. The two-temperature model is a tool for modeling a situation with different temperature in the electron and lattice systems. One assumption of the model is that the electrons reach a thermal distribution on a time-scale which is short compared to the pulse duration. The electron thermalization time is reported to be around 10 fs,[8] meaning that this criterion is well fulfilled in our case. The two-temperature model can mathematically be written as a set of coupled differential equations. In order to reduce the required equations to containing only one spatial variable, we shall make the approximation that the incoming laser power is uniformly distributed over the silicon surface, i.e., the laser spot is homogeneous and infinitely large. As

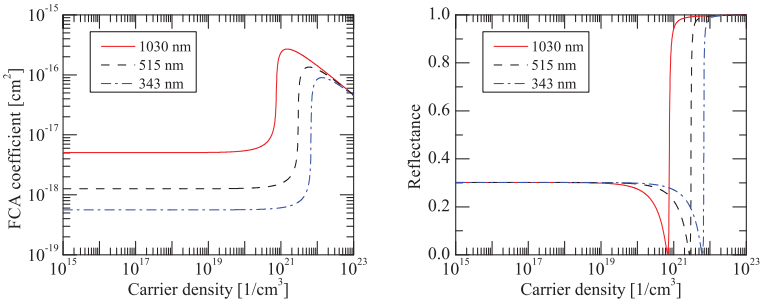


FIG. 3. Theoretical free carrier absorption coefficient (left) and reflection coefficient (right) as functions of carrier density, for three wavelengths.

shown in Fig. 1, the laser penetration depth is smaller than the spot radius by at least an order of magnitude, making the approximation reasonable. Following Sim *et al.*,[8] adding diffusion of carriers,[13] we write the equations

$$\frac{\partial U_e}{\partial t} = \frac{\partial}{\partial x}\left(k_e \frac{\partial T_e}{\partial x}\right) + \frac{\partial}{\partial x}\left(E_g D_0 \frac{\partial N}{\partial x}\right) - \frac{3Nk_b}{\tau_{e-l}}(T_e - T_l) + q_{tot}, \tag{2}$$

$$\frac{\partial U_l}{\partial t} = C_l \frac{\partial T_l}{\partial t} = \frac{\partial}{\partial x}\left(k_l \frac{\partial T_l}{\partial x}\right) + \frac{3Nk_b}{\tau_{e-l}}(T_e - T_l), \tag{3}$$

$$\frac{\partial N}{\partial t} = \frac{\partial}{\partial x}\left(D_0 \frac{\partial N}{\partial x}\right) - \gamma' N^3 + \delta N + \sum \frac{a_n I^n}{n\hbar\omega}. \tag{4}$$

The meaning and value of all parameters are tabulated in Tables I and II. Equations (2) and (3) are heat/diffusion equations with the temporal change in energy being balanced by diffusion terms and source terms. Equation (2) describes the energy in the conduction band electron system and Eq. (3) the energy in the lattice system. Equation (4) is a continuity equation for the number density of conduction band electrons. $q_{tot}$ is a collective source term covering all laser absorption mechanisms. For the case of silicon and wavelengths between 343 and 1030 nm, we only consider linear and two-photon band-to-band absorption, along with free carrier absorption (FCA), and we can write $q_{tot}$ as[1]

$$q_{tot} = \alpha_{tot} I = -\frac{dI}{dx} = \sum a_n I^n + \theta N I \simeq \alpha I + \beta I^2 + \theta N I, \tag{5}$$

where I is the optical intensity. As the intensity at a depth x is depending on the absorption between the surface and the position x, we need to express the intensity as an integral equation. We integrate Eq. (5) to obtain

$$I(t,x) = I_0(\mathrm{t}) \exp\left( - \int_0^x \left[ \sum a_n I(t,x')^{n-1} + \theta N(t,x') \right] dx' \right). \tag{6}$$

In this equation, we have ignored the time delay experienced by the pulse as it travels through the workpiece. Note that $I_0(t) = I(t,x=0)$ is the intensity of the laser pulse entering the silicon surface, equal to the incoming intensity minus the reflected intensity.

Going a bit more into the details of Eqs. (2)–(6), we see that linear and non-linear band-to-band absorption mechanisms, along with free-carrier absorption, increase the energy stored in the electron system. Linear and non-linear band-to-band absorption introduces energy as both potential energy (increase of number density of electrons) and kinetic energy (electron system temperature). Free-carrier absorption only introduces kinetic energy. Auger and impact ionization processes do not contribute to the overall energy of the electron system, but transfer energy to kinetic energy and potential energy (number density of electrons), respectively. Kinetic

TABLE I. Explanation of symbols encountered in the equations for the two-temperature model.

| Symbol | Parameter | Value | Unit | Reference |
|---|---|---|---|---|
| $U_e$ | Electron system thermal energy | $3Nk_bT_e$ | J/m$^3$ | |
| $N$ | Number density of electrons | | 1/m$^3$ | |
| $k_b$ | Boltzmann constant | $1.38 \times 10^{-23}$ | J/K | |
| $T_e$ | Electron temperature | | K | |
| $k_e$ | Electron heat conductivity | $-0.556 + 7.13 \times 10^{-3} T_e$ | W/(K m) | 25 |
| $\tau_{e\text{-}l}$ | Electron-lattice coupling time | $240 \times 10^{-15} \times \left(1 + \left(\frac{N}{N_{cr\_sh}}\right)^2\right)$ | s | 15 |
| $N_{cr\_sh}$ | Shielding electron density | $6 \times 10^{26}$ | 1/m$^3$ | 15 |
| $a_n$ | n-th order absorption coefficient | see Table II | | |
| $\theta$ | Free-carrier absorption coefficient | see Table II | | |
| $U_l$ | Lattice system thermal energy | $C_l T_l$ | J/m$^3$ | |
| $T_l$ | Lattice temperature | | K | |
| $C_l$ | Lattice heat capacity | $2.2368 \times 10^6$ (300 K $< T_l <$ 1683 K) | J/(m$^3$ K) | 26 |
| $k_l$ | Lattice heat conductivity | $1.521 \times 10^5 T_l^{-1.226}$(300 K $< T_l <$ 1200 K)<br>$896 \times T_l^{-0.502}$(1200 K $< T_l <$ 1683 K) | W/(K m) | 26 |
| $D_0$ | Electron diffusivity | $2.98 \times 10^{-7} T_e$ | m$^2$/s | 7 |
| $\gamma' N^3$ | Screened Auger recombination | $N/\left(\frac{1}{\gamma N^2} + t_{min}\right)$ | | 7, 20 |
| $\gamma$ | Auger coefficient | $3.8 \times 10^{-43}$ | m$^6$/s | 13 |
| $t_{min}$ | Minimum Auger lifetime | $6 \times 10^{-12}$ | s | 7, 20 |
| $\delta$ | Impact ionization coefficient | $1.0 \times 10^{11}(U_e - E_g)^{4.6}$(energies in eV) | 1/s | 23 |
| $E_g$ | Band gap in silicon | $1.86 \times 10^{-19}$ | J | |
| $N_{cr}$ | Critical electron density | $6.2 \times 10^{27}$ (343 nm)<br>$2.7 \times 10^{27}$ (515 nm)<br>$6.9 \times 10^{26}$ (1030 nm) | 1/m$^3$ | 1, 14 |

TABLE II. Optical constants in silicon for three different wavelengths.

| Symbol | 1030 nm (measured at 1064 nm) | 515 nm | 343 nm | Unit | Reference |
|---|---|---|---|---|---|
| $a_1 = \alpha$ | $-5895 + 62.26T_l - 0.2309T_l^2$ $+3.186 \times 10^{-4}T_l^3 + 9.967 \times 10^{-8}T_l^4$ $-1.409 \times 10^{-11}T_l^5$ | $5.02 \times 10^5 \exp\left(\frac{T_l}{430}\right)$ | $1.09 \times 10^8$ | 1/m | 26, 27 |
| $a_2 = \beta$ | $1.5 \times 10^{-11}$ | $1.8 \times 10^{-12}$ | 0 | m/W | 28 and 29 |
| $\theta$ | $5 \times 10^{-22}\left(\frac{T_l}{300}\right)$ | $1.2 \times 10^{-22}\left(\frac{T_l}{300}\right)$ | $5.4 \times 10^{-23}\left(\frac{T_l}{300}\right)$ | $m^2$ | 28 |

energy loss from the electron system also occurs through the electron-lattice coupling term. Radiative and Shockley-Read-Hall recombination mechanisms take place over much longer time scales than our pulses and are therefore neglected in our simulations.

We use a partial differential equation solver with one spatial dimension in order to solve the three coupled equations (2)–(4) and the equation for optical intensity (6). We simulate Gaussian laser pulses centred at $t = 0$ and a pulse duration of 3 ps (FWHM), for irradiation wavelengths of 343, 515, and 1030 nm. We take the intrinsic doping level (carrier density) to be $10^{16}$ 1/cm$^3$. The pulse fluence is increased in steps of 3% until one of the criteria for ablation is reached.

### A. Ablation threshold in simulations

There are two possible mechanisms causing ablation when a sample is irradiated by a laser pulse. The first mechanism is the "thermal ablation," which occurs if the lattice reaches vaporization temperature. This mechanism is typical when applying long laser pulses. The second, "non-thermal ablation" is typical for short pulses, and occurs if the number density of conduction band electrons reaches a critical density, suggested to be $2.7 \times 10^{21}$ 1/cm$^3$ for irradiation at 532 nm.[14] Details on the physics in such a dense plasma are described by a free-electron gas, summarized in Sec. IV C. The mechanism signifying ablation in our simulations is the mechanism which reaches ablation threshold first.

### B. Comments on the parameters

In Tables I and II, we have stated values for several material properties of silicon. For many of these parameters, several groups report values which differ significantly.

We have used an **electron-lattice coupling time** of $240 \times (1 + (N/N_{cr})^2)$ fs,[15] based on experiments on silicon. However, several articles[16,17] make use of much longer coupling times of around 1–10 ps, based on work by van Driel[13] and measurements on GaAs,[18] which we expect to be less representative for our case. The three-temperature model described by Sim *et al.*[8] uses values from a general statement in the book by Tien *et al.*[19] that electron–optical phonon coupling is on the order of 100 fs, while the optical phonon-acoustic phonon coupling time is on the order of 10 ps for "most semiconductors."

**Auger recombination** at high electron densities is also subject to uncertainty. Yoffa[20] predicts theoretically a minimum value for the Auger lifetime of 6 ps as a result of Coulomb-screening. On the other hand, experimental work[21] indicates Auger lifetimes down to and below 1 ps without deviation from the $N^{-2}$ trend for Auger lifetime. Here, polycrystalline silicon was used, however, with properties close to those of crystalline silicon.

For the **electron diffusivity**, we have used $2.98 \times 10^{-7} T_e$ (m$^2$/s),[7] while van Driel[13] uses $18 \times 10^{-3}$ $(300/T_l)$ (m$^2$/s). The impact ionization coefficient has generally only been simulated, and the values reported vary strongly. Examples are $3.6 \times 10^{10} \exp(-1.5E_g/(k_B T_e))$(1/s),[13] $10^{11} \times ((U_e - 1.2)/1.2)^2$ (1/s),[22] and $10^{11} \times (U_e - E_g)^{4.6}$ (1/s) (with $U_e$ and $E_g$ in eV).[23]

For the 1030 nm wavelength, we have used values for **the linear absorption coefficient** based on measurements at 1064 nm. The temperatures encountered in our simulations are higher than those reported in the measurements (up to 200 °C); however, other work[24] indicates that the extrapolation is valid also to temperatures up to around 850 °C. At 515 and 343 nm, the temperature dependence is based on measurements up to 700 °C.

Generally, where we have found several different values for parameters, we have used the newest values available, or the ones where the simulations or experiments most closely resemble our experimental conditions. It is important to be aware of the large discrepancies in reported experimental values for some of the parameters used in these simulations. This represents a significant source of uncertainty in our simulation results.

### C. Free-electron gas

Many excellent books review the Drude free-electron theory. Briefly summarized, a free-electron gas will have a dielectric response according to[30,31]

$$\epsilon = \epsilon' + i\epsilon'' = \epsilon_{bg}\left(1 - \frac{\tilde{\omega}_p^2}{\omega^2 + \gamma^2}\right) + i\frac{\epsilon_{bg}\tilde{\omega}_p^2\gamma}{\omega(\omega^2 + \gamma^2)}, \quad (7)$$

$$n + ik = \sqrt{\epsilon}, \quad (8)$$

where $\epsilon_{bg}$ is the background relative permittivity of the silicon material without free carriers. We define $\tilde{\omega}_p^2 = \frac{Ne^2}{\epsilon_{bg}\epsilon_0 m_{eff}}$ as the plasma frequency with a dielectric background, $\gamma$ is the reciprocal collision time, $m_{eff}$ is the effective electron mass, and $\omega$ is the frequency of the applied electric field. With $\gamma \ll \omega$, the real part of the dielectric coefficient equals zero when $\tilde{\omega}_p = \omega$. $k$ is an expression for the attenuation

caused by free carriers, that is the free carrier absorption. Dividing this expression by $N$ gives the free-carrier absorption coefficient. In some limiting cases, the expression can be simplified, some results are given here. For the case $(\tilde{\omega}_p, \gamma) \ll \omega$, the expression (7) simplifies to

$$\epsilon = \epsilon' + i\epsilon'' = \epsilon_{bg}\left(1 + i\frac{\tilde{\omega}_p^2\gamma}{\omega^3}\right), \tag{9}$$

$$n + ik = \sqrt{\epsilon_{bg}}\left(1 + i\frac{\tilde{\omega}_p^2\gamma}{2\omega^3}\right), \tag{10}$$

which yields

$$\alpha_{fca} = \theta N = \frac{2\omega k}{c} = \frac{\sqrt{\epsilon_{bg}}\tilde{\omega}_p^2\gamma}{\omega^2 c} = \frac{\sqrt{\epsilon_{bg}}\tilde{\omega}_p^2\gamma}{4\pi^2 c^3}\lambda^2 = \frac{e^2\gamma}{4\pi^2\epsilon_0 m_{eff}\sqrt{\epsilon_{bg}}}N\lambda^2. \tag{11}$$

For our case, this corresponds to the situation with low electron densities and small values of $k$, and this is the well-known $\lambda^2$ behavior of the FCA. We also see that FCA is proportional to $N$, meaning that $\theta$ is constant with $N$. However, an increase in $N$ will eventually increase $\tilde{\omega}_p$ to the point where it is approaching $\omega$, and the absorption will deviate from the low electron density limit, meaning that the approximations in Eqs. (9)–(11) will no longer hold. Fig. 3 (left) shows the FCA coefficient in silicon, based on the expressions (7) and (8) and values in Tables I and II, plotted as a function of $N$, for wavelengths of 343, 515, and 1030 nm. It is clear that we, when $\tilde{\omega}_p$ approaches $\omega$, will see a dramatic increase in FCA, as a result of the sharply increasing FCA-coefficient, leading to the formation of a highly absorbing electron gas near the surface of the substrate. This gas will reach very high electron temperatures and temperature gradients. These gradients are suggested[17] to be the driving force for lattice expansion, resulting in lattice stress to the point of material fracture. We take this as the physical mechanism behind the "non-thermal ablation," and we therefore define $N_{cr}$ as $N_{cr} = N(\tilde{\omega}_p = \omega)$. This gives

$$N_{cr} = \frac{\omega^2\epsilon_{bg}\epsilon_0 m_{eff}}{e^2} \propto 1/\lambda^2. \tag{12}$$

Based on the findings in Eqs. (11) and (12), we extrapolate reported values for $N_{cr}$[14] and $\theta$[28] to the wavelengths encountered herein. Also, when $\tilde{\omega}_p$ approaches $\omega$, $n$ and $k$ will deviate significantly from the low electron density value, as the contributions from the free electron gas grow. As the reflection is dependent on $\epsilon$, the reflectance of the sample will change during the pulse. Fig. 3 shows the reflectance as function of carrier density. However, as explained in Sec. III, the reflectance will start changing late in the pulse at fluencies close to the ablation threshold, giving only a minor change in the average reflectance. Hence, the reflectance change is omitted in the simulations.

## V. ANALYSIS OF SIMULATIONS

From our simulations, we extract the electron generating dynamics and the temperature evolution of our sample. Fig. 4 (left) shows contributions to the electron density from the individual carrier generating mechanisms, and we see that the critical electron density of $6.9 \times 10^{20}$ 1/cm$^3$ is reached towards the end of the pulse. The right figure shows the temperature in the lattice and electron systems at the surface of the sample. We clearly see that the electron system is much hotter than the lattice system during the pulse, and that equilibrium is reached shortly after the pulse. The lattice temperature stays below 1000 K, well below melting temperature. Hence, ablation is non-thermal, and follows from reaching $N_{cr}$. This behavior is seen for all of our simulations. As the electron density clearly plays a crucial role, we investigate the electron density created by the various mechanisms. In silicon, carriers are generated through linear and two-photon absorption and from impact ionization, while carriers are removed through Auger recombination.

### A. Substrate at 27 °C

The simulations show that, at 343 and 515 nm, linear absorption is the dominant electron generating mechanism. At 1030 nm, however, two-photon absorption accounts for over half of the generated electrons, closely followed by linear absorption. The modeled electron density for 1030 nm, 27 °C, 3 ps pulse duration, and a pulse fluence of 0.58 J/cm$^2$ is shown in Fig. 4 (left). It is interesting to observe that the two-photon absorption is centered on the peak of the pulse, while the linear absorption is clearly shifted towards the end of the pulse as a result of the temperature dependence of the linear absorption coefficient. This is more clearly seen in Fig. 5. Significant electron densities are created even during the very weak leading flanks of the Gaussian pulse. Impact

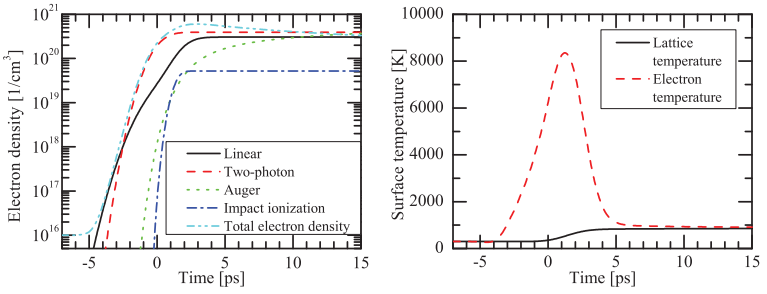


FIG. 4. Simulated contributions to the cumulative generated electron number density (1/cm$^3$) from the various electron generating mechanisms (left) and lattice and electron temperatures (right) at the surface (z = 0) for 1030 nm excitation wavelength, pulse fluence 0.58 J/cm$^2$, 3 ps pulse duration (centered at t = 0) and 27 °C. Linear absorption and two-photon absorption are the main electron generating mechanisms.

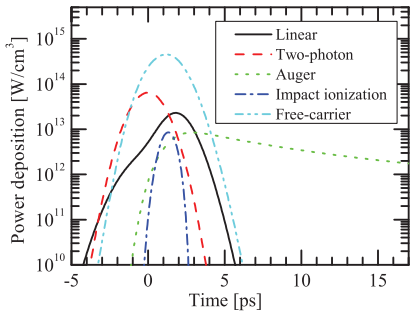


FIG. 5. Simulated power density deposition (W/cm$^3$) at the surface ($z = 0$); 1030 nm excitation wavelength, pulse fluence 0.58 J/cm$^2$, 3 ps pulse duration (centered at $t = 0$), 27 °C. Free-carrier absorption is the dominating absorption mechanism. For Auger and impact ionization, the power corresponds to the energy shifted between potential and kinetic electron energy.

ionization contributes with around 5% of the total number density of generated electrons. As Auger recombination is a strong function of electron density, its influence is strongest late in the pulse and after the pulse. (Auger recombination is of course not a source of electrons, but rather a sink for electrons, and should therefore be interpreted as having a negative sign.) Also shown in Fig. 4 (right) is the temperature evolution in the electron and lattice systems at the surface of the wafer, shown for the same pulse. The electron system is much hotter than the lattice system during the pulse, and that equilibrium is reached shortly after the pulse. The lattice temperature stays below melting temperature during the simulations.

### B. Varying substrate temperature, absorption mechanisms

We now increase the substrate temperature, by varying the initial and boundary conditions in our differential equations, and observe how the simulated ablation threshold changes.

The simulated ablation threshold and absorption coefficient in silicon are shown in Fig. 6. We see that the linear absorption coefficient at 515 nm and 1030 nm increases with increasing temperature. As absorption in indirect band-gap semiconductors is dependent on phonon assistance, the absorption coefficient increases with increasing temperature and phonon abundance. Simulations have shown[32] that the acoustic phonons are responsible for the temperature dependence of the linear absorption coefficient. At 343 nm, however, direct transitions are allowed in silicon, and no temperature dependence is observed,[27] as no phonon assistance is required for direct transitions.

At 343 nm, linear absorption is very strong, rendering all other contributions to absorption negligible. As a result of this combined with the temperature independence of the linear absorption at this wavelength, the simulated ablation threshold remains constant with varying temperature.

At 515 nm, linear absorption is the dominating absorption mechanism at room temperature, and due to its exponential increase with temperature, linear absorption is even more dominant at higher temperatures. This is shown in Fig. 7. The simulated reduction in ablation threshold is attributed to the stronger linear absorption.

At 1030 nm and 27 °C, two-photon absorption is the dominant carrier generating mechanism as shown in Fig. 4.

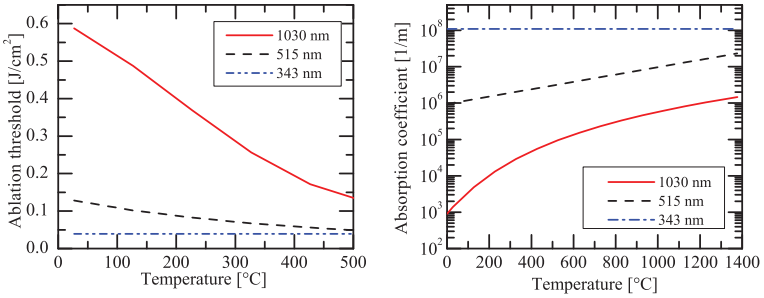


FIG. 6. (Left) Simulated ablation threshold for 3 ps pulses. (Right) The linear absorption coefficient for the three wavelengths as a function of temperature.

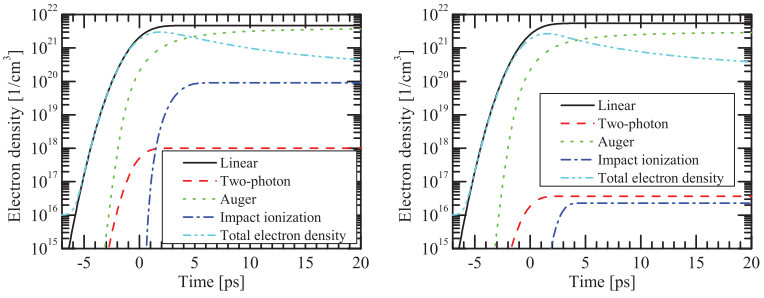


FIG. 7. Simulated cumulative generated electron number density (1/cm$^3$) at the surface ($z = 0$) for 3 ps pulse at 515 nm. Temperature and pulse fluence are 27 °C and 0.14 J/cm$^2$ (left) and 827 °C and 0.026 J/cm$^2$ (right), respectively. Linear absorption is dominant in both cases. Two-photon absorption and impact ionization are more suppressed at higher substrate temperatures.

However, this changes already at the next simulated temperature, 127 °C (400 K). From this temperature and upwards, linear absorption is the dominant mechanism, and the reduction in ablation threshold can be attributed to the increasing linear absorption coefficient.

### C. Impact ionization and free-carrier absorption

When working with ultrashort pulses, non-linear interactions are expected, as a result of the high optical intensities and high electron densities encountered. During a 3 ps pulse in silicon, however, our simulations show that the main contributor to the increased electron density is linear absorption. We would like to examine impact ionization and free-carrier absorption closer.

IR-pulses at room temperature experience the weakest linear absorption of our pulses. Under these conditions, the main energy absorption mechanism is actually free-carrier absorption, which at the surface of the wafer absorbs around 10 times as much energy as linear and two-photon absorption combined (Fig. 5). According to our simulations, the vast majority of the excess electron energy caused by FCA is transferred to the lattice through the electron-lattice coupling, which operates with a time constant of 240 fs in silicon.[15] As such, FCA contributes only indirectly to the ablation, by raising the lattice temperature and thereby raising the temperature dependent linear absorption. The only mechanism which could potentially transform electron kinetic energy into electron-hole pairs directly, namely impact ionization, is a too weak process to have any significant contribution.

### D. Varying electron-lattice coupling

The time constant of electron-lattice coupling is of great importance to the simulation results. As stated earlier, this constant is somewhat uncertain, and we have also chosen not to include the additional thermal delay between optical and acoustic phonons presented in the three-temperature model. We therefore wish to investigate the influence of an increased electron-lattice coupling time, as this could give results more similar to those obtained with the three-temperature model. In the three-temperature model, the temperature in the acoustic phonon system will remain lower, as the coupling time between optical and acoustic phonons is long.[19] The acoustic phonon temperature is the driving mechanism for the temperature dependent linear absorption coefficient in silicon,[32] and as such, longer time for the energy to reach the acoustic phonon modes would decrease the linear absorption experienced in the pulses.

In our simulations, we increase the coupling time to $1 \times (1 + (N/N_{cr})^2)$ ps. This will increase the temperature in the electron system, which in turn will promote stronger impact ionization. On the other hand, the lattice will remain cooler, decreasing the linear absorption. These two mechanisms result in a lower ablation threshold at 1030 nm, as the increased impact ionization outweighs the reduced linear absorption. At room temperature, the ablation threshold decreases from 0.58 J/cm$^2$ to 0.46 J/cm$^2$. As shown in Fig. 8, we observe that linear absorption dominates the electron generation in the beginning of the pulse, two-photon absorption dominates towards the peak of the pulse, while impact ionization dominates towards the end of the pulse, generating twice the number density of electrons compared with two-photon absorption. Contrary to this, the ablation threshold increases somewhat at 515 nm, because the reduced linear absorption is more important compared to contributions from impact ionization in this case. At 343 nm, linear absorption is dominant and not temperature dependent, and the ablation threshold therefore remains unchanged with varying electron-lattice coupling time.

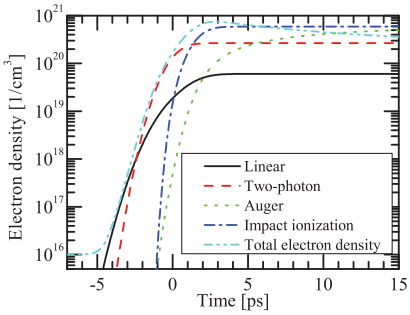


FIG. 8. Simulated cumulative generated electron number density (1/cm$^3$) at the surface (z = 0) for 1030 nm excitation wavelength, pulse fluence 0.46 J/cm$^2$, 3 ps pulse duration (centred at t = 0). Electron-lattice coupling time is $1 \times (1 + (N/N_{cr})^2)$ ps. Linear absorption, two-photon absorption, and impact ionization all dominate at different times during the pulse. Impact ionization is the most important electron generating mechanism.

### E. Auger recombination

As stated above, also the Auger recombination rate is subject to discussion. Experimental results[21] suggest that there is no screening of the Auger recombination down to 1 ps.

Therefore, we remove the lower bound on the Auger lifetime and repeat the simulations. As seen in Fig. 9, the simulated ablation threshold remains essentially unchanged at 1030 nm, while a substantial increase is observed for 343 and 515 nm. This is as expected due to the higher electron densities encountered using shorter wavelengths giving a

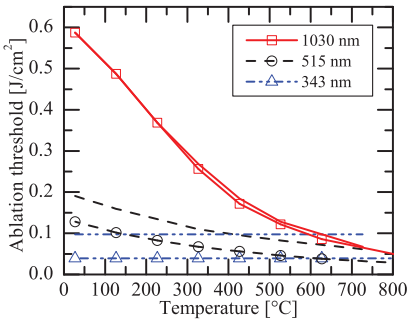


FIG. 9. Simulated ablation threshold with Auger lifetime limited to 6 ps (line + symbol), and with the limit removed (line). A substantial increase in simulated ablation threshold is observed for 343 and 515 nm.

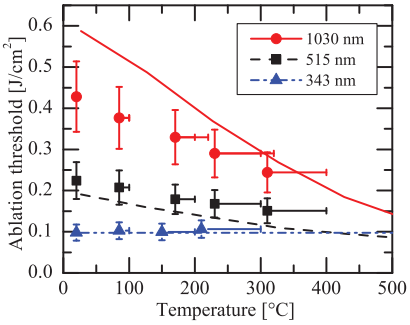


FIG. 10. Ablation threshold fluence for silicon at 343, 515, and 1030 nm (3 ps pulse duration). Symbols: Experimental values. Lines: Simulated ablation threshold using un-screened Auger recombination.

larger discrepancy between the screened and the un-screened Auger recombination rates. We also observe, however, that the temperature dependencies remain essentially unchanged.

## VI. COMPARING EXPERIMENTAL RESULTS AND SIMULATIONS

The measured ablation threshold at 343, 515, and 1030 nm at temperatures from room temperature to 320 °C is shown in Fig. 10, along with the simulation results using un-screened Auger recombination. Although there are discrepancies between simulations and experiments, the temperature dependencies of the ablation threshold are reproduced in simulations. An interesting point to note is that the experimentally observed ablation threshold at 1030 nm and 320 °C substrate temperature is similar to the experimentally observed ablation threshold at 515 nm at room temperature. We will discuss this in more detail. In simulations, we have identified the linear absorption as the most important absorption mechanism for all wavelengths at elevated temperatures. However, looking at the linear absorption coefficients, these are $10^4$ 1/cm and $3 \times 10^2$ 1/cm for 515 nm at room temperature and 1030 nm at 320 °C, respectively. This means that despite the fact that the laser pulse at 515 nm experiences a 35 times stronger absorption, the ablation thresholds are similar. In a linearly absorbing material where the ablation mechanism is vaporization, e.g., using pulses in the ns-range, pulses with such strong differences in absorption coefficient would certainly not see a similar ablation threshold. This effect must be related to the fact that we are applying ultrashort laser pulses. From our simulations, we can explain this result by two factors. First, the $\lambda^2$-dependence of the free-carrier absorption leads to stronger lattice heating at 1030 nm, resulting in a stronger temperature driven increase in absorption coefficient at 1030 nm. Second, and most importantly, the $1/\lambda^2$-dependence of $N_{cr}$ reduces the critical electron density at 1030 nm by a factor of 4 compared to that at 515 nm and hence reduces the required electron generation. To further verify this, simulations were performed where 515 and 1030 nm had the same $N_{cr}$. In these simulations, the ablation threshold at 515 nm was always lower than for 1030 nm as expected from the argumentation above. We take the experimental results as an indication that FCA and $N_{cr}$ are indeed wavelength-dependent quantities, and that the ablation mechanism is indeed linked to the high electron densities encountered during the pulses.

## VII. DISCUSSION

The temperature dependence of the linear absorption coefficient plays a crucial role for the dynamics of absorption. With pulses at 1030 nm, linear absorption is dominant except at room temperature, and two-photon absorption and impact ionization are of minor importance. However, if the electron-lattice coupling is slower than assumed in this article, as would be the case if implementing the three-temperature model, impact ionization would be a significant contributor to electron density for the case of irradiation at 1030 nm.

When choosing the two-temperature model, we are aware of the implied simplifications; however, more elaborate models would require an even larger number of uncertain material parameters. Already by applying the two-temperature model, many of the parameters used in our simulations are not easily accessible experimentally. The impact ionization coefficient, free-carrier absorption cross section, electron-lattice coupling, and several other parameters which need to be applied far from equilibrium situations have a significant influence on the simulation results. A shift in some of these material parameters may yield different electron generating dynamics and different ablation thresholds. We have presented in tables the values for these parameters that we have chosen to use in our simulations. We have motivated our choices in the main text. And in the main text, we have discussed how sensitive our main conclusions are to deviations in the parameters from the chosen values. There are several other quantifiable factors contributing to uncertainty in the comparison between experiments and simulations. The pulse duration can be measured with 10% accuracy. Simulating the ablation threshold using pulse duration of 3 ps ± 10% gives a variation in ablation threshold of up to 5%. The ablation threshold is determined to within 3% in the simulations, also contributing to discrepancy. The heat capacity in the simulations is taken as constant. Simulations with temperature varying heat capacity showed a discrepancy of 3%. In the simulations, we used the low intensity value for the reflectance. Measurements showed that the reflectance may vary by around 2% from the low intensity value for the fluencies encountered herein. Most of these error contributions can be assumed to be systematic (pulse duration, heat capacity, and reflectance), while the determination of ablation threshold poses a random error. As such, linear summation should be representative, giving a total error contribution of about 10%.

The simulated ablation thresholds deviate from the experimentally observed ablation thresholds by −60%, −43%, and +37% for 343, 515, and 1030 nm, respectively, when using screened Auger recombination. As we see, the under-estimation grows with decreasing wavelength. Two mechanisms could contribute towards this behavior. As already shown, by applying un-screened Auger recombination, most of the under-estimation is removed, and simulation results are

within −15% to +37% of the experimental values. Another mechanism which may contribute to the same trend is diffusion of carriers. Diffusion which is stronger than the simulated values would manifest itself as an increased ablation threshold compared to simulated values, and this effect would be most pronounced for the wavelengths with strong energy confinement, namely 515 and especially 343 nm.

Process temperatures well in excess of the temperatures investigated in this work are commonly used, for example, in the solar cell industry. These processes introduce little or only acceptable material degradation. As such, it is a realistic scenario to apply moderate substrate heating in order to better utilize expensive laser power and increase process throughput.

## VIII. CONCLUSION

Our experiments on ablation from silicon wafers at elevated temperatures, when applying ultrashort laser pulses with 3 ps pulse duration, show a temperature dependent behavior. We observe that the ablation thresholds at 515 and 1030 nm decrease by 35% and 43%, respectively, when substrate temperatures are increased from room temperature to 320 °C, while the ablation threshold at 343 nm remains constant with temperature.

In order to explain the observed trends, we have implemented a simulation model for solving the time-dependent two-temperature model for the interaction between silicon and ultrashort laser pulses. From these simulations, we see that the ablation is related to the critical electron density rather than to vaporization of the lattice. We have extracted the dynamic excess carrier generation from different mechanisms, such as linear and two-photon absorption, impact ionization, and Auger recombination. We have seen that the strongest carrier generating mechanism is linear absorption for all investigated cases, with the exception of irradiation at 1030 nm at 27 °C where two-photon absorption creates the majority of the carriers. Free-carrier absorption is the strongest energy absorption mechanism for irradiation at 1030 nm; however, this energy is lost through electron-lattice coupling, and does not directly contribute to the number density of conduction band electrons. We have discussed the consequences of choosing to apply the two-temperature model, rather than to apply the more elaborate three-temperature model. The two-temperature model assumes thermal equilibrium between optical and acoustic phonons, which certainly is a simplification for pulses as short as the ones encountered herein. Nevertheless, we are able to reproduce the observed temperature dependence in our simulations, and we are able to extract information about the dominating absorption mechanisms.

When applying elevated substrate temperatures in our simulations, we observe that the increase in linear absorption coefficient with temperature causes a lowering of the ablation threshold for irradiation at 515 and 1030 nm. With irradiation at 343 nm, no temperature dependence is observed, as a result of the temperature independence of the linear absorption coefficient at this wavelength. Best agreement between simulations and experiments is obtained when applying unscreened Auger recombination in our simulations.

We observe experimentally that ablation with 1030 nm pulses at 320 °C requires similar fluence as ablation by 515 nm pulses at 25 °C. This experimental result can only be explained by treating both the free-carrier absorption and the critical electron density as wavelength dependent quantities, as predicted by Drude free-electron theory, and in doing so accepting that the ablation is related to the high number densities of conduction band electrons encountered during the pulses. As only moderate substrate heating is required for significant lowering of the ablation threshold, these experimental results open the possibility of using substrate temperature in order to obtain efficient utilization of laser power when processing silicon with ultrashort laser pulses in the IR or visible wavelength range.

## ACKNOWLEDGMENTS

The authors gratefully acknowledge the valuable input received from Professor Aasmund Sudbø (University of Oslo) and Dr. Erik Marstein (Institute for Energy Technology) in forming the contents of this article. This work has been funded by the Research Council of Norway through the project "Thin and highly efficient silicon-based solar cells incorporating nanostructures," NFR Project No. 181884/S10.

[1]D. Bäuerle, *Laser Processing and Chemistry*, 3rd ed. (Springer, Berlin Heidelberg, 2000).
[2]B. C. Stuart, M. D. Feit, A. M. Rubenchik, B. W. Shore, and M. D. Perry, Phys. Rev. Lett. **74**, 2248–2252 (1995).
[3]B. C. Stuart, M. D. Feit, S. Herman, A. M. Rubenchik, B. W. Shore, and M. D. Perry, J. Opt. Soc. Am. B **13**, 459 (1996).
[4]P. Engelhart, S. Hermann, T. Neubert, H. Plagwitz, R. Grischke, U. Klug, A. Schoonderbeek, U. Stute, and R. Brendel, Prog. Photovoltaics **15**, 521 (2007).
[5]J. Hermann, M. Benfarah, G. Coustillier, S. Bruneau, E. Axente, J.-F. Guillemoles, M. Sentis, P. Alloncle, and T. Itina, Appl. Surf. Sci. **252**, 4814–4818 (2006).
[6]M. Schulz-Ruhtenberg, D. Trusheim, J. Das, S. Krantz, and J. Wieduwilt, Energy Procedia **8**, 614–619 (2011).
[7]N. Bulgakova, R. Stoian, A. Rosenfeld, I. Hertel, and E. Campbell, in *Laser Ablation and Its Applications*, 1st ed., edited by C. Phipps (Springer Science+Business Media LLC, Boston, MA, 2010), pp. 17–36.
[8]H. S. Sim, S. H. Lee, and K. G. Kang, Microsyst. Technol. **14**, 1439–1446 (2008).
[9]S. S. Mao, X. L. Mao, R. Greif, and R. E. Russo, Appl. Surf. Sci. **127–129**, 206–211 (1998).
[10]B. Christensen, K. Vestentoft, and P. Balling, Appl. Surf. Sci. **253**, 6347–6352 (2007).
[11]J. M. Liu, Opt. Lett. **7**, 196–198 (1982).
[12]M. C. Downer and C. V. Shank, Phys. Rev. Lett. **56**, 761–764 (1986).
[13]H. M. van Driel, Phys. Rev. B **35**, 8166–8176 (1987).
[14]J. Chen, D. Tzou, and J. Beraun, Int. J. Heat Mass Transfer **48**, 501–509 (2005).
[15]T. Sjodin, H. Petek, and H.-L. Dai, Phys. Rev. Lett. **81**, 5664–5667 (1998).
[16]T. Y. Choi and C. P. Grigoropoulos, J. Appl. Phys. **92**, 4918 (2002).
[17]L. A. Falkovsky and E. G. Mishchenko, J. Exp. Theor. Phys. **88**, 84–88 (1999).
[18]D. von der Linde, J. Kuhl, and H. Klingenberg, Phys. Rev. Lett. **44**, 1505–1508 (1980).
[19]*Microscale Energy Transport*, edited by C.-L. Tien, A. Majumdar, and F. M. Gerner (Taylor & Francis, Washington, D.C., 1998).
[20]E. J. Yoffa, Phys. Rev. B **21**, 2415 (1980).
[21]E. Lioudakis, A. G. Nassiopoulou, and A. Othonos, Semicond. Sci. Technol. **21**, 1041–1046 (2006).
[22]M. V. Fischetti and S. E. Laux, Phys. Rev. B **38**, 9721 (1988).
[23]Y. Kamakura, H. Mizuno, M. Yamaji, M. Morifuji, K. Taniguchi, C. Hamaguchi, T. Kunikiyo, and M. Takenaka, J. Appl. Phys. **75**, 3500 (1994).

[24]G. E. Jellison, Appl. Phys. Lett. **41**, 594 (1982).
[25]D. Agassi, J. Appl. Phys. **55**, 4376–4383 (1984).
[26]C. K. Ong, H. S. Tan, and E. H. Sin, Mater. Sci. Eng. **79**, 79–85 (1986).
[27]G. E. Jellison, Appl. Phys. Lett. **41**, 180 (1982).
[28]T. F. Boggess, K. M. Bohnert, K. Mansour, S. C. Moss, I. W. Boyd, and A. L. Smirl, IEEE J. Quantum Electron. **22**, 360–368 (1986).
[29]M. Sheik-Bahae and M. P. Hasselbeck, in *Handbook of Optics, Volume IV—Optical Properties of Materials, Nonlinear Optics, Quantum Optics*, edited by M. Bass, G. Li, and E. V. Stryland (McGraw-Hill, New York, 2010).
[30]N. Ashcroft and N. Mermin, *Solid State Physics*, 1st ed. (Thomson Learning, 1976).
[31]J. Reitz, F. Milford, and R. Christy, *Foundations of Electromagnetic Theory*, 4th ed. (Addison-Wesley, 1993).
[32]E. H. Sin, C. K. Ong, and H. S. Tan, Phys. Status Solidi A **85**, 199–204 (1984).

# PAPER VI

Jostein Thorstensen, Ragnhild Sæterli and Sean Erik Foss, "Laser ablation mechanisms in thin silicon nitride films on a silicon substrate," *submitted to IEEE Journal of Photovoltaics*, April 2013.

# PAPER VII

Jostein Thorstensen and Sean Erik Foss, "New approach for the ablation of dielectrics from silicon using long wavelength lasers," *submitted to Energy Procedia,* March 2013.

Available online at www.sciencedirect.com

SciVerse ScienceDirect

Energy Procedia 00 (2013) 000–000

Energy Procedia

www.elsevier.com/locate/procedia

SiliconPV: March 25-27, 2013, Hamelin, Germany

# New approach for the ablation of dielectrics from silicon using long wavelength lasers

Jostein Thorstensen*[a,b] and Sean Erik Foss[a]

[a]*Institute for Energy Technology, P.O. Box 40, 2027 Kjeller, Norway*
[b]*University of Oslo, Department of Physics, P.O. Box 1048 Blindern, 0316 Oslo, Norway*

**Abstract**

Laser ablation of dielectrics from silicon substrates represents a useful technique for e.g. the creation of local contacts. However, these dielectrics are transparent at the laser wavelengths normally employed for silicon solar cell processing, i.e. the first, second and third harmonics of solid state lasers (1064, 532 and 355 nm). As a result of this, the ablation is indirect, and follows from energy deposition in the silicon rather than in the dielectric. This mechanism introduces defects in the silicon substrate, an effect which is detrimental to solar cell performance. Attempts have been made to limit the extent of the laser damage, by going to shorter wavelengths and shorter pulse durations.
In this work, we suggest an alternative route to low-damage ablation of dielectrics by application of long wavelength laser pulses from e.g. $CO_2$-lasers. At wavelengths above approx. 8 µm, we find absorption bands in many of the dielectrics applied in solar cells. Simulations show that it may be possible to keep the silicon temperature below melting temperature, while reaching vaporization temperature in the dielectric. Experiments using laser pulses at 9.3 µm with a duration of approx. 100 ns show, however, that the silicon substrate experiences melting. We conclude that even shorter pulses must be applied for the method to be successful.


Selection and/or peer-review under responsibility of the scientific committee of the SiliconPV 2013 conference

*Keywords:* Laser ablation; long laser wavelengths

## 1. Introduction

In processing of silicon solar cells, the local removal of dielectric layers is beneficial for several processes [1–3]. Lasers have been suggested as a possible tool for this local removal, as lithography and masking processes may be incompatible with industrial scale processing. However, laser damage is often

* Corresponding author. Tel.: +47 63806445; fax: +47 63812905.
*E-mail address:* Jostein.thorstensen@gmail.com.

observed as a reduction of lifetime in lowly doped silicon, or it can be observed as an increase in the dark saturation current density if processing in emitters [1,4]. This laser damage is a result of laser energy deposition in the silicon. The approach up until now has been to go to shorter pulse durations and wavelengths, in order to either confine the laser energy and damage to a shallow layer in the silicon, or to obtain (non-linear) absorption in the dielectric layers, which normally are transparent at visible and near-infra-red wavelengths due to their high band-gap energy. The problem with going to short laser wavelengths and ultrashort laser pulses is that the silicon will also be highly absorbing in this situation, meaning that there will always be an inherent mechanism present for energy deposition into the silicon. In this article, we propose a new approach for obtaining low damage ablation of dielectric layers from silicon.

We seek a situation where we not only get energy deposition in the dielectric, as will be the case in the situation described above, but where the silicon in addition is transparent to the laser light. In such a situation, once the dielectric is removed, we will get no more laser energy deposition, and one could potentially obtain a much more stable process. Our approach is based on the application of short-pulsed, long wavelength lasers, operating at wavelengths above 8 μm. At these wavelengths, intrinsic silicon is nearly transparent at room temperature, while many dielectrics have absorption bands at these wavelengths. This behaviour opens for the possibility of directly depositing the laser energy into the dielectric, while keeping the silicon at a much lower temperature. We simulate the temperature evolution during such a laser pulse, and compare the results with experiments performed using a $CO_2$-laser at 9.3 μm and a pulse duration of 100 ns.

## 2. Simulations

We apply a partial differential equation solver with one spatial dimension in order to solve the heat equation for our system. The system consists of a stack structure with a dielectric on top of a silicon slab. The silicon substrate is 100 μm thick, and the dielectric is 100 nm thick. We assume that ablation of the dielectric is obtained when the dielectric reaches vaporization temperature, and we shall abort the simulations if the silicon reaches melting temperature, as the recrystallization is assumed to introduce defects in the silicon, being an undesired situation. The heat equation is given by [5]:

$$C_p \frac{\partial T}{\partial t} = \frac{\partial}{\partial x}\left(\kappa \frac{\partial T}{\partial x}\right) + \alpha I(1-R)\ . \qquad (1)$$

Here, $C_p$ is the heat capacity, modified to include the enthalpy of phase change, $\kappa$ is the heat conductivity, $\alpha$ is the optical absorption coefficient. $I$ is the optical fluence, $R$ is the reflectivity and $\alpha I(1-R)$ is the energy input from the laser. At the boundary between dielectric and silicon, we apply extra thermal interface resistance, $R_{int}$, as reported by Huang *et al.* [6] and Kuo *et al.* [7]. This resistance is related to the mismatch between phonon modes in different materials, and will delay heat transfer. Material parameters are taken from the literature and are shown in table 1 and table 2. $T_v$ indicates the vaporization temperature.

Table 1. Material parameters for $SiO_x$ and $SiN_x$.

| Parameter | $SiO_x$ | $SiN_x$ | Unit | Ref |
|---|---|---|---|---|
| $R_{int}$ | $2.4 \times 10^{-4}$ | $3.7 \times 10^{-4}$ | $cm^2K/W$ | [6] |
| $T_v$ | 3223 | 2100 | K | [8,9] |
| $C_p$ | 3 | 1.80 | $J/cm^3$ K | [10,11] |
| $\kappa$ | 0.0123 | 0.0107 | W / cm K | [6] |

Table 2. Material parameters for Si.

| Parameter | Value | Unit | Ref |
|---|---|---|---|
| $C_{Si,solid}$ | 2.24 | J/cm$^3$ K | [12] |
| $C_{Si,liquid}$ | 2.33 | J/cm$^3$ K | [13] |
| $\kappa_{Si,solid}$ | $1.521 \times 10^3 T^{-1.226}$ $(300 < T < 1200)$<br>$8.96 \times T^{-0.502}$ $(1200 < T < 1683)$ | W / cm K | [12] |
| $\kappa_{Si,liquid}$ | 0.62 | W / cm K | [13] |

The optical absorption coefficient $\alpha$ is of course of outmost importance for the outcome of the simulations, however, this term is not straightforward in these simulations. For energy deposition in the dielectrics, absorption coefficients from FTIR measurements are used, however, we need an expression for $\alpha$ in silicon. As we are applying long wavelength irradiation, band-to-band absorption is prohibited, and we are left with free-carrier absorption (FCA) and absorption by defect states $\alpha = \alpha_{defect} + \alpha_{fca}$. $\alpha_{defect}$ is obtained from FTIR measurements. $\alpha_{fca}$, on the other hand, is more difficult to quantify. $\alpha_{fca}$ at room temperature is given by the expression $\alpha_{fca} = 2 \times 10^{-18} N_{doping} \lambda^2$ [14], where $N_{doping}$ is the background doping level. More fundamentally, FCA is expected to have an absorption coefficient following the trend [14]:

$$\alpha_{fca} \propto \frac{N}{\mu} \lambda^2, \tag{2}$$

meaning that $\alpha_{fca}$ is dependent on the mobility $\mu$, number density of free electrons $N$, and wavelength of the laser irradiation, $\lambda$. As $\mu$ and $N$ are temperature dependent, so is $\alpha_{fca}$. The temperature dependence of $N$ is given by [15]:

$$N(T) = N_{doping} + N_i(300) \times \frac{N_i(T)}{N_i(300)} = N_{doping} + N_i(300) \times \frac{T^{\frac{3}{2}} \exp\left(-\frac{E_g(T)}{2k_B T}\right)}{300^{\frac{3}{2}} \exp\left(-\frac{E_g(300)}{2k_B \times 300}\right)}, \tag{3}$$

where $N_i(300)$ is the intrinsic carrier concentration in silicon at 300 K, $E_g(T)$ is the temperature dependent band-gap energy and $k_B$ is the Boltzmann constant. $E_g(T)$ is given by [16]:

$$E_g(T) = E_g(0) - \frac{BT^2}{C+T}, \tag{4}$$

in units of eV, where $E_g(0) = 1.155$ eV, $B = 4.73 \times 10^{-4}$ eV/K and $C = 635$ K are fitting parameters. The electron mobility $\mu$ is given by [17]:

$$\mu_e(N,T) = 88 T_n^{-0.57} + \frac{7.4 \times 10^8 T^{-2.33}}{1 + \left(N / \left(1.26 \times 10^{17} T_n^{2.4}\right)\right) \times 0.88 T_n^{-0.146}} \tag{5}$$

where $T_n$ is T/300. Combining these expressions, we can write $\alpha_{fca}$ as

$$\alpha_{fca}(N,T) = \alpha_{fca}(10^{16}, 300) \times \frac{N(T)}{10^{16}} \times \frac{\mu\left(10^{16}, 300\right)}{\mu(N,T)} \tag{6}$$

When the silicon is cold, $\alpha_{fca}$ is fairly small, and the substrate is fairly transparent. When the temperature rises, however, $\alpha_{fca}$ increases significantly, meaning that we have a mechanism for thermal runaway in silicon, where heated silicon will absorb stronger, confine the laser energy to a smaller volume and hence grow even hotter. It should be noted that $\mu$ and $\alpha_{fca}$ have not been measured at

temperatures close to the melting temperature of silicon, where the FCA is strongest. As such, the values for $\alpha_{fca}$ are uncertain, and introduces a significant source of error in the simulations.

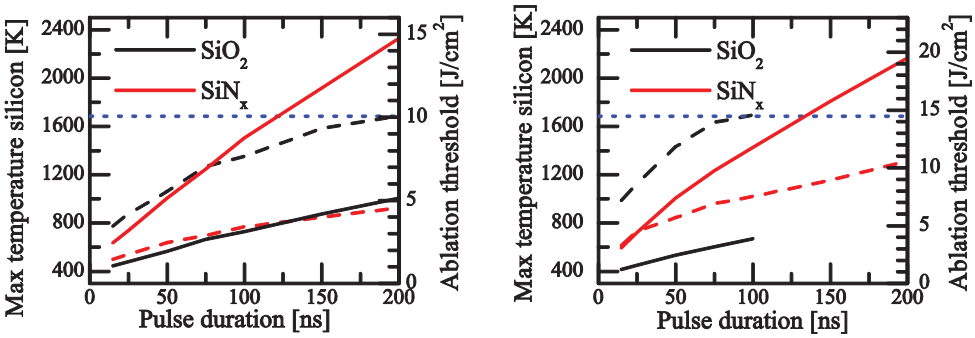


Fig. 1. (Left) Ablation threshold for dielectric from silicon using literature values (Solid lines). Also shown is the maximum temperature reached in the silicon substrate (dashed lines). (Right) The same values, but with higher thermal conductivity in the dielectric, and thermal interface resistance removed. Also shown is the melting temperature of silicon (dotted blue lines).

Fig. 1 (left) shows the simulated ablation threshold (solid lines) and the maximum temperature of the silicon substrate (dashed lines) using literature values. We see that the substrate temperature decreases with decreasing pulse duration, a sign of reduced heat transfer from the dielectric. Reducing the pulse duration is therefore a way to reach ablation with substrate temperatures well below melting temperature. Fig. 1 (right) shows the same simulations, but with the thermal conductivity, $\kappa$, in the dielectric increased by a factor 10 and the thermal interface resistance removed, constituting a pessimistic scenario. Here, significantly shorter pulses must be applied in order to keep the silicon from melting.

## 3. Experimental

We measure the infrared absorption coefficient of several dielectrics commonly used in solar cell processing, by means of Fourier-transform infrared spectroscopy (FTIR). The dielectrics are deposited by plasma-enhanced chemical vapor deposition (PECVD). The results are shown in Fig 2. We see that $SiO_x$, $SiN_x$ and $SiO_xN_y$ have significant absorption at around 9.3 µm, suitable for the $CO_2$-laser, while $AlO_x$ shows absorption only at longer wavelengths.

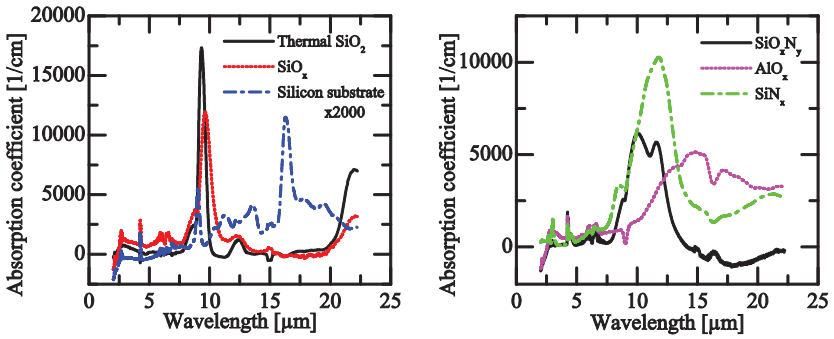


Fig. 2. Absorption coefficient in various dielectrics as measured by FTIR. All are deposited by PECVD, with the exception of the thermal $SiO_2$. Also shown is the absorption in the silicon substrate (x2000). The absorption bands are seen from around 8 µm.

We perform experiments on ablation of thermal $SiO_2$, PECVD - $SiO_x$, $SiN_x$ and $SiO_xN_y$ using a $CO_2$-laser at 9.3 µm and pulse duration of 100 ns. The experiments, however, show expulsion of the silicon, shown in fig. 3, and we conclude that the substrate has melted, indicating that the applied pulses are too long for the desired behavior. This also means that the heat conduction from the dielectric or the absorption in the silicon substrate is significantly higher than what we have simulated. We also perform ablation experiments on bare silicon (without dielectric cover), and we find that in this situation, the ablation threshold is very much higher than that obtained with a dielectric covering the silicon. This is taken as an indication that laser energy deposition in cold silicon is indeed very slow, and that the silicon is heated by heat conduction from the dielectric. The heated silicon will thereafter absorb more strongly, leading to melting of the silicon.

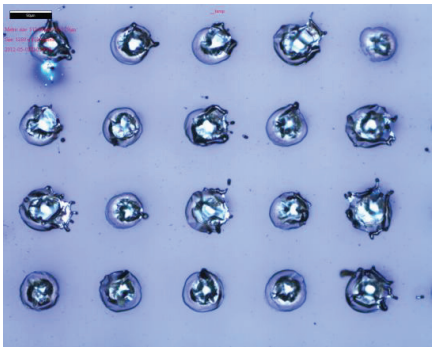

Fig. 3. Process result from the laser ablation of $SiO_x$ using a laser wavelength of 9.3 µm and 100 ns pulse duration. Expulsion of silicon is clearly seen, indicating that the silicon has reached the melting temperature.

## 4. Discussion

We have found that the simulations fail to predict the ablation behavior of dielectrics from silicon when applying 100 ns pulses at 9.3 µm wavelength. We have already noted that this means that either the heat transfer from the dielectric is higher than expected, or the absorption in silicon is stronger. It could, however, also mean that some of our assumptions are incorrect. Firstly, we assume that ablation of the dielectric occurs when the surface of the dielectric reaches vaporization temperature. With some of the dielectric at vaporization temperature, the vapor pressure would expel the remaining dielectric. This description may not necessarily be correct. Secondly, and more importantly, we assume that $R_{int}$ is temperature independent. This need not be the case, as $R_{int}$ represents thermal resistance caused by mismatch of phonon modes. With temperature increase and the following melting of the dielectric, this resistance must be expected to change.

## 5. Conclusion

We suggest using long wavelength laser irradiation for removal of dielectric layers from silicon wafers, as many dielectrics have absorption bands at wavelengths above 8 µm, and as silicon is transparent at these wavelengths. Simulations show that there is a possibility of reaching vaporization temperatures in the dielectric while keeping the substrate below melting temperatures if using short enough pulses. Experiments, however, show that substrate melting is observed for pulses as short as 100 ns, indicating that the heat transfer from the dielectric or absorption in the substrate is significantly higher

than what we have simulated. As such, even shorter pulses must be applied for the method to be successful.

## Acknowledgements

This work has been funded by the Research Council of Norway through the project "Thin and highly efficient silicon-based solar cells incorporating nanostructures", NFR Project No. 181884/S10.

## References

[1] P. Engelhart, S. Hermann, T. Neubert, H. Plagwitz, R. Grischke, R. Meyer, et al., Laser Ablation of SiO2 for Locally Contacted Si Solar Cells With Ultra-short Pulses, Progress in Photovoltaics: Research and Applications. 15 (2007) 521–527.

[2] K. Mangersnes, Back-contact back-junction silicon solar cells, University of Oslo, 2010.

[3] A. Knorz, M. Peters, A. Grohe, C. Harmel, R. Preu, Selective Laser Ablation of SiNx Layers on Textured Surfaces for Low Temperature Front Side Metallizations, Progress in Photovoltaics: Research and Applications. 17 (2009) 127–136.

[4] M. Ametowobla, Characterization of a Laser Doping Process for Crystalline Silicon Solar Cells, Universität Stuttgart, 2010.

[5] D. Bäuerle, Laser Processing and Chemistry, 3rd ed., Springer, Berlin Heidelberg, 2000.

[6] S. Huang, X. Ruan, X. Fu, H. Yang, Measurement of the thermal transport properties of dielectric thin films using the micro-Raman method, Journal of Zhejiang University SCIENCE A. 10 (2009) 7–16.

[7] B. Kuo, J. Li, A. Schmid, Thermal conductivity and interface thermal resistance of Si film on Si substrate determined by photothermal displacement interferometry, Applied Physics A. 55 (1992) 289–296.

[8] W.M. Haynes, ed., Physical Constants of Inorganic Compounds, in: CRC Handbook of Chemistry and Physics, 92nd ed., CRC Press/Taylor and Francis, Boca Raton, FL, 2012.

[9] Y. Cerenius, Melting-Temperature Measurements on, Journal of the American Ceramic Society. 82 (1999) 380–386.

[10] C.L. Yaws, Yaws' Handbook of Thermodynamic Properties for Hydrocarbons and Chemicals, Knovel, 2009.

[11] A. Jain, K.E. Goodson, Measurement of the Thermal Conductivity and Heat Capacity of Freestanding Shape Memory Thin Films Using the 3ω Method, Journal of Heat Transfer. 130 (2008) 102402.

[12] C.K. Ong, H.S. Tan, E.H. Sin, Calculations of Melting Threshold energies of crystalline and amorphous materials due to pulsed-laser irradiation, Materials Science and Engineering. 76 (1986) 79 – 85.

[13] H. Kobatake, H. Fukuyama, I. Minato, T. Tsukada, S. Awaji, Noncontact measurement of thermal conductivity of liquid silicon in a static magnetic field, Applied Physics Letters. 90 (2007) 094102.

[14] D.K. Schroder, R.N. Thomas, J.C. Swartz, Free Carrier Absorption in Silicon, IEEE Transactions on Electron Devices. 25 (1978) 254–261.

[15] J. Nelson, The Physics of Solar Cells, Imperial College Press, UK, 2003.

[16] E.H. Sin, C.K. Ong, H.S. Tan, Temperature Dependence of Interband Optical Absorption of Silicon at 1152, 1064, 750 and 694 nm, Physica Status Solidi (a). 199 (1984) 199–204.

[17] N.D. Arora, J.R. Hauser, D.J. Roulston, Electron and Hole Mobilities in Silicon as a Function of Concentration and Temperature, IEEE Transactions on Electron Devices. ED-29 (1982) 292–295.

# PAPER VIII

Jostein Thorstensen and Sean Erik Foss, "Investigation of depth of laser damage to silicon as function of wavelength and pulse duration," *accepted for publication in Energy Procedia,* March 2013.

Available online at www.sciencedirect.com

SciVerse ScienceDirect

Energy Procedia 00 (2013) 000–000

Energy Procedia

www.elsevier.com/locate/procedia

SiliconPV: March 25-27, 2013, Hamelin, Germany

# Investigation of depth of laser damage to silicon as function of wavelength and pulse duration

Jostein Thorstensen*[a,b] and Sean Erik Foss[a]

[a]*Institute for Energy Technology, P.O. Box 40, 2027 Kjeller, Norway*
[b]*University of Oslo, Department of Physics, P.O. Box 1048 Blindern, 0316 Oslo, Norway*

**Abstract**

When quantifying laser damage in silicon, two key parameters are of importance, namely the depth of the laser damaged region and the minority carrier lifetime in the laser processed region. In this paper, we investigate the depth of the electrically active laser damage as function of laser wavelength and laser pulse duration. By etch-back experiments, we find that the laser damage from picosecond laser pulses is confined to a considerably shallower region than what is the case for nanosecond pulses. This is as expected due to the longer available times for heat conduction experienced in the latter case. However, the depth of damage is also much shallower than what the linear optical absorption coefficient would suggest, pointing towards non-linear optical confinement. We also develop an analytical expression for the effective minority carrier lifetime measured on a wafer with a laser damaged region, and from this expression, we are able to give an estimate on the lifetime in the laser damaged region. Based on these findings, we develop an optimized laser process.
Using a wavelength of 515 nm and a pulse duration of 3 ps, an effective lifetime of 1.8 ms is completely recovered after removal of just 240 nm of silicon from the wafer surface. The lifetime in the laser damaged region is in this case estimated to be on the order of 1 ns.


Selection and/or peer-review under responsibility of the scientific committee of the SiliconPV 2013 conference

*Keywords:* Laser ablation; laser damage; lifetime

## 1. Introduction

In laser processing for silicon solar cells, the laser induced damage is a crucial factor. Both the electrical activity of the damage, in the form of reduction in minority carrier lifetime (from here:

* Corresponding author. Tel.: +47 63806445; fax: +47 63812905.
*E-mail address:* Jostein.thorstensen@gmail.com.

lifetime), and the distribution of the damage are of importance. While it is often stated that the depth of the laser induced damage or heat affected zone is reduced when using ultrashort lasers, this depth is rarely measured. In this paper, we present a comparison of the depth of laser induced damage encountered when using nanosecond and picosecond pulses. We ablate silicon nitride ($SiN_x$) from a silicon substrate, etch away a controlled silicon thickness, and measure the effective lifetime of the wafer as function of removed silicon thickness. Furthermore, we develop an analytical model for the effective lifetime measured on a wafer with a laser damaged region at one surface. From the model and the measured depth of the laser damage, an estimate on the lifetime in the laser damaged area is given.

## 2. Theory

### *2.1. Depth of laser damage*

The penetration depth of the laser energy, $l_{pen}$, is often assumed to be [1]

$$l_{pen} \approx l_{opt} + l_{diff} = 1/\alpha + \sqrt{\tau D_{th}}, \quad (1)$$

where $l_{opt} = 1/\alpha$ is the optical penetration depth, $\alpha$ is the optical absorption coefficient, $\tau$ is the pulse duration and $D_{th}$ is the thermal diffusion coefficient. $l_{opt}$ describes the depth at which the laser energy is actually deposited, while $l_{diff}$ is the diffusion term, describing how far the energy may diffuse during the pulse.

Some comments must be made to this model. Firstly, α is very often temperature dependent, and the temperature of the substrate increases during laser processing. As such, an effective optical penetration depth, $l_{opt,eff}$ should be applied. In order to correspond with the definition of $l_{opt}$, $l_{opt,eff}$ should be defined as the depth after which 1/e of the incoming laser energy remains. As $\alpha$ normally increases with increasing temperature, $l_{opt,eff}$ is normally smaller than $l_{opt}$. Furthermore, the expression $l_{diff} = \sqrt{\tau D_{th}}$ assumes that the heated material is removed within the duration of the pulse. While this may hold true for laser processing with long pulses, where much of the heated (molten) material is expelled during the laser pulse, it may not be true when applying ultrashort pulses. In this case, the material may be removed some time after the pulse [2], giving a larger diffusion depth than expected from the expression above. Furthermore, the value for $D_{th}$ may deviate from its steady-state value, as the electron gas is strongly heated when applying ultrashort laser pulses. As such, the value for the penetration depth, $l_{pen}$ should be treated with caution, and the link between $l_{pen}$ and the depth of laser induced damage likewise.

Engelhart *et al.* [3] have performed an experiment similar to ours, and report laser damage at 2, 3 and 25 µm, for 30 nanosecond pulses at 355, 532 and 1064 nm, respectively. With $l_{opt}$ of 10 nm, 0.7 µm and ~300 µm for the three wavelengths, and $l_{diff}$ of about 1.5 µm, this result shows that the laser damage in this case is situated deeper than $l_{diff}$, but may be situated shallower or deeper than both $l_{pen}$ and $l_{opt}$, depending on which of the above mentioned processes are most dominant. At 355 nm, the depth of damage must be dominated by diffusion, as the optical penetration depth is very small. Hence, $l_{diff} \simeq 2$ µm for this pulse duration (eq. (1) gives $l_{diff} = 1.5$ µm using $D_{th}$ from [4]). At 1064 nm, the depth of damage must be dominated by the optical penetration depth $l_{opt,eff}$. With $l_{opt}$~300 µm at this wavelength, we see that $l_{opt,eff}$ is much smaller than $l_{opt}$ at this wavelength as discussed above.

Some general trends can be expected when going to shorter pulses. With very short laser pulses, heat transport is strongly reduced. In addition, α increases with increasing optical intensity, as a result of non-linear processes. These two factors both contribute to stronger confinement of the laser energy when applying ultrashort laser pulses.

### 2.2. Lifetime in laser damaged region

We are also interested in estimating the lifetime encountered in the laser damaged region, and need an expression for the effective lifetime measured in a wafer with laser damage near one surface. Applying the geometry shown in Fig. 1, we investigate the minority carrier distribution in the laser damaged region. We assume that photogeneration occurs only in the undamaged bulk of the wafer, and assume that $S_2$ is small compared to the recombination taking place in the laser damaged region. We use the continuity equation

$$\frac{\partial n}{\partial t} = -U - \frac{\partial J}{\partial x} = \frac{n}{\tau} - D_n \frac{\partial^2 n}{\partial x^2}. \quad (2)$$

where $U$ is the recombination, $J$ is the electron current, $D_n$ is the electron diffusion coefficient, $n$ is the electron density and $\tau$ is the electron lifetime. The stationary solution gives

$$\frac{n}{\tau} = D_n \frac{\partial^2 n}{\partial x^2}. \quad (3)$$

We apply the boundary condition of zero recombination current across $S_2$. The carrier density in the laser damaged region becomes

$$n(x) = A \cosh\left(\frac{x-(d+w)}{\sqrt{D_n \tau_{laser}}}\right), \quad (4)$$

with $S_2$ at $x = d + w$ where $d + w$ is the total wafer thickness, and $w$ is the width of the laser damaged region, assumed to be constant over the wafer. The total recombination in the laser damaged region can be found by integrating over the laser damaged region, $x \in [d, d + w]$:

$$U_{tot} = \int_d^{d+w} \frac{n(x)}{\tau_{laser}} dx = A \sqrt{\frac{D_n}{\tau_{laser}}} \sinh\left(\frac{w}{\sqrt{D_n \tau_{laser}}}\right). \quad (5)$$

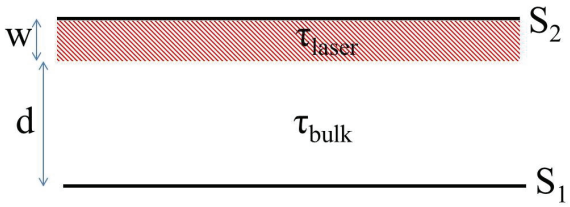


Fig. 1. Wafer with laser damaged region. Thicknesses, lifetimes and surface recombination velocities are indicated.

Inserting a virtual boundary between bulk and laser damaged region ($x = d$), a surface recombination velocity (SRV) can be defined as

$$S_{laser} \equiv \frac{U_{tot}}{n(x=d)} = \sqrt{\frac{D_{el}}{\tau_{laser}}} \tanh\left(\frac{w}{\sqrt{D_n \tau_{laser}}}\right) \quad (6)$$

where $n(x = d)$ is the electron concentration at $x = d$. We see that the effective SRV from the laser damage depends on both $w$ and $\tau_{laser}$. For $w \gg \sqrt{D_n \tau_{laser}}$, i.e. laser damage much deeper than the diffusion length, the recombination saturates, and $S_{laser} \approx \sqrt{D_n/\tau_{laser}}$ is independent of $w$. For a powerful analysis tool, the expression in eq. (6) can be combined with expressions by Sproul [5] for the effective lifetime and the surface lifetime:

$$\frac{1}{\tau_{eff}} = \frac{1}{\tau_b} + \frac{1}{\tau_s} = \frac{1}{\tau_{bulk}} + \alpha_0^2 D_n \,, \tag{7}$$

where $\alpha_0$ is the smallest eigenvalue solution of the equation

$$\tan(\alpha_0 w) = (S_{laser} + S_2)/(\alpha_0 D_n - \frac{S_{laser} S_2}{\alpha_0 D_{el}}) \,. \tag{8}$$

Here, we apply eq. (6) for $S_{laser}$, in order to obtain the effective lifetime of the laser damaged structure.

## 3. Experimental

We deposit a 75 nm thick a-$SiN_x$:H ($SiN_x$) film by plasma-enhanced chemical vapor deposition (PECVD) on polished silicon wafers. The $SiN_x$ has a refractive index of around 2.05 at a wavelength of 633 nm. We ablate the $SiN_x$ by applying non-overlapping laser pulses at 1030, 515 and 343 nm and a pulse duration of 3 ps using a peak fluence of 0.86, 1.2 and 2.1 J/cm$^2$ at 1030, 515 and 343 nm, respectively, and at 532 nm and 100 ns pulse duration using a peak fluence of around 20 J/cm$^2$. The remaining $SiN_x$ is removed in an HF dip, and the samples are etched in a concentrated (47 %) KOH solution at 85 °C, showing an etch rate of approx. 1 µm/min. The etch depth is measured by gravimetry, assuming uniform material removal over the wafer. The accuracy of the measurement is +/- 0.2 mg, corresponding to approx. 20 nm etch depth. The samples are then passivated by amorphous silicon (a-Si), ensuring very low SRV, and the effective lifetime of the samples is measured by photoluminescence imaging (PL) using a LIS-R1 setup from BTimaging. The lifetime measured in the laser processed areas is normalized to the effective lifetime measured in damage-free areas.

As defects or surface roughness may act as seeds for etching, thereby increasing the local etch rate, we analyze the shape of the laser spots before and after etching by atomic force microscopy (AFM). If the laser spot gets deeper by etching, there would be a preference for etching in the spots, and hence, the depth of damage must be corrected correspondingly.

## 4. Results

### *4.1. Depth of laser damage*

When etching the wafers, the lifetime in the laser treated areas is gradually restored, at some point reaching the 1.8 ms seen outside of the laser treated areas. AFM analysis shows that the shape of the laser spot remains constant with etching, ruling out the possibility of preferential etching in the spots.

The results of the etch-back experiments are shown in Fig. 2 (left), showing that the depth of the laser damage using ultrashort pulses is in the range of 70 – 130 nm for 343 nm (between the last measurement point showing lifetime degradation and the first measurement point showing complete recovery of the lifetime), 120 – 240 nm using 515 nm and below 210 nm using 1030 nm laser wavelength (we unfortunately don't have any measurements showing lifetime degradation for this laser wavelength and pulse duration). Using long laser pulses at 532 nm, the damage is situated much deeper, in the range of 1.8 – 2.7 µm. This depth corresponds approximately to $l_{diff}$.

It should be noted that also on non-laser treated reference samples, surface-near damage was observed as reductions in effective lifetime down to a depth of approx. 70 nm. This is attributed to ion bombardment damage from the PECVD-process. However, this ion bombardment damage is less pronounced than the laser damage, making it easy to extract the contributions from laser induced damage.

It is interesting to note the difference between long and short pulses at wavelengths at 515 nm laser wavelength. The 3 ps, 515 nm pulse results in a much more shallow damage than at the same wavelength

using long pulses, confined to within 240 nm of the wafer surface. This is a result of the elimination of thermal diffusion (which at a pulse duration of 3 ps would correspond to around 20 nm). Comparing with measurements by Engelhart *et al.*, the same reduction is also seen in the UV, where the depth of damage using long pulses was dominated by thermal diffusion. Using 3 ps, 343 nm pulses, thermal diffusion is eliminated, and the depth of damage is much smaller. At 1064 nm, the depth of damage using nanosecond-pulses [3] was around 25 µm, and dominated by the optical penetration depth. Using 3 ps, 1030 nm pulses, we see no reduction in lifetime even at 210 nm from the surface, indicating that the optical penetration depth must have been dramatically reduced (by two orders of magnitude!), as a result of non-linear absorption mechanisms using ultrashort pulses. In combination, the comparison between depth of damage using nanosecond and picosecond lasers at three wavelengths shows that both the optical penetration depth and the thermal diffusion depth are decreased using ultrashort laser pulses.

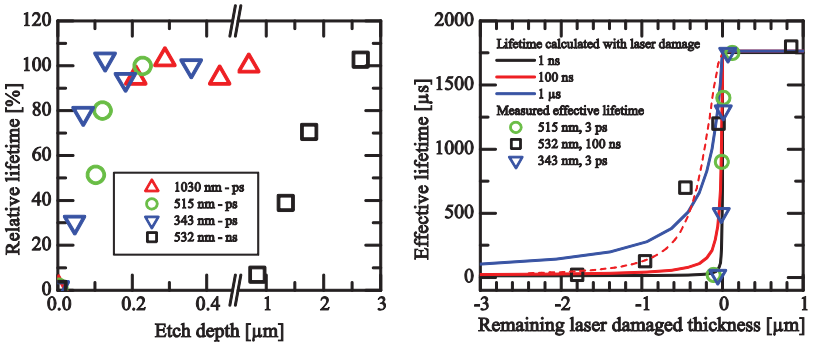


Fig. 2. (Left) Relative lifetime measured as function of etch depth using four different lasers. (Right) Modeled effective lifetime (solid lines) assuming three different values for $\tau_{laser}$ and measured effective lifetime (symbols) as function of depth of laser damage. Also shown is a calculation of effective lifetime taking into account the finite area coverage and geometry of the laser damage (dotted line).

### *4.2. Lifetime in laser damaged region*

We plot the modeled effective lifetime as extracted using eqs. (6-8) as function of the remaining laser damage, shown in Fig. 2 (right) as solid lines. The measured effective lifetime is shifted along the x-axis for best fit, shown as symbols. We see that for the 515 nm, 3 ps sample, a fairly good fit is found if inserting a lifetime in the laser damaged region of 1 ns. However, as we only have a limited number of experimental values, a smaller lifetime in the laser damaged region would give an equally good fit.

For the 532 nm, 100 ns sample, however, the fit is not as good, indicating that other effects are taking place. One effect could be the geometry of the laser damage. We have applied spots in a square pattern, with 30 µm pitch. Using long laser pulses, it is not unreasonable to assume that the molten volume will be deepest in the middle of the laser spot. Assuming that the laser damaged volume has the shape of a paraboloid with depth 1.8 µm (estimated from the etch depth showing recovery of the effective lifetime), the area fraction of laser damage will decrease as we etch into the wafer, decreasing the effective SRV. With a width of the paraboloid at the wafer surface of 30 µm, we can calculate the fill factor of the laser damage as function of etch depth. We can then apply Fischer's formula for effective SRV [6]

$$S_{eff} = \frac{D_{el}}{W}\left(\frac{p}{2W\sqrt{\pi f}}\arctan\left(\frac{2W}{p}\sqrt{\frac{\pi}{f}}\right) - \exp\left(-\frac{W}{p}\right) + \frac{D_{el}}{fWS_{laser}}\right)^{-1} + \frac{S_{pass}}{1-f}. \qquad (9)$$

Here $W$ is the wafer thickness, $p$ is the laser spot pitch, $f$ is the fill factor of laser damage and $S_{pass}$ is the passivated SRV. Using this value for $S_{laser}$, and using a modeled lifetime in the laser damaged region of 100 ns, the red dashed line in Fig. 2 is obtained. Although still not a perfect fit to experimental data, the fit is now much better. Arguably, the assumption that the laser damaged depth takes on a parabolic shape is somewhat arbitrary. In addition, the shape of the lifetime curve using long pulses may also be a result of other mechanisms, such as varying lifetime throughout the laser damaged region. As such, the dashed line in Fig. 2 is only meant as an indication that the shape of the lifetime curve will vary with assumptions on damage geometry and variations in lifetime throughout the laser damaged region.

## 5. Conclusion

We have measured the depth of laser-induced damage in silicon using ultrashort and long laser pulses, by etch back experiments. The laser-induced damage in silicon is found to be confined within 70 nm, 240 nm and 210 nm for 3 ps laser pulses at 343, 515 and 1030 nm, respectively. This is a strong reduction in depth of damage compared to what was observed by Engelhart et al. [3] using nanosecond pulses at corresponding wavelengths. We conclude that strong reduction in thermal diffusion and non-linear confinement of the optical energy cause this trend.

With knowledge of the depth of laser damage, the laser source can be more efficiently targeted to a specific process. As an example, in our process for creation of diffractive structures in silicon [7], 300 – 350 nm of silicon is removed by etching after laser processing. As such, laser damage is expected to be removed when applying any of the three picosecond lasers investigated herein, yielding a process where the laser-induced damage is eliminated.

## Acknowledgements

This work has been funded by the Research Council of Norway through the project “Thin and highly efficient silicon-based solar cells incorporating nanostructures”, NFR Project No. 181884/S10.

## References

[1] D. Bäuerle, Laser Processing and Chemistry, 3rd ed., Springer, Berlin Heidelberg, 2000.

[2] R. Holenstein, S.E. Kirkwood, R. Fedosejevs and Y.Y. Tsui, Simulation of femtosecond laser ablation of silicon, in: Proc. SPIE 5579, Photonics North 2004: Photonic Applications in Telecommunications, Sensors, Software, and Lasers, Spie, Ottawa, Canada, 2004: pp. 688–695.

[3] P. Engelhart, R. Grischke, S. Eidelloth, R. Meyer, A. Schoonderbeek, U. Stute, et al., Laser Processing for Back-contacted Silicon Solar Cells, in: ICALEO Congress Proceedings, Scottsdale, AZ, 2006: pp. 218–226.

[4] H.R. Shanks, P.D. Maycock, P.H. Sidles and G.C. Danielson, Thermal conductivity of Silicon from 300 to 1400 K, Physical Review. 130 (1963) 1743–148.

[5] A.B. Sproul, Dimensionless solution of the equation describing the effect of surface recombination on carrier decay in semiconductors, Journal of Applied Physics. 76 (1994) 2851–2854.

[6] J. Schmidt, A. Merkle, R. Brendel, B. Hoex, M.C.M. Van De Sanden and W.M.M. Kessels, Surface Passivation of High-efficiency Silicon Solar Cells by Atomic-layer-deposited $Al_2O_3$, Progress in Photovoltaics: Research and Applications. 16 (2008) 461–466.

[7] J. Thorstensen, J. Gjessing, E. Haugan and S.E. Foss, 2D periodic gratings by laser processing, Energy Procedia. 27 (2012) 343–348.